STUDY OF K^* RESONANCE PRODUCTION IN RELATIVISTIC HEAVY ION COLLISIONS AT RHIC

A THESIS SUBMITTED TO THE

HOMI BHABHA NATIONAL INSTITUTE

FOR THE DEGREE OF

DOCTOR OF PHILOSOPHY IN SCIENCE

(PHYSICS)

MAY, 2009

By

SADHANA DASH

INSTITUTE OF PHYSICS, BHUBANESWAR 751 005, INDIA

CERTIFICATE

This is to certify that the thesis entitled **" Study of K^* resonance production in relativistic heavy ion collisions at RHIC"** which is being submitted by **SADHANA DASH** who has been registered at the **Homi Bhabha National Institute** for the award of **Doctor of Philosophy in Science (Physics) degree** is a record of her own research work carried out by her. She has carried out her investigations for the last five years on the subject matter of the thesis under my guidance at the **Institute of Physics, Bhubaneswar**. To the best of my knowledge, the matter embodied in the thesis has not been submitted for the award of any other degree by her or by anybody else.

D.P. MAHAPATRA,
Professor,
Institute of Physics,
Bhubaneswar 751 005
India

Signature of the candidate

(Sadhana Dash)

Acknowledgements

I would like to venerate the Almighty for his benevolence, thanks galore for seeing me through the trials and tribulations of life till now. I would like to thank all the people who have inspired and helped me during my doctoral study.

Foremost, I would like to express my deep and sincere gratitude to my thesis advisor, Prof. D. P. Mahapatra for his continuous support. His wide knowledge and his logical way of thinking have been of great value to me. His understanding, encouragement and personal guidance have helped me immensely at all times during my doctoral research.

I wish to express my warm and sincere thanks to Dr. Bedangdas Mohanty for his invaluable advice, patience, untiring support and constructive criticism throughout my research. He guided me through the detailed analysis on my thesis topic, patiently answering all my queries. It has been a learning and rewarding experience working with him.

I would like to express my sincere thanks to Dr. Y. P. Viyogi, for his support, advice and useful suggestions.

I would like to thank Prof. S. C. Phatak and Dr. P. K. Sahu for all the fruitful discussions we had, for their kind support and encouragement.

I would like to extend my sincere thanks to Dr. Zhangbu Xu, Dr. Haibin Zhang, Zebo Tang, Dr. Xin Dong and Dr. Patricia Fachini for all the useful discussions and help on my research on resonance analysis. It was quite a learning and memorable experience.

I would also like to thank Dr. Dipak Mishra for all the help and encouragement during my thesis work. He and Haibin had introduced me to resonance analysis. He has always been friendly and forthcoming in extending support.

I express my hearty thanks to my collaborators Ajay Dash and Chitrasen Jena at IOP. It was a great experience in sharing together many happy moments both in academic and non-academic front. We had many lively discussions. Both have been very cooperative and friendly.

During this work, I have collaborated with many colleagues in PMD collaboration for whom I have great regard. I wish to extend my sincere thanks to my collaborators at VECC, Kolkata, Panjab University, Chandigarh, Jammu University, Jammu, Rajasthan University, Jaipur and IIT Bombay, Powaii. I thank them all for their useful suggestions, cooperation and encouragement. I had spent some very memorable time with them at various workshops, conferences and during my stay at BNL, New York.

I wish to thank each and every member of the STAR Collaboration for all their effort and support.

I take this opportunity to thank all the faculty members of IOP for their support, teachings and guidance. I would also like to thank all my faculties at Utkal University

who encouraged me to pursue research. I would like to thank my teachers at college and school level who taught me the basics. This thesis would not have been possible without their blessings.

In my daily work I have been blessed with a friendly and cheerful group of fellow students. I wish to express my warm and sincere thanks to all my seniors, my pre-doctoral batch mates and scholar friends at IOP for all their help and good wishes. I would like to thank Binata Panda as she has been very friendly, caring and understanding. Also I enjoyed the company of Mamata Sahoo. Both have been very cooperative and loving.

I am also thankful to all the library, administrative, laboratory, hostel mess, and computer centre staff of this institute for their prompt support at every stage.

My deepest gratitude goes to my parents, my sister, my husband and family members for their unflagging love and support throughout my life; this dissertation is simply impossible without them. I am indebted to them for their relentless care and love.

Date: **Sadhana Dash**

List of Publications/Preprints

*[1] K^{*0} **production in Cu+Cu and Au+Au collisions at** $sqrt(s_{NN})$ = **62.4 GeV and 200 GeV in STAR.**
S.Dash (for STAR collaboration), **J. Phys. G 35**, 104057 (2008).

[2] **Characterizing Jets in Heavy Ion collisions by Flow Method.**
S.Dash, D.K.Mishra, S.C. Phatak and P.K.Sahu, **J. Phys. G 35**, 104068 (2008).

*[3] K^{*} **production in heavy ion collisions at RHIC.**
S.Dash (for STAR collaboration), **J. Phys. G 35**, 044061 (2008).

*[4] K^{*} **(892) production in Au+Au collisions at RHIC.**
X.Dong, Z.Tang and S.Dash, **Int. J. Mod. Phys. E 16**, 2103-2109 (2007).

[5] **Flow Coefficients and Jet Characteristics in Heavy Ion Collisions.**
S.Dash, D.K.Mishra, S.C. Phatak and P.K.Sahu, **Applied Mathematics and Information Sciences 3(1)**, 97-115 (2009).

*[6] **Energy and System Size dependence of** K^{*} **production at RHIC.**
S.Dash, DAE-BRNS Nuclear Physics Symposium Proceedings (2007).

[7] **Identification and Characterization of Jet Events using Flow method in Heavy Ion Collisions.**

S.Dash, DAE-BRNS Nuclear Physics Symposium Proceedings (2005).

(*) indicates papers on which this thesis is based.

Synopsis

Ultra-relativistic nucleus-nucleus collisions at RHIC (Relativistic Heavy Ion Collider) provide means to create nuclear matter of high energy density over an extended volume. Modification of the production rates and the in-medium properties of hadronic resonances can be used as signatures of a possible phase transition of nuclear matter to a deconfined state of quarks and gluons. Such hadronic resonances, due to their short life times, can be used to investigate the freeze-out mechanisms following the hadronization. K^* meson is of particular interest due to its very short lifetime and its strange quark content. With $c\tau \sim 4fm$, the lifetime of K^* is expected to be less than the lifetime of the system formed. Therefore, the K^* is expected to decay, re-scatter and regenerate all the way throughout the kinetic freeze-out. Various in-medium effects, due to the high density and the high temperature of the medium, are expected to modify the characteristic properties of K^* resonance. Measurement of these properties such as mass, width, yield as a function of the transverse momentum can provide insight for understanding the dynamics of the medium created in the collision.

The present thesis investigates the production of the strange mesonic resonance K^* , at mid-rapidity, in Au+Au and Cu+Cu collisions at RHIC. The motivation for studying in Cu+Cu system is that it serves as a bridge between d+Au and Au+Au collisions in terms of number of participants and number of binary collisions. In particular, looking at the data in terms of number of participants offers the possibility of

studying system size dependence of various bulk properties and may help to disentangle the initial state versus final state scenarios at RHIC. Through a comparison with similar data on other resonances, the evolution of the fireball is studied. The data used for the analysis presented in this thesis were taken with the STAR (Solenoidal Tracker at RHIC) detector. The primary tracking device, TPC (Time Projection Chamber) within STAR was used to measure the K^* production via its hadronic decay channel, $K^{*0} \rightarrow K^+\pi^-$ and $\overline{K^{*0}} \rightarrow K^-\pi^+$. TPC provides identification and momentum information of the charged particles by measuring their ionization energy loss (dE/dx). Measurement of K^* yield, through its hadronic decay channel, has been carried out, for all centralities, for Au+Au collisions at center of mass energy 62.4 GeV and Cu+Cu collisions at center of mass energy 62.4 GeV and 200 GeV. The invariant mass spectra of K^* , for various collision centralities, were reconstructed using the standard combinatorial technique. The mixed event technique was used for determining the uncorrelated background. The inverse slope parameters, and the yields for $0.2 \leq p_T \leq 3.0$ GeV/c, as determined from the above data, are compared for various centralities in different collision systems. The mean p_T for K^* has been compared with the same for other stable particles (kaon, pion and proton) to investigate particle production mechanism.

Due to the short life time, some K^* produced at hadronization will decay in the medium, and because of frequent re-scattering of its daughter particles with other hadrons, the K^* decayed inside the medium may not be reconstructed. Alternatively, in the presence of large population of pion and kaon, the K^* can be regenerated by the re-scattering of pion and kaon through the so-called pseudo-elastic collisions, $\pi K \rightarrow K^*$. These two competing processes determine the final observed yield of the K^* resonance and it depends upon the time span between the chemical and kinetic freeze-out and the daughter particle's interaction cross-section in the medium. The measurement of K^{*0}/K^- yield ratio can provide vital information on the K^*

production properties as K^{*0} and K^{-} have different masses and spin but have identical quark content. It is observed that K^{*0}/K^{-} ratio is much smaller than unity in central Au+Au collisions. This signals towards strong re-scattering of decay daughters of K^{*} meson which results in loss of reconstruction of K^{*} signal. Another parameter of considerable interest is ϕ/K^{*0} ratio as both ϕ and K^{*0} have similar masses with the same spin. However, they have different lifetime and strangeness. The lifetime of ϕ meson is 10 times more than that of K^{*0}. Due to longer lifetime of ϕ meson and negligible σ_{KK}, we expect both the re-scattering and regeneration effect to be negligible for the ϕ meson. Since ϕ has two strange quarks and K^{*0} has one, ϕ/K^{*0} ratio can also provide information regarding strangeness enhancement. This ratio is observed to increase with centrality favoring re-scattering scenario of $K^{*}0$ daughter particles. The observed increase can have contributions from possible strangeness enhancement in more central collisions. The nuclear modification factors R_{AA} or R_{CP} of K^{*} meson are of vital importance in differentiating between the mass and particle species ordering in particle production. Earlier STAR measurement of nuclear modification factor for various hadrons had supported the baryon-meson effect over the mass effect as per the predictions of quark coalescence model. As the mass of K^{*} is close to the mass of baryons (proton, Λ) and it is a vector meson, a comparison of nuclear modification factors R_{AA} or R_{CP} of K^{*} with those of K^{0}_{S} and Λ can be used to distinguish whether the differences are due to their differences in masses or particle species. The nuclear modification factor, R_{CP}, for K^{*}, in the intermediate p_T range, has been found to support the quark coalescence model for particle production.

Contents

List of Figures

List of Tables

Chapter 1

Introduction

The dynamics of both matter and energy in nature are best understood in terms of the kinematics and interactions of fundamental particles. A small core of fundamental laws and theories govern the behavior and interaction of all types of matter and energy. A major goal in physics is to find out the common ground that would unite all of these theories into one integrated theory of everything. The Standard Model of particle physics describes three of the four known fundamental interactions *viz.* the Electromagnetic, the Weak and the Strong interactions between the elementary particles. The Standard Model combines the Electroweak theory, a combined theory of Electromagnetic and Weak interactions, together with Quantum Chromodynamics (QCD) which is the theory of strong interactions. Unfortunately, it has so far not been possible to unite Gravity into such a unified theory. The Standard Model of particle physics contains 12 flavors of elementary fermions (3 quarks, 3 leptons and their corresponding antiparticles) together with elementary bosons that mediate the forces. Figure 1.1 depicts the constituents of the Standard model showing the elementary particles and the mediators of the interactions.

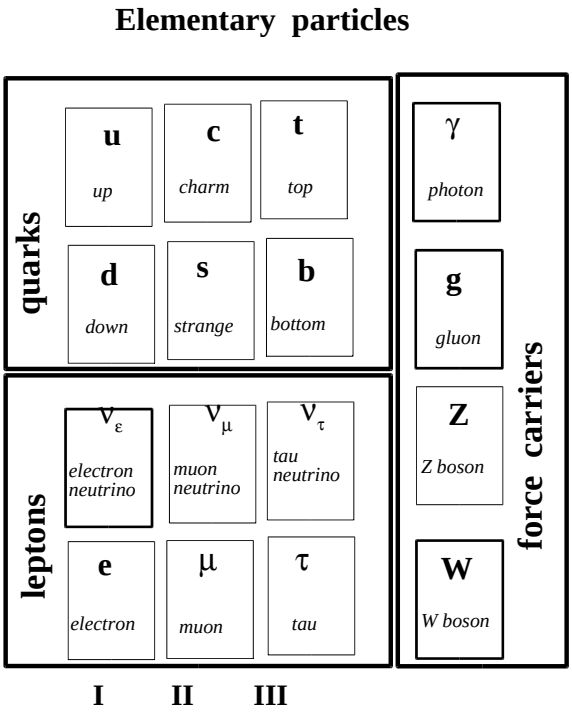

Figure 1.1: The fundamental particles of Standard Model and the force mediating bosons.

1.1 Quantum Chromodynamics (QCD)

The bulk of hadronic matter is comprised of partons consisting of quarks and gluons. These are bound into neutrons, protons (and subsequently into nuclei) and mesons by the strong force mediated by the field quanta, the gluons. Thus quarks and gluons are the basic building blocks of normal matter. The fundamental interactions between these partons are described by the theory of Quantum Chromodynamics (QCD) [1, 2]. The fundamental particles in QCD *viz.* quarks and gluons carry a color

charge and hence the name "chromodynamics". This theory exhibits two remarkable features at both large and small distances between the quarks and gluons. These two properties namely the *Confinement* and *Asymptotic Freedom* can be understood from the expression of strong interaction coupling constant, α_s given by

$$\alpha_s(Q^2) = \frac{3}{(33 - (2N_f ln(q^2/\lambda^2))} \tag{1.1}$$

where Q^2 is the momentum transfer, N_f is the number of quark flavors and λ is the scaling parameter. At small momentum transfer and large distances, the value of α_s is large and thus, the color charged particles (such as quarks) cannot be isolated singularly. The quarks are confined together with other quarks by the strong interaction to form pairs (mesons) or triplets (baryons) so that the observed hadrons (meson or baryon) are color neutral. This phenomenon is called *Quark Confinement*, or often just confinement. For sufficiently short distances or large momentum transfers, α_s tends to zero and quarks behave as free non-interacting particles. As a consequence, QCD medium at very high temperatures is predicted to be a gas of free quarks and gluons. This property, where the interactions between the quarks becomes arbitrarily weak at length scales that asymptotically goes to zero, is known as *Asymptotic Freedom*. This was discovered in 1973 by David Gross, Frank Wilczek, and David Politzer who were awarded the Nobel Prize in Physics in 2004.

1.1.1 QCD Phase Transition and QGP

Even before the identification of QCD as the theory of strong interaction there was considerable interest in the fate of nuclear matter subjected to extreme temperatures and densities [3, 4, 5]. Soon after the discovery of the asymptotic freedom, in 1975, Collins and Perry, in their study on QCD at low temperatures and high densities, had observed that the reduction of the coupling constant at small distances indicated that the dense nuclear matter at the center of neutron stars would consist of deconfined

quarks and gluons [6, 7]. At sufficiently high temperature, the hadrons are expected to melt, deconfining quarks and gluons. The exposure of new color degree of freedom would then be manifested by a rapid increase in entropy density and hence in pressure. We define this Quark Gluon Plasma (QGP) state to be a locally thermally equilibrated state of matter consisting of deconfined quarks and gluons interacting through color charge [8]. QCD calculations, carried out on a lattice, indicate a transition from a hadronic phase to a deconfined phase of QGP to be taking place at a temperature T_C of $\sim$ 170 MeV at an energy density $\sim$ 1 GeV/fm^3 [7].

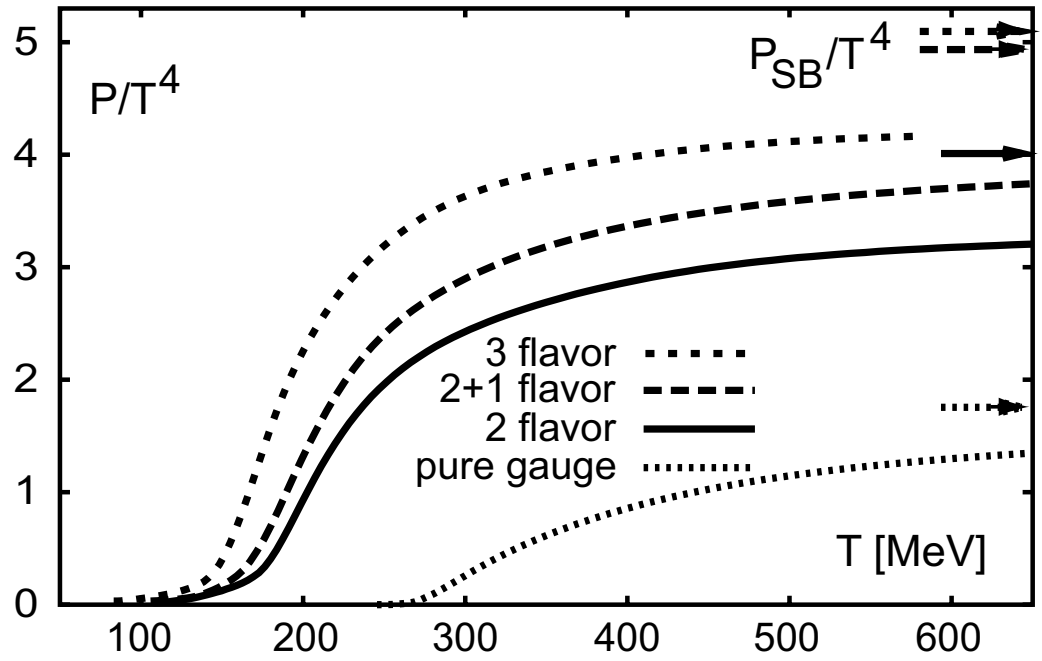

Figure 1.2: The pressure divided by T^4 as a function of temperature of strongly interacting matter, and for several other choices of the number of dynamical quark flavors from Lattice QCD results [9]. The arrows pointing to right indicate the corresponding Stefan-Boltzmann pressures for the same quark flavor assumptions . The figure has been taken from [8].

Some results from lattice QCD calculations are presented in Figure 1.2. For a weakly interacting ideal gas, the energy density and pressure approach the Stefan-Boltzmann limit at asymptotically high temperatures [9]. As shown in Figure 1.2, the

pressure divided by T^4 increases above T_C, and saturates at about $2T_C$. This value of P/T^4 lies substantially below the Stefan-Boltzmann limit and the deviation suggests quarks and gluons interact among themselves in the QGP phase. Lattice QCD also predicts that the deconfinement transition is accompanied by a chiral symmetry restoration transition.

Figure 1.3 shows the various phases of QCD matter as a function of temperature T and baryon chemical potential, μ_B [10]. For very high T and low μ_B, a state of weakly interacting quarks and gluons is expected to exist. This state mimics the condition of the early universe. The T_C at zero μ_B is around 170 MeV. At low T and very high μ_B, the conditions are similar to what it is expected in the core of neutron stars. For low T and low μ_B, the quarks and gluons are color confined inside the hadrons resulting in a hadron gas phase.

1.2 Heavy Ion Collisions

Following the Big-bang, which is accepted to mark the beginning of the Universe, all matter existed as quarks and gluons along with some electrons and neutrinos. A transition from a deconfined QGP state to confined color neutral states occurred during the rapid expansion in the early universe. The net baryon density was low and the temperatures were high during the initial stages. Therefore, one assumes zero baryonic chemical potential, μ_B, while calculating thermodynamic properties of the strongly interacting matter in the early universe. It is important to re-establish these conditions in the laboratory and study the evolution process. Heavy ion collisions at relativistic energies provide a promising tool for such studies of QCD at extreme temperatures and densities, particularly, the deconfining transitions of quarks and gluons from a hadronic state to a QGP state. The energy density attained can be high enough to allow a phase transition, leading to the formation of QGP.

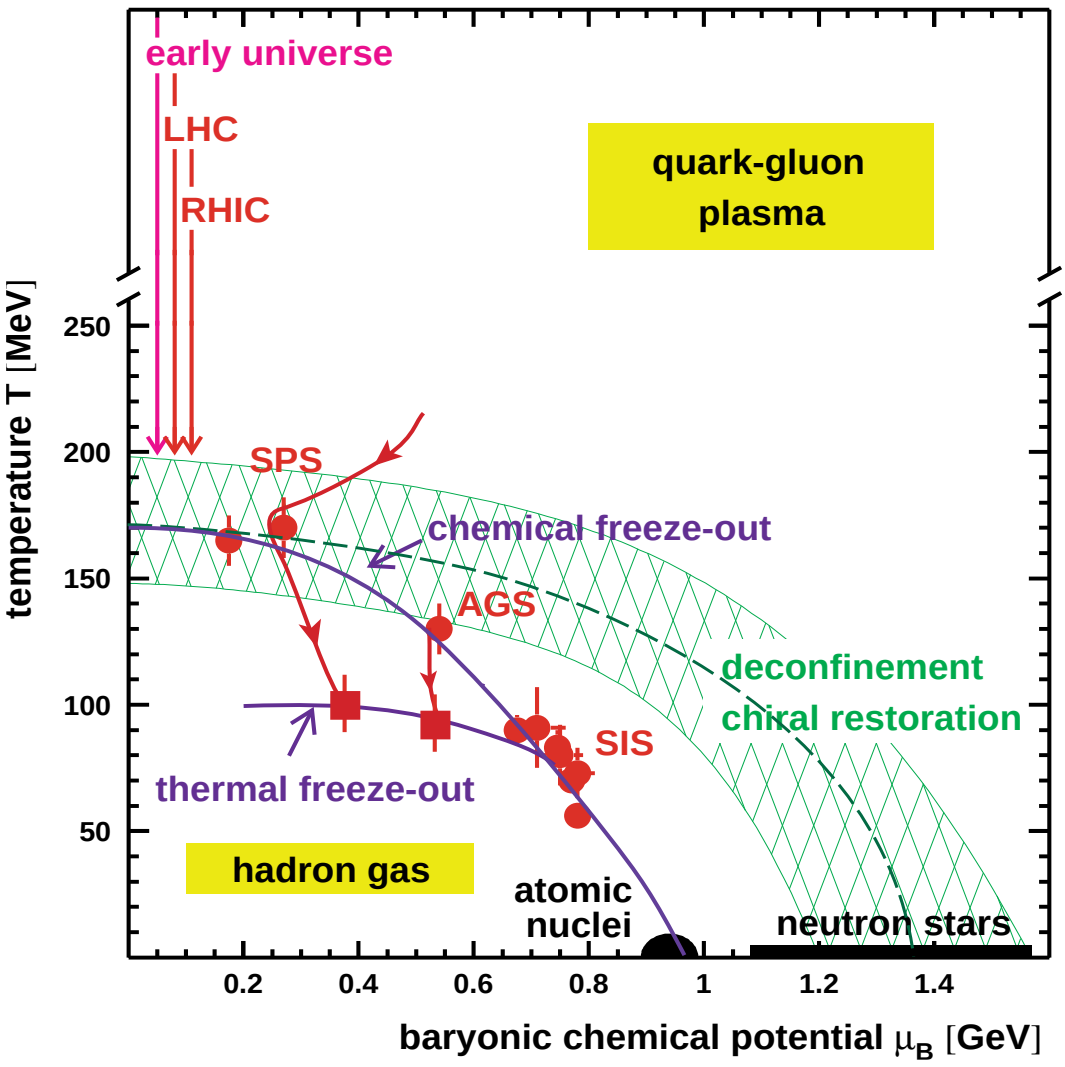

Figure 1.3: Phase diagram of hadronic and partonic Matter [10].

In this quest for the discovery of an exotic QGP state and to get some information on the hadronisation process that took place in the early universe, a number of experiments were carried out over the last thirty years. In the first round of experiments, carried out during 1986-1990, only light ions could be used producing nuclear matter at lower energy densities, insufficient to produce a deconfined QGP state. Subsequently heavier targets (Pb, Au) with higher beam energy were used to achieve higher energy density and temperature. The initial, fixed-target experimental program using the Alternating Gradient Synchrotron (AGS) at the Brookhaven National Laboratory (BNL), used Si beams at 14.6 GeV per nucleon and O beams at 11 GeV per nucleon. The later fixed-target experiments, carried out at the Super Proton Synchrotron (SPS) facility at CERN, utilized O beams at 60-200 GeV per nucleon, S beams at 200 GeV per nucleon and Pb beams at 158 GeV per nucleon. Finally, a series of such experiments, carried out with Pb+Pb collisions at a center of mass energy of 17.2 GeV at CERN SPS signaled towards a possible phase transition and formation of QGP [11, 12]. After these very exciting results, the focus shifted to go higher up in energy density where the life time of the deconfined phase is expected to be longer. To keep pace with these activities at CERN, a Relativistic Heavy Ion Collider (RHIC) was built at BNL with a possibility of raising the center of mass energy to 200 GeV using two colliding Au beams. The RHIC experiments at BNL began around 2000 and studied the collisions of p+p, d+Au, Cu+Cu and Au+Au at center of mass energies ranging from 19.6 GeV to 200 GeV. The programme still continues with exciting results coming from time to time. All of the four experimental programs that started in the year 2000 at RHIC, *viz* STAR (A Solenoidal Tracker at RHIC), PHENIX (Pioneering High Energy Nuclear Interaction eXperiment), BHRAHMS (Broad RAnge Hadron Magnetic Spectrometers) and PHOBOS provided enough experimental evidences which confirm the existence of a very strongly interacting matter in the form of a QGP [8, 7, 13, 14].

At the moment the experimental program is heading towards Large Hadron collider (LHC) at CERN. Here with collisions of Pb beams at a center of mass energy of 5.5 TeV, we expect a much higher life time of the deconfined state and thus it would be possible to identify the state and study its properties in details. Although the primary aim of LHC experiments is to discover the Higg's boson for the experimental validation of the Standard Model, heavy ion collision experiments with colliding Pb beams also forms a major activity.

1.2.1 Space time Evolution of Heavy Ion Collisions

Let us consider a head-on collision of two heavy nuclei, A and B, moving with relativistic energies, in the center of mass frame. The dynamics of such a collision can be viewed in the space time diagram with the longitudinal co-ordinate z and the time co-ordinate t as illustrated in Figure 1.4. The trajectories of the colliding nuclei are shown as thick lines. The colliding nuclei are Lorentz contracted due to their relativistic speeds. The projectile nucleus B with velocity close to speed of light comes from $z = -\infty$ and meets the target nucleus, A, coming from $z = +\infty$ with same speed. They meet at $z = 0$ and $t = 0$.

After the collision, the energy density may not reach the critical value and in such a case the system consists of a gas of hadrons. However, if the initial energy density is high enough to deconfine the hadrons into a fireball of quarks and gluons, then multiple parton-parton interactions can lead to establishment of thermodynamic equilibrium and the phase can be identified as a QGP state. Subsequent evolution of the system from this QGP state can be described by hydrodynamics. In the evolution, the QGP expands rapidly, lowering its temperature till a critical transition temperature, T_C is reached followed by hadronisation. As the hadrons require some finite time to be formed, the matter spends some time in the mixed phase where quarks and gluons co-exist with hadrons. The expansion is likely to be isothermal in

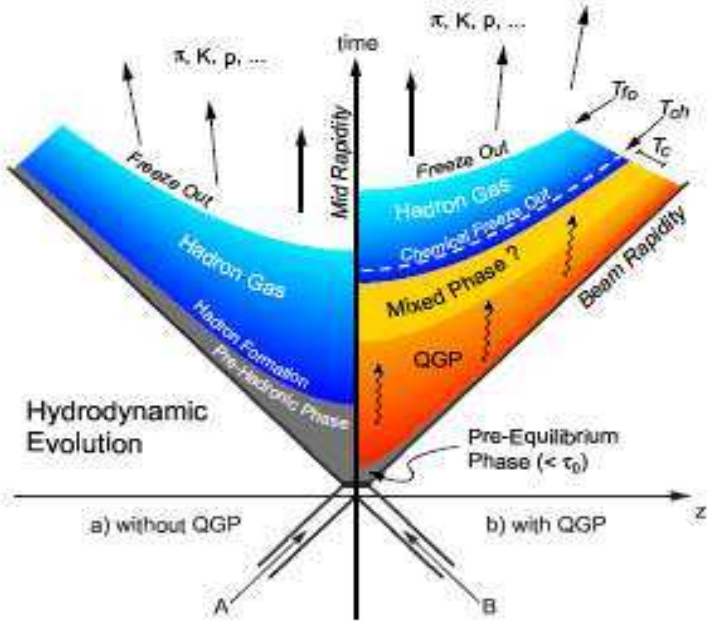

Figure 1.4: Space-time diagram of longitudinal evolution of the quark-gluon plasma.

this phase and the latent heat is absorbed in the conversion of the degrees of freedom of quarks and gluons into hadronic degrees of freedom. In the hadron gas phase, all the quarks and gluons are confined inside the hadrons. The expansion of the system continues and at a temperature T_{ch}, the inelastic interactions between the hadrons cease. The particle abundances reach a constant value and there is no further creation and annihilation of particles. This is called the *chemical freeze-out*. The expansion continues until the mean free path of the hadrons exceeds the dynamical size of the system and the hadrons interact no more. This is called *kinetic freeze-out* following which the hadrons freely stream out and are measured in detectors.

1.3 Signatures of Quark Gluon Plasma

As mentioned in earlier section, the heavy ion collisions can lead to formation of a phase of matter consisting of deconfined quarks and gluons. This QGP state goes through several stages during its evolution namely a pre-equilibrium process and its formation through thermalization, a mixed phase (containing quarks and gluons mixed with hadrons), a hadron gas phase and a phase of free hadrons. Each stage has certain characteristic properties related to the type of particles produced, their life time and production mechanism. The evolving system can be characterized by identifying and studying the appropriate experimental parameters to examine the different stages formed. The experimental probes can be basically categorised into two groups namely the soft probes and hard probes. The former includes the bulk matter signatures such as particle multiplicities, particle ratios, transverse momentum spectra, flow and particle correlations. All these provide a picture of thermalization and spatial evolution. The later include a class of penetrating probes, known as hard probes, which probe the system before thermalization through hard scattering processes providing information on the partonic energy loss in the medium formed.

In the following sections we briefly review some of the proposed signatures of the formation of quark gluon plasma.

1.3.1 Particle Yield and Transverse Momentum Distributions

Measurement of particle yields in nucleus-nucleus collisions can provide information about the system during the chemical freeze-out stage. At the chemical freeze-out, the inelastic interactions among the produced hadrons ceases and there is no further creation or annihilation of particles. Hence, we expect the hadronic yield ratios to be fixed as chemical abundances are fixed. Within the framework of the Statistical Model [15, 16, 17], the measured ratios can be used to constrain the system temperature and the baryonic chemical potential, μ_B, at chemical freeze-out. The above mentioned Statistical models predict that the system is in thermal and chemical equilibrium at this stage. Figure 1.5 shows a comparison of the experimental p_T integrated hadron yield ratios, as measured by STAR at mid-rapidity for Au+Au collisions, with statistical model fits. The excellent fit obtained to the ratios indicates that the light flavors have reached chemical equilibrium at a temperature, T_{ch} = 163.5 MeV [18]. The inset of Figure 1.5 shows the variation of the strangeness suppression factor, γ_s with centrality. The value of γ_s reaches 1 for most central collisions. This is consistent with chemical equilibrium being achieved before hadronisation.

The transverse momentum distribution of hadrons reflects the conditions reached late in the reaction as well as the integrated effects of expansion from the beginning of the collision [7]. The characteristics of the system at kinetic freeze-out can be explored by analyzing the spectra of various hadron species. Kinetic equilibration is thought to prevail over the transverse degrees of freedom, therefore transverse momentum, p_T or transverse mass, m_T distribution are used to extract the kinetic freeze-out temperature, T_{fo} . The spectra are usually fit to hydrodynamics motivated fits to extract model parameters such as the kinetic freeze-out temperature, T_{fo} and the radial flow

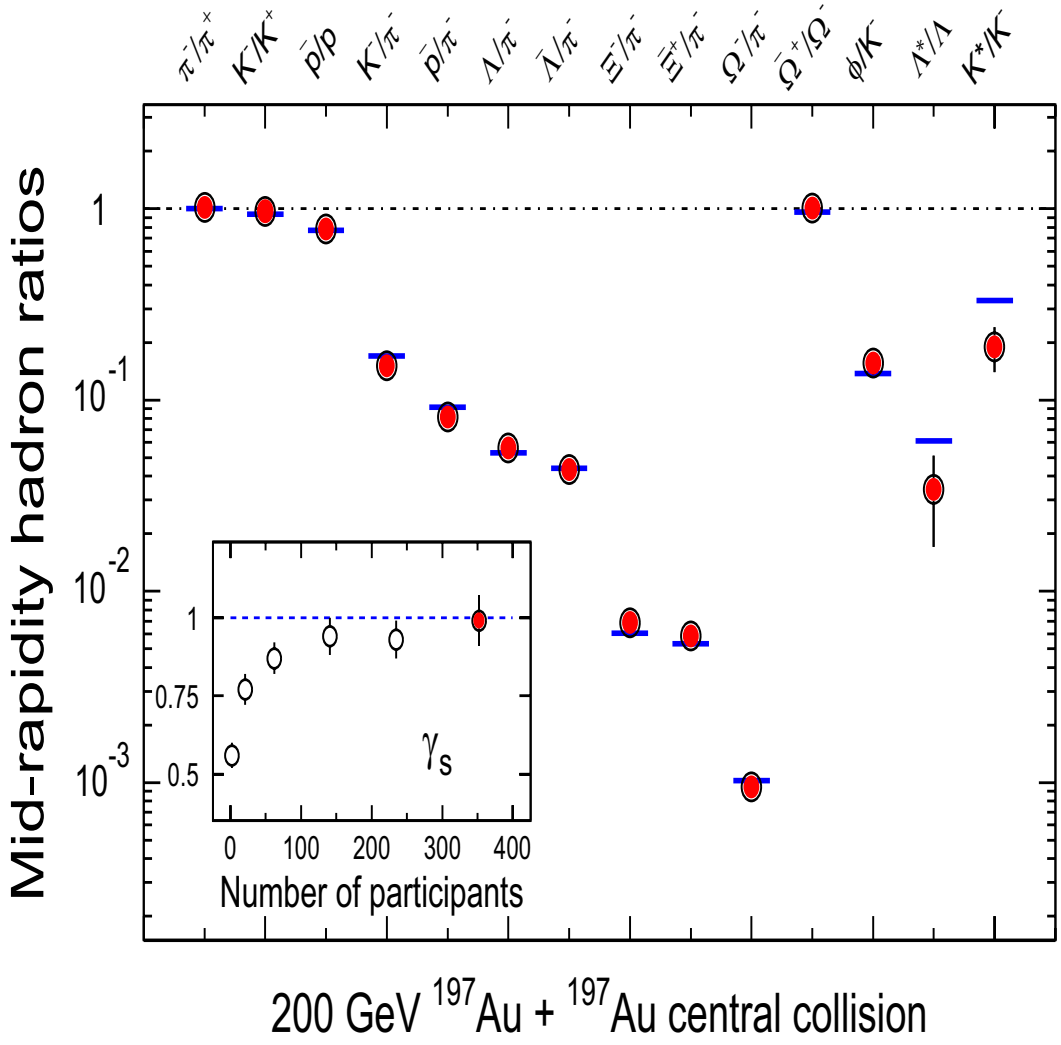

Figure 1.5: Ratios of the mid-rapidity p_T integrated yields for different hadron species in Au+Au collisions at 200 GeV. The horizontal lines represent the statistical model fits to the particle ratios.The fit parameters are $T_{ch} = 163 \pm 4 MeV$, $\mu_B = 24 \pm 4 MeV$, $\gamma_s = 0.99 \pm 0.07$ [18]. The inset shows the variation of γ_s with centrality. The figure is taken from [8].

velocity (β_T). The p_T distribution of hadrons also have a collective component which arises due to matter density gradient from the center to the boundary of the system created. Frequent interactions among the constituents push the matter outward and this leads to a common constituent velocity distribution. We can characterize the change in p_T spectra as a function of centrality for an estimation of the mean p_T ($< p_T >$).

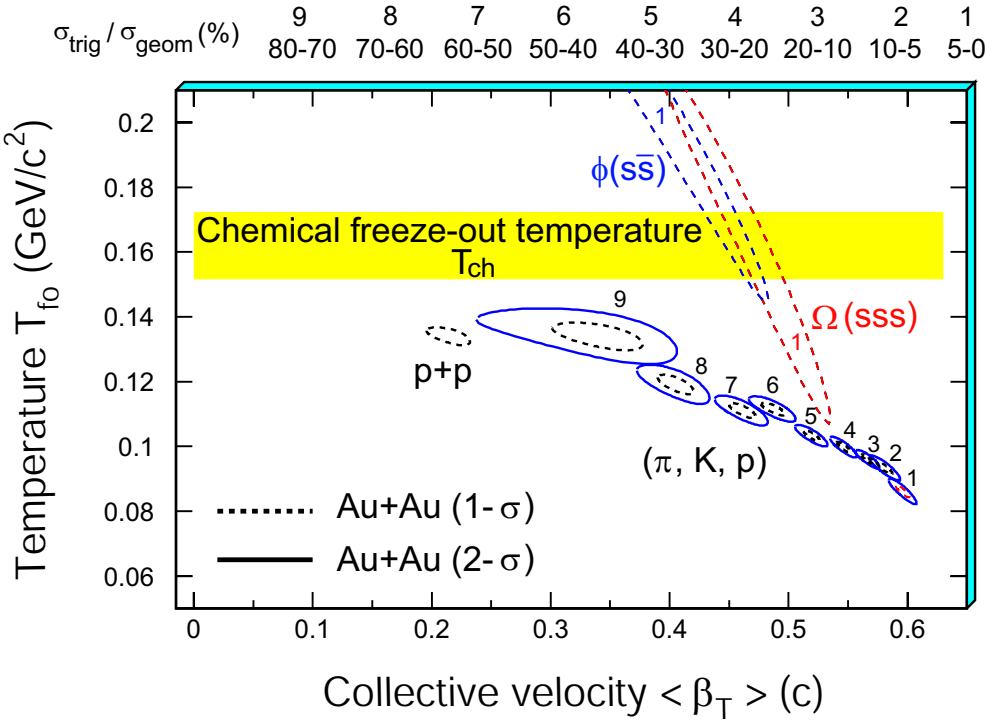

Figure 1.6: The χ^2 contours for T_{fo} and $< \beta >$ extracted from thermal and radial flow fits for different hadrons produced in Au+Au collisions at 200 GeV. The figure is taken from [8].

Figure 1.6 depicts the values of T_{fo} and $< \beta_T >$ extracted from thermal and radial flow fits for different centrality bins and hadron species as obtained in Au+Au collisions at 200 GeV. We observe that bulk of the system consisting of kaons, pions and protons become cooler at kinetic freeze-out and develop a stronger collective flow. This may signal that there is a rapid expansion after chemical freeze-out which

is seen to increase with centrality. The results obtained with ϕ and Ω indicate reduced hadronic interactions after chemical freeze-out.

1.3.2 Elliptic Flow

In non-central collisions, the spatial distribution of colliding matter resembles an ellipsoid due to incomplete overlap of the two colliding nuclei. If the particles interact with each other to produce pressure gradients, the system expands more strongly along the short axis of the ellipse and the initial stage spatial anisotropy gets converted into momentum-space anisotropy. The anisotropy of the particle yield versus the reaction plane can be characterized by a Fourier expansion [19]:

$$E\frac{d^3N}{d^3p} = \frac{1}{2\pi}\frac{d^2N}{p_T dp_T dy}(1 + \sum_{n=1}^{\infty} 2v_n cos[n(\phi - \Psi_r)]) \tag{1.2}$$

where ϕ is the azimuthal angle, v_n's are the n^{th}-order Fourier coefficients, Ψ_r being the reaction plane angle. The Fourier coefficient, v_1 represents the directed flow while v_2 stands for the elliptic flow. The elliptic flow coefficient, v_2, is expected to be dominant by virtue of the geometry of collision. The observed particle yields versus azimuthal angle measured with respect to reaction plane can provide information on early collision dynamics.

Figure 1.7 depicts the p_T integrated mid-rapidity elliptic flow coefficient, v_2, as a function of collision centrality, as obtained at SPS [20] and RHIC [21, 22] energies. We can observe the characteristic centrality dependence that reflects an increase of spatial eccentricity of the collision geometry with an increase of impact parameter.

Figure 1.8 shows the STAR experimental results for the low p_T v_2 distributions in 200 GeV Au+Au collisions for different charged particles. As can be seen in the figure, the v_2, for different hadrons, scale with the particle mass. The systematic dependence of v_2 on particle mass is a strong indicator that a common transverse velocity field

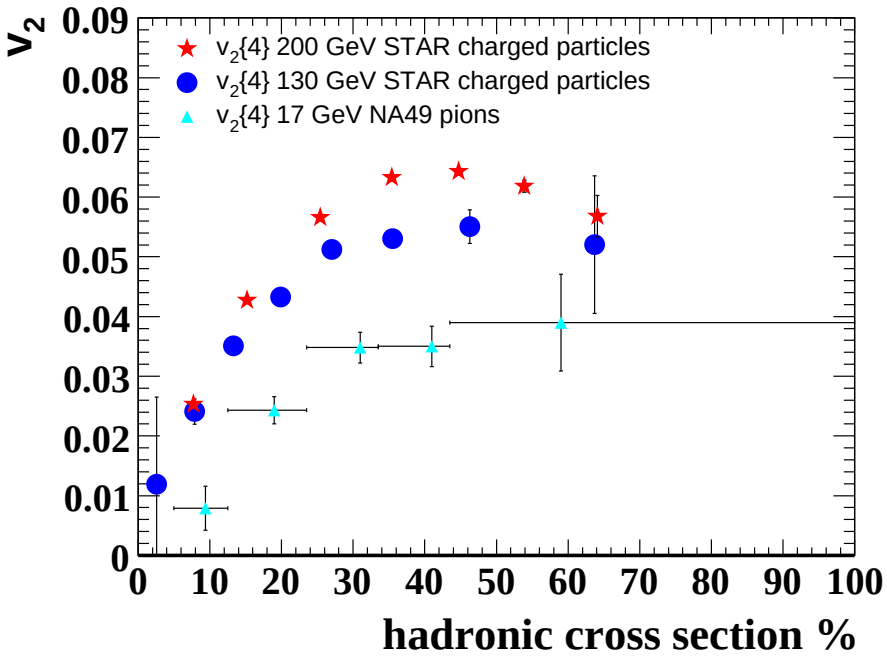

Figure 1.7: The centrality dependence of p_T integrated v_2. The triangles are NA49 measurements for pions [20]. The circles and crosses are STAR measurements for charged particles at 130 GeV [21] and 200 GeV [22] respectively.

underlies the observations. The absolute value of v_2 and the mass-dependence is well reproduced by hydrodynamic calculations [24]. The agreement with hydrodynamic calculation, which assume early thermalization and ideal relativistic fluid expansion is one of the centerpieces of the discovery of QGP, as claimed at RHIC.

Figure 1.9 represents the v_2 measurements for identified hadrons in the 200 GeV Au+Au minimum-bias sample by STAR and PHENIX experiments. For $p_T > 2$ GeV/c, one can see that the observed values of v_2 saturate and there is a substantial difference between the saturation levels for baryons and mesons. This provides some important information regarding the origin of baryon-meson difference which characterize this p_T range. The hydrodynamic calculations over predict the data for $p_T > 2$ GeV/c. However, if we divide the v_2 values with the number of constituent quarks, n (i.e. $n = 2$ for mesons and $n = 3$ for baryons), we observe a scaling for $p_T/n > 1$

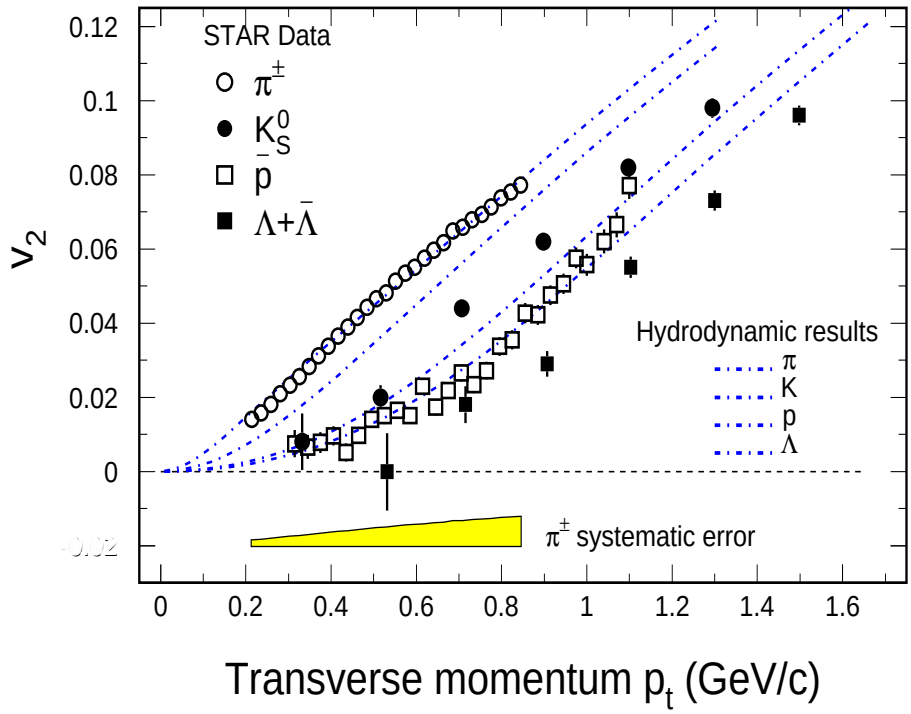

Figure 1.8: The p_T dependence of the elliptic flow parameter, v_2 in 200 GeV Au+Au collisions as measured by the STAR experiment. The hydrodynamic calculations are shown as dot-dashed lines. This figure has been taken from [23].

GeV/c.

The upper panel in Figure 1.10 shows the STAR experimental results on v_2/n Vs p_T/n for identified hadrons in the 200 GeV Au+Au minimum-bias sample. Here n stands for the number of constituent quarks. The dashed-dotted line denotes a polynomial fit to the data. In the intermediate p_T range, the apparent scaling behavior points towards the quark degree of freedom as the most effective one determining the hadron flow. It indicates that hadron formation at intermediate p_T proceeds via quark coalescence [25]. The constituent quarks carry their own substantial azimuthal

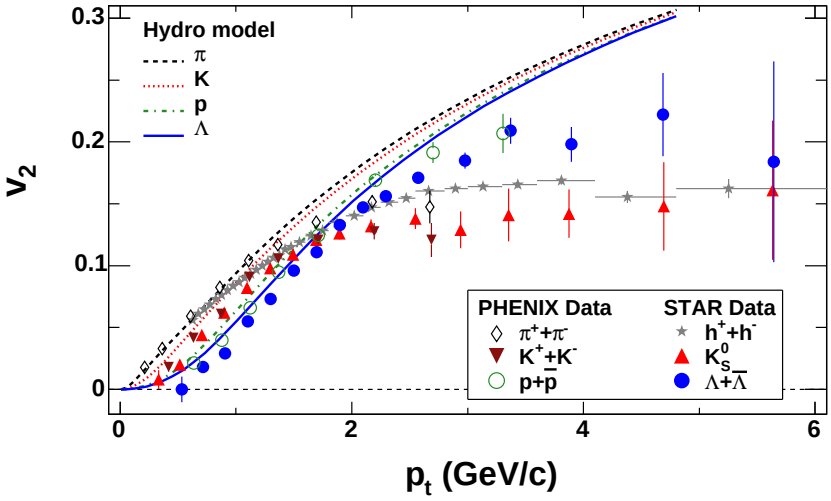

Figure 1.9: $v_2(p_T)$ for minimum-bias events (circles) for Au+Au collisions at $\sqrt{s_{NN}}$ = 200 GeV. Also shown as pure hydrodynamical calculations [24] (dotted curves).

anisotropy which is later summed up to give the hadronic flow.

1.3.3 Strangeness Enhancement

Enhanced production of strange hadrons has been proposed as a signature of transition from hadronic matter to QGP [26]. In p+p collisions, the production of strange particles is strongly suppressed due to the higher mass of the s quark. Also the system size created in a p+p collision is small and the reduced phase space results in suppression of strangeness production [27, 28]. The yield of strange and multi-strange mesons as well as baryons has been predicted to be strongly enhanced in the presence of QGP as compared to the purely hadronic scenario at the same temperature. The strange quark production is facilitated by two characteristic properties of QGP *viz* the partial restoration of chiral symmetry and deconfinement of color [29]. The first property has the effects of lowering the energy threshold for strange quark production while the second one results in very high density gluonic excitations which can

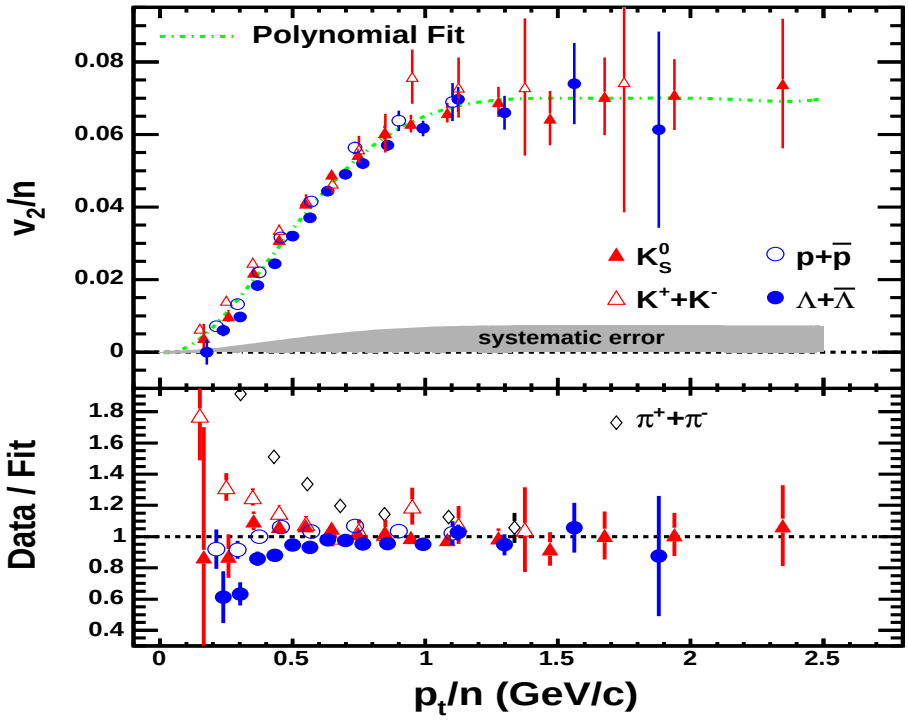

Figure 1.10: **Upper Panel** v_2/n Vs p_T/n for identified particles measured by the STAR experiment. n is the number of constituent quarks. The dashed-dotted line is the polynomial fit to the data. **Lower Panel** The data from the upper panel is divided by the polynomial fit as a function of p_T/n. [23]

produce $s\overline{s}$ pairs via QCD interactions.

Figure 1.11 depicts high statistics data from p+p and Au+Au collisions at 200 GeV for strange and multi-strange baryon production at mid-rapidity measured by STAR [30]. The results are shown against the mean number of participants $< N_{part} >$ which is obtained from Glauber model [31]. One can see, for all particles shown, there is an enhancement in the yields over that expected from an $< N_{part} >$ scaling.

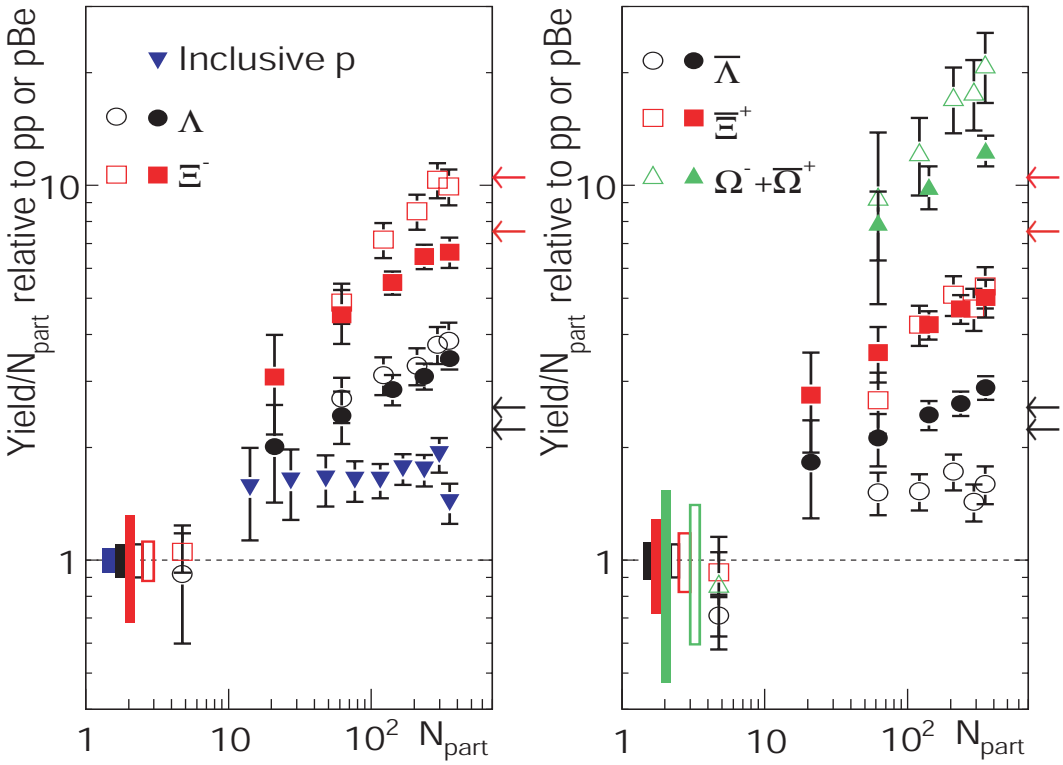

Figure 1.11: Mid-rapidity strangeness enhancement as a function of $< N_{part} >$ for strange baryons and inclusive protons. The solid markers are for Au+Au collisions at $\sqrt{s_{NN}} = 200$ GeV and the open symbols are for Pb+Pb collisions at $\sqrt{s_{NN}} = 17.3$ GeV.

1.3.4 Nuclear Modification Factor

It is very useful to scale the hadron spectra corresponding to nucleus-nucleus (AA) collisions with the same obtained from nucleon-nucleon (NN) collisions. Such a scaling provides some additional information on particle production mechanisms in hot nuclear matter (in AA system) compared to those in cold nuclear medium (NN system). Any effect of a nuclear medium on the total particle production can be extracted using the above scaling since no such medium is expected to be produced in elementary nucleon-nucleon collisions. Keeping the above goal in mind, a nuclear modification factor is constructed which is defined as

$$R_{AA}(p_T) = \frac{d^2N^{AA}/dp_T d\eta}{T_{AA} d^2\sigma^{NN}/dp_T d\eta} \tag{1.3}$$

where $T_{AA} = < N_{bin} > /\sigma_{inel}^{NN}$. N_{bin} is the average number of binary nucleon-nucleon collisions, as estimated by Glauber calculations [31]. In the absence of medium effects, a nucleus-nucleus collision could be viewed simply as a superposition of individual nucleon-nucleon collisions, where the R_{AA} factor would be unity, above a certain p_T threshold. The later is because at low p_T we expect a scaling of particle production with number of participating nucleons, N_{part}, rather than number of binary collisions, N_{bin}.

A similar ratio R_{CP} is also defined in terms of the spectra measured for central and peripheral events, both scaled in terms of the number of binary collisions. Here one approximates the effects of p+p collisions by peripheral nucleus-nucleus collisions. One can construct R_{CP} as

$$R_{CP} = \frac{< N_{bin}^{peripheral} > d^2N^{central}/dp_T d\eta}{< N_{bin}^{central} > d^2N^{peripheral}/dp_T d\eta} \tag{1.4}$$

Figure 1.12 depicts R_{AB}, the ratio of inclusive hadron yields in A+B (Au+Au *or* d+Au) collisions to the same in p+p collisions. One can see a suppression in high

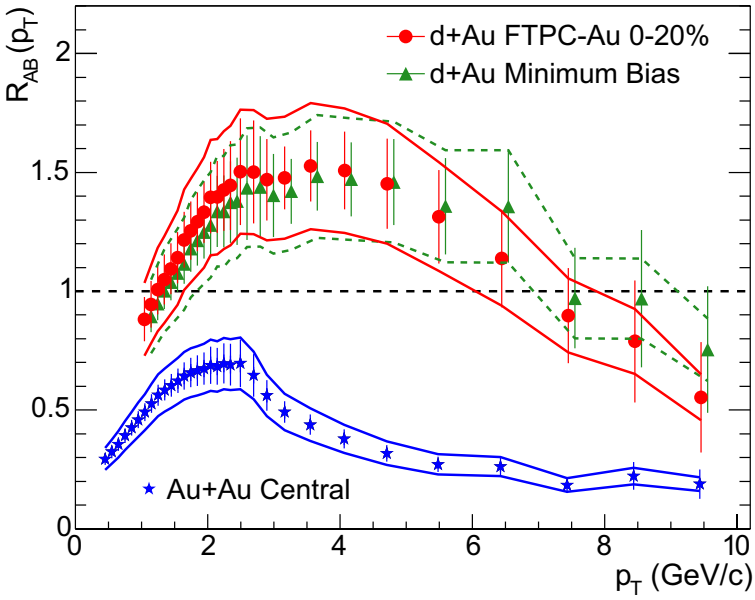

Figure 1.12: STAR data of R_{CP} for charged hadron and π^0 inclusive yields for d+Au and central Au+Au collisions in 200 GeV [32].

p_T hadrons in central Au+Au collisions. This suppression, which is mainly due to final state interactions, is not seen in d+Au collisions where the conventional initial state interactions such as multiple scatterings, gluon saturation etc are present. In case d+Au collisions, a Cronin-like enhancement due to initial state broadening of intrinsic quark transverse momenta is seen [33]. The observed suppression in Au+Au collisions can be attributed to the final state interactions of hard scattered partons and their fragmentation products. This can be visualised in terms of partonic energy loss due to gluon bremsstrahlung in the deconfined medium with high density of color charges.

1.3.5 Quarkonia Suppression

In early pre-thermal stages of the collision, heavier quark flavor mesons $c\overline{c}$ and $b\overline{b}$ may be created due to $q\overline{q}$ fusion or gluon fusion. As proposed by Matsui and Satz

[34] suppression of heavy quarkonia mesons may signal towards a deconfined QGP state at high temperatures. At high density, the Debye screening in a QGP reduces the attractive force between heavy quarks as well as heavy quarks and antiquarks. Above certain critical density it prevents the formation of bound states. The bound states are expected to dissolve as the temperature of the system increases. In view of this, J/Ψ suppression is considered as one of the key probes of the formation of QGP in heavy ion collisions. Color screening has been proposed as a mechanism leading to anomalous suppression of the J/Ψ's beyond normal hadronic absorption. The CERN SPS experiments NA38, NA50 and NA60 were the first ones to investigate this by measuring the J/Ψ production in a variety of collision systems and energies. The results show a significant anomalous suppression in Pb+Pb [35] and In+In [36] collisions at SPS.

The PHENIX experiment at RHIC has also confirmed J/Ψ suppression in various collision systems and provides further insights by exploring this phenomenon at higher energies [37, 38, 39]. The ratio of J/Ψ yields for Au+Au and p+p collisions as given by R_{AA} (the nuclear modification factor), as a function of N_{part} is shown in Figure 1.13. The magnitude of suppression is greater than what is expected by extrapolating the CNM (Cold Nuclear Matter) effects measured in d+Au collisions [40]. We also observe that the suppression at mid-rapidity is similar to that observed in the SPS experiment and it is less than that in the forward rapidity region. This contradicts the local density induced suppression models since energy density at mid-rapidity is higher than that in the forward rapidity region. Furthermore the medium is more dense in RHIC than what is produced at SPS. A number of explanations, such as a sequential melting which includes dissociation of $\Psi^{'}$ and χ_c (leading to suppression of feed down components of J/Ψ yield), and gluon saturation (which leads to lower charm quark yield at forward rapidity), have been put forth. A strong regeneration of J/Ψ from uncorrelated c and $\overline{c}$ quarks is also a good candidate to explain the R_{AA}

as a function of rapidity.

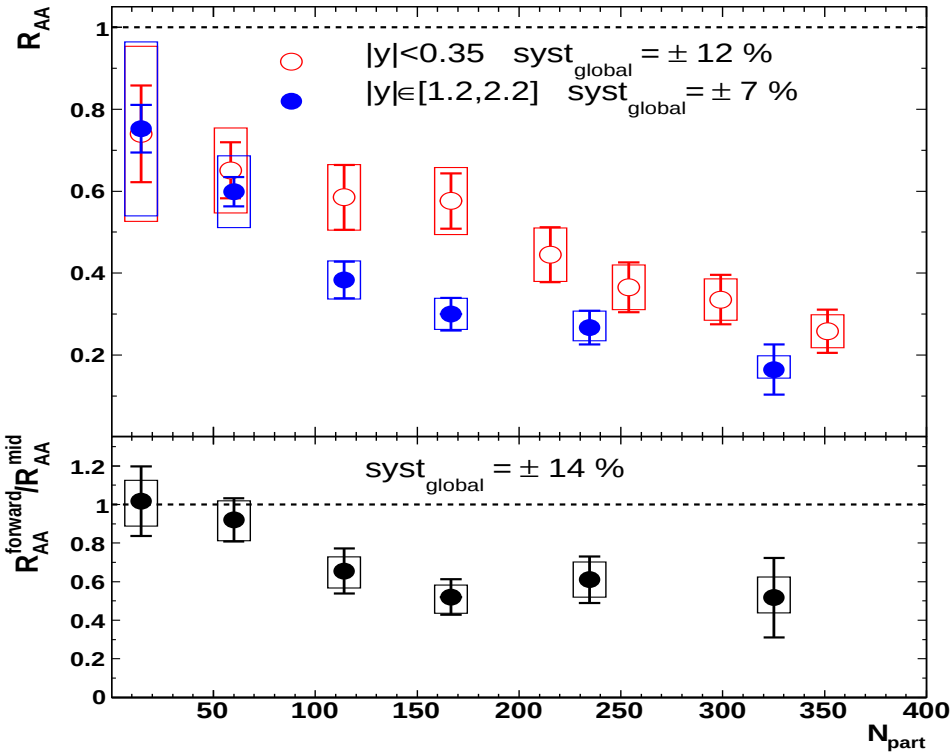

Figure 1.13: The J/ψ R_{AA} versus N_{part} for Au+Au collisions at 200 GeV. The open circles represent the mid-rapidity data. The lower panel depicts the ratio of J/ψ R_{AA} for forward rapidity to the same of mid-rapidity as a function of N_{part}.

1.3.6 Jet Quenching

As suggested by Bjorken [41], partons traversing through the bulk partonic matter can undergo significant energy loss. These partons can subsequently fragment into hadrons. The significant softening and broadening of jets, resulting from the fragmentation of the partons, while traversing through high density partonic matter, due to induced gluonic radiations, is called jet quenching [42, 8]. One of the major indicators of QGP is also the observation of jet quenching. It means, if the QGP is formed, then jets of final state baryons and mesons emitted from the plasma will loose some

of their energy due to strong interactions with the plasma (via gluon bremsstrahlung and scattering). In such a case one expects to see a suppression of particles with high transverse momentum.

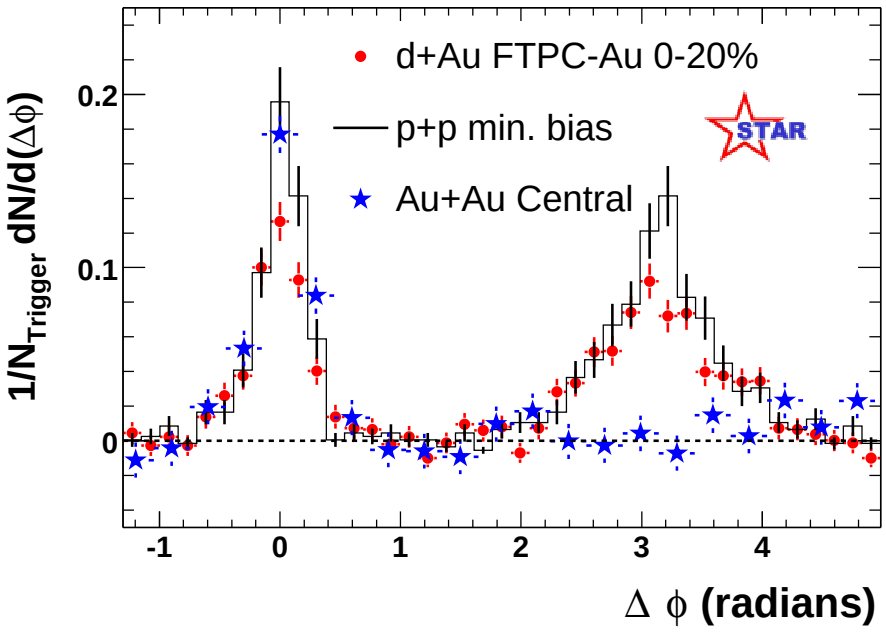

Figure 1.14: STAR measurements of di-hadron azimuthal correlations for p+p, d+Au and central Au+Au collisions [32, 43].

Figure 1.14 shows the data corresponding to STAR measurement of correlations of high p_T hadrons. It shows the azimuthal distributions of hadrons with $p_T > 2$ GeV/c. A hadron pair drawn from a single jet will generate an enhanced correlation at $\delta\phi \sim 0$ in case of p+p, d+Au and Au+Au collisions. On the other hand, a hadron pair drawn from two opposite jets of a di-jet event is expected to show an enhanced correlation at $\delta\phi \sim \pi$. However, such a correlation peak as observed for p+p and d+Au is broader than the near side correlation peak. For central Au+Au collisions this back to back correlation is seen to be absent while for peripheral collisions there is some back to back correlation with a strength similar to that of p+p collisions. This suppression in back to back correlation strength for di-jet events is due to final

Resonance	Decay Channel	Branching Ratio (%)	Width (MeV/c^2)	Life time (fm)	Strangeness
ρ^0 (770)	$\pi^+\pi^-$	∼100	150	1.3	0
K^* (892)	$K\pi$	∼100	50.7	4	±1
f_0 (980)	$\pi^+\pi^-$	∼67	40 to 100	2.6	0
ϕ (1020)	K^+K^-	49.2	4.46	44	0
Δ (1232)	$p\pi$	>99	∼120	∼ 1.6	0
Σ^* (1385)	$\Lambda\pi$	88.2	35.8	5.5	±1
Λ (1520)	pK	45	15.5	12.6	±1
Ξ^* (1530)	$\Xi\pi$	∼100	9.1	22	±2

Table 1.1: Mesonic and Baryonic resonances measured with the STAR experiment.

state interactions of the hard scattered partons or their fragmentation products in the dense medium created in Au+Au central collisions [32].

1.4 Resonances in Heavy ion collisions

A resonance or resonance state can be thought as a very short lived particle that decays via strong interaction. It carries a set of quantum numbers (spin, isospin, etc) like normal particles. It differs from regular particles in that its mass is smeared and has a width. This is based on uncertainty principle between time and energy which implies shorter the life time, the wider is the uncertainty in mass. Resonances have life times of the order of 1×10^{-23} seconds (usually denoted by 1 fm/c) and they are detected via their decay particles. Table 1.1 shows some resonances along with their decay channels, branching ratios, widths as well as life times studied with the STAR experiment.

1.4.1 Re-scattering and Regeneration Effect

As discussed earlier, during the expansion of the fireball, a stage is reached when the inelastic interactions among hadrons cease and this is known as the chemical

freeze-out. Kinetic freeze-out is reached when there is no further elastic interactions among the produced hadrons. As the resonances have very short life times ($\sim$ few fm/c), a fraction of them decay inside the medium before the thermal freeze-out. In such a case the hadronic decay daughter particles go through a period of elastic interactions with the hadrons in the medium. These interactions alter the momenta of the daughter particles. This effect which results in loss of reconstructed resonance signal is called the *re-scattering* of resonance daughter particles. However, after the chemical freeze-out, there can be pseudo-inelastic interactions among the hadrons in the medium, resulting in an increase in the resonance population. This is called the *re-generation* effect [44]. Therefore, both the resonance regeneration and primary production (unscattered resonances) contribute to the total yield of resonance signals detected. Measurement of the resonance yields can therefore serve as a tool to probe the time evolution of the system (from thermal to kinetic freeze-out) and to study the final state interactions in the hadronic medium [26, 45]. A schematic description of the re-scattering and regeneration effect of the K^* meson is shown in Figure 1.15.

1.4.2 K^* meson as a probe of dense medium created at RHIC

K^* meson is of particular interest due to its very short life time and its strange quark content. This makes K^* mesons sensitive to the properties of the dense matter. It allows one to study strangeness production from a possible early partonic phase [46, 47, 48]. Since the life time of K^* ($\sim 4fm/c$) is expected to be less than the lifetime of the system formed in heavy ion collisions [49], the K^* is expected to decay, re-scatter and regenerate all the way throughout kinetic freeze-out. Various in-medium effects due to the high density and high temperature of the medium such as dynamical interaction with the surrounding matter, the interference between different scattering channels, effects of phase space distortion due to re-scattering of particles and Bose Einstein correlations may result in modification of the characteristic properties of

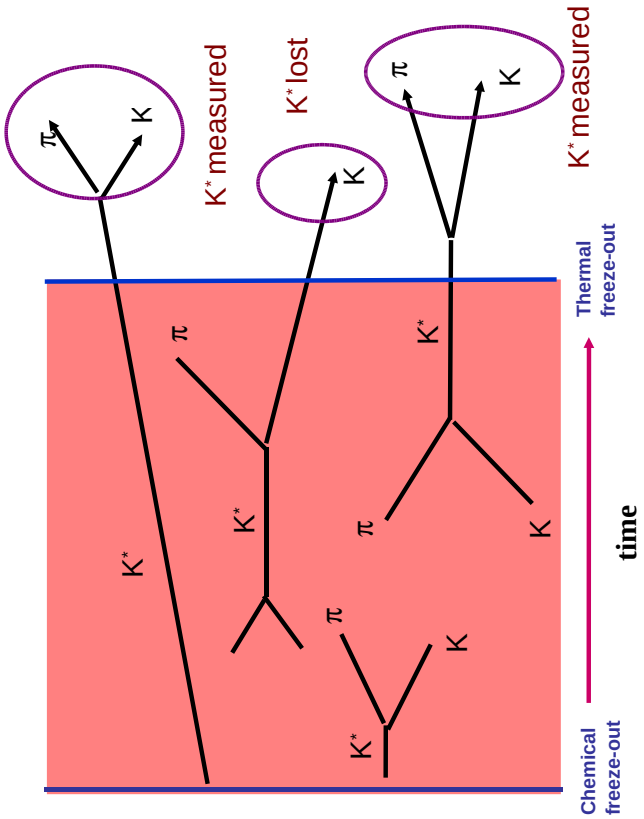

Figure 1.15: The re-scattering and regeneration effects of K^{*0} meson.

K^* [50]. Measurement of these properties such as mass, width, yield and transverse momentum spectra can provide insight for understanding the dynamics of the medium created in heavy ion collisions.

Since the total $\pi\pi$ interaction cross section [51] is about five times the total πK interaction cross section [52], the final observable K^* yield may decrease compared to the primordial yields. Hence a suppression in the K^*/K and/or K^*/ϕ yield ratios is expected in heavy ion collisions. These data can be compared with similar results obtained from elementary p+p collisions at similar collision energy to estimate a lower

limit of the time span between chemical freeze-out and kinetic freeze-out [46]. Further the system size, beam energy and centrality dependence of this suppression can be used to study the correlation of the life time with the size of the fireball.

The nuclear modification factors R_{AA} or R_{CP} of K^* meson are vital in differentiating between the mass and particle species ordering in particle production. Earlier STAR results on nuclear modification factor for various hadrons had supported the baryon-meson effect over the mass as per the predictions of quark coalescence model [46, 53]. In the intermediate p_T range, the nuclear modification factors, R_{CP} of Λ and K^0_S, as measured by STAR have been found to be different. These two particles have different masses. Further K^0_S is a vector meson while Λ is a baryon. Therefore it was not understood whether the observed differences in R_{CP} are due to mass or the particle types. In this scenario, when the mass of K^* is comparable to the mass of Λ baryon, it is interesting to compare the R_{CP} of K^* with those of K^0_S and Λ. This would help to distinguish whether the differences observed in R_{CP} of K^0_S and Λ are due to mass differences or differences in particle type.

In the intermediate p_T range, the elliptic flow parameter, v_2, for different hadrons shows a deviation from the particle mass ordering as seen in the low p_T regime [25, 54, 53]. The elliptic flow parameter, v_2, for the identified hadrons is found to follow a scaling with number of constituent quarks as explained by the quark coalescence model. K^* being a meson, its v_2 is expected to follow the scaling law of $n = 2$ where n is the number of constituent quarks. K^* produced via regeneration of kaons and pions during hadronisation, on the other hand, would follow the v_2 scaling of $n = 4$ [55]. STAR measurement of K^* v_2 had shown the number to be 3 ± 2 [46]. Due to large statistical uncertainties, it was inconclusive whether K^* production mechanism is via quark recombination or due to regeneration in the hadronic medium. The v_2 measurement in high statistics data for Au+Au collisions at 200 GeV would conclusively provides information about the K^* production mechanism in the intermediate

p_T range.

1.5 Scope and organisation of the thesis

The present thesis investigates the production of the strange mesonic resonance K^*, at mid rapidity, in Au+Au and Cu+Cu collisions at RHIC. The motivation for studying in Cu+Cu system is that it serves as a bridge between d+Au and Au+Au collisions in terms of number of participants, N_{part} and number of binary collisions, N_{bin}. In particular, looking at the data in terms of N_{part} offers the possibility of studying system size dependence of various bulk properties and may help to disentangle the initial state versus final state scenarios at RHIC. Through a comparison with similar data on other resonances, the evolution of the fireball formed in the collision is studied. The data used for the analysis presented in this thesis were taken with the STAR detector. Measurement of K^* yield, through its hadronic decay channel has been carried out, for all centralities, for Au+Au collisions at $\sqrt{s_{NN}} = 62.4$ GeV and Cu+Cu collisions at $\sqrt{s_{NN}} = 62.4$ GeV and 200 GeV. The invariant mass spectra of K^*, for various collision centralities, were reconstructed using standard techniques. The inverse slope parameters, and the yields for $0.3 \leq p_T \leq 3.0$ GeV/c, as determined from the above data, are compared for various centralities in different collision systems. The $\langle p_T \rangle$ for K^{*0} has been compared with the same for other stable particles (K, π and p) to investigate particle production mechanism.

The organization of the thesis is as follows, the RHIC complex and the STAR detector are presented briefly in Chapter 2. Chapter 3 deals with the analysis techniques along with the trigger conditions as used for determining various observables related to K^* meson. Results of the present analysis are presented in Chapter 4. This is followed by conclusions in Chapter 5.

Chapter 2

The STAR Experiment

2.1 Experimental Setup

2.1.1 Early Heavy Ion Accelerator Facilities

The Bevatron-Bevalac at Lawrence Berkley National Laboratory (LBNL) was the first facility to exploit relativistic nucleus-nucleus collisions at fixed target energies ranging up to 2 GeV per projectile nucleon. With the advent of Quantum Chromodynamics (QCD), the goal of locating and characterizing the hadron-parton deconfinement phase transformation suggested the necessity for collisions at higher energies. The interest in research thus shifted to the Alternating Gradient Synchrotron (AGS) at Brookhaven National Laboratory (BNL), Super Proton Synchrotron (SPS) at CERN, Relativistic Heavy Ion Collider (RHIC) at BNL finally heading towards Large Hadron Collider (LHC) at CERN. The AGS program at BNL allowed fixed target experiments of Au and S ion beams at top center of mass energies of 4.86 GeV. The RHIC at BNL is the first machine in the world, capable of colliding heavy ions at relativistic energies. It provides data on collisions of heavy nuclei and protons at center of mass energies ($\sqrt{s_{NN}}$) up to 200 GeV per nucleon pair which is about 10 times more than

what was achieved at previous fixed target experiments. These super fast and super hot collisions are likely to provide conditions of high temperature and high pressure to explore some of nature's most intriguing and exotic phenomena. The next large collider is LHC at CERN which is designed to collide p+p at 14 TeV and Pb+Pb beams up to $\sqrt{s_{NN}} = 5.5$ TeV. In the following sections we describe the RHIC experimental facility and the STAR detector.

2.1.2 Relativistic Heavy Ion Collider (RHIC)

RHIC's primary mission has been to accelerate and collide heavy ions and protons to create conditions that can take us back in time where we can observe how matter behaved when the universe originated immediately following the Big Bang. It is also capable of colliding spin polarized proton beams which will inform us about the gluonic contribution to the proton spin and many other interesting phenomena regarding spin physics. With RHIC, nuclear physics is expected to enter into the high-energy domain where the QCD structure of matter should be directly manifested in terms of the dynamics of quarks and gluons [56, 57].

Figure 2.1 shows the schematic diagram of the RHIC accelerator complex at BNL together with all other accelerators used to bring the heavy ions up to the RHIC injection energy. With two sources of ions (two Van de Graaffs or a Van de Graaff and proton linac), collisions of asymmetric ion species, such as protons on gold ions or light ions on gold can also be studied at RHIC. In the following we describe briefly how ions of Au are accelerated starting from the source. Negatively charged gold ions from the pulsed sputter ion source at the Tandem Van de Graaff are partially stripped of their electrons with a foil at the high voltage terminal, and then accelerated to the energy of 1 MeV/nucleon by the second stage of the Tandem. After a further stripping at the exit of the Tandem and a charge selection by bending magnets, beams of gold ions with a charge state of 32+ are delivered to the Booster Synchrotron and

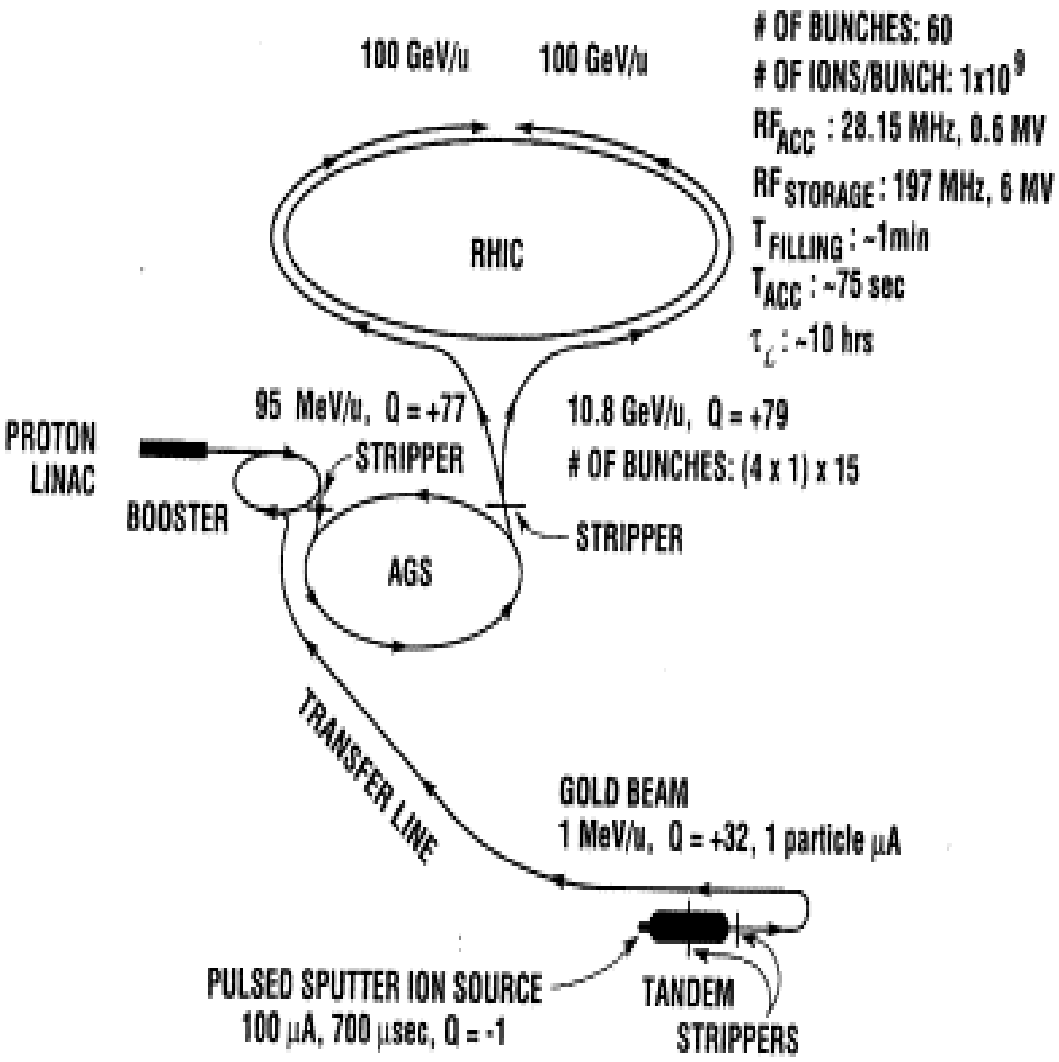

Figure 2.1: The Relativistic Heavy Ion Collider (RHIC) accelerator complex at Brookhaven National Laboratory.

accelerated to 95 MeV/nucleon. Ions are stripped again at the exit from the Booster to reach a charge state of 77+, and injected to the AGS for further acceleration to the RHIC injection energy of 10.8 GeV/nucleon. Gold ions, initially injected into the AGS in 24 bunches, are de-bunched and then re-bunched to four bunches at the injection front porch, prior to the acceleration. These four bunches are ejected at the top energy, one bunch at a time, and transferred to RHIC through the AGS-to-RHIC Beam Transfer Line. A further stripper at the exit of the AGS strips the Au ions to a final charge state of 79+ before injecting them into the RHIC rings. The stacking in the RHIC rings is done in a boxcar fashion [56].

The RHIC consists of two quasi circular, concentric storage rings with counter rotating beams. These independent rings have their sets of superconducting magnets which bend and focus the ions. The ring with the clock-wise rotating beam is called the Blue ring. The other ring with the counter clock-wise beam is called the Yellow ring. Once the beam is injected into the rings, the ion bunches are accelerated to 100 GeV/nucleon. For p+p collisions, protons are injected from the 200 MeV Linac into the booster, the AGS and finally the RHIC. The RHIC rings are positioned in the same horizontal plane and intersect at six locations which provide six interaction points for particle collisions. Four of these points are equipped with detectors. There are two large experiments *viz* STAR (Solenoidal Tracker at RHIC) at 6 o'clock position and PHENIX (Pioneering High Energy Nuclear Interaction Experiment) at 8 o'clock position. The other two small experiments which are recently decommissioned are BRAHMS at 2 o'clock and PHOBOS at 10 o'clock positions. This is shown in Figure 2.2.

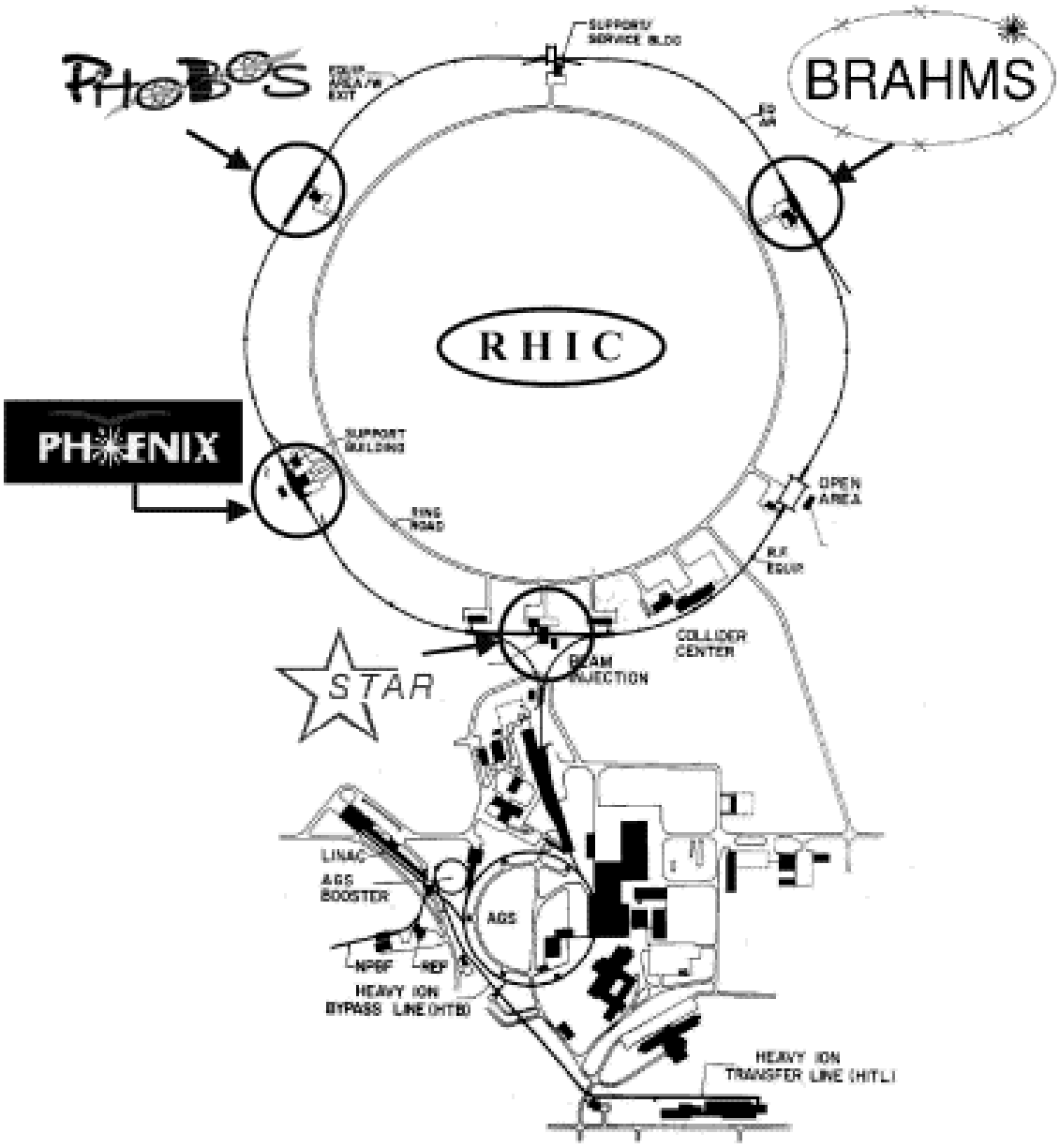

Figure 2.2: The arrangement of detectors along the RHIC ring [56].

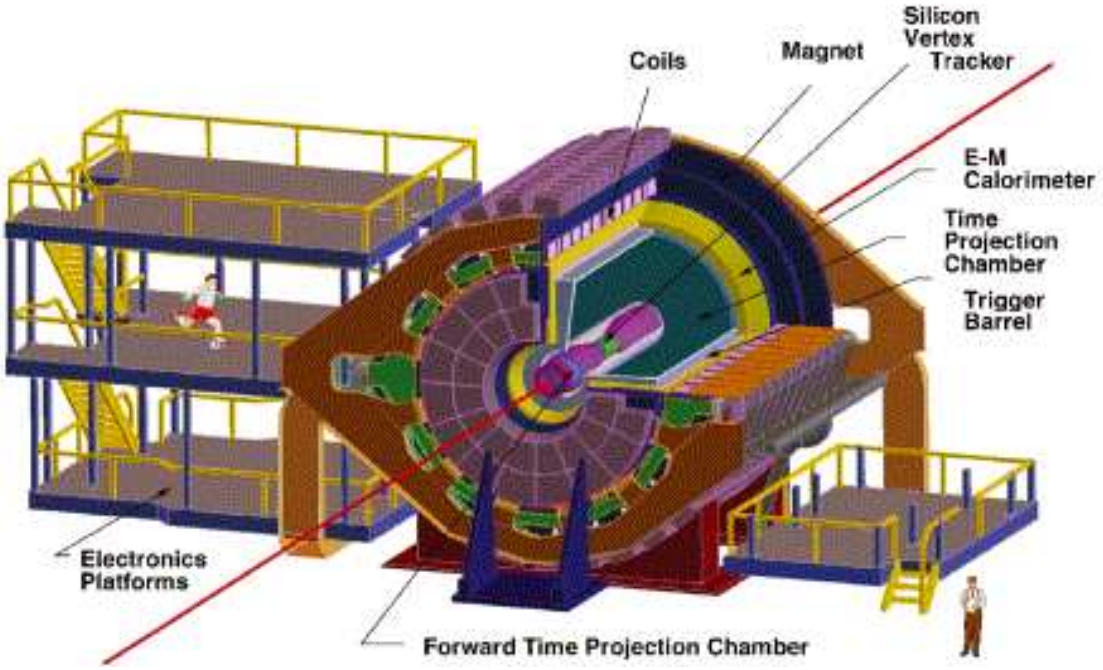

Figure 2.3: A perspective view of the STAR detector, with a cutaway for viewing inner detector systems [58].

2.2 The STAR Detector

The STAR detector system at RHIC [58] was constructed with the prime objective to study high density QCD using ultra-relativistic heavy ion collisions. It also aims at studies of p+p and p+A interactions to infer about the initial parton distribution functions of the incident nuclei. It also aims at an estimate of the gluonic contribution to the overall spin of the proton by accumulating information from polarized p+p collisions.

A cutaway perspective view of the STAR detector is displayed in Figure 2.3. A cut-away side view of the same is shown in Figure 2.4. The entire system is enclosed in a room temperature solenoidal magnet, with a uniform magnetic field of maximum value 0.5 T [59], for charged particle momentum analysis. The detector consists of various detector sub-systems for high precision tracking, momentum analysis, and

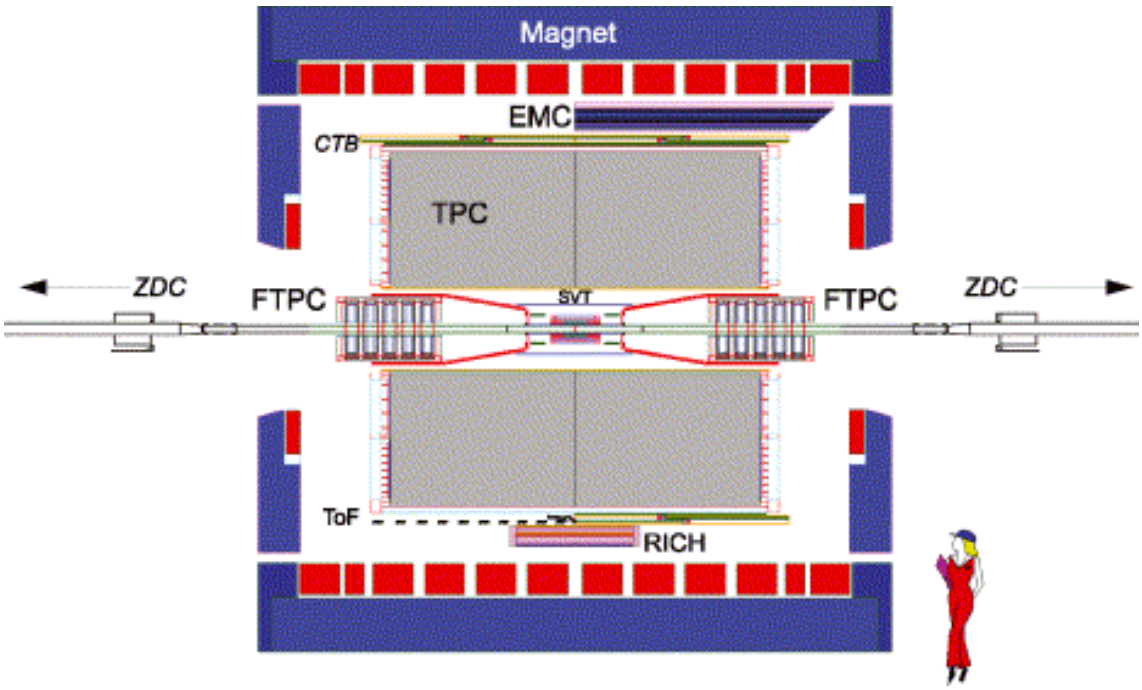

Figure 2.4: A cut-away side view of the STAR detector [58].

particle identification at mid-rapidity. The large acceptance of STAR is very much suitable for an event-by-event characterization of heavy ion collisions and the detection of hadron jets. Its primary tracking device is a large volume Time Projection Chamber (TPC) for charged particle tracking and particle identification [60]. This is described in Section 2.3. The TPC continues tracking out to 200 cm radial distance from the interaction region. A Silicon Vertex Tracker (SVT) [61] provides three layers of charged particle tracking near the interaction region. These three cylindrical layers consists of 216 silicon drift detectors. They have full azimuthal coverage with a pseudo-rapidity range, $|\eta| < 1$. This tracking, close to the interaction point, allows precision localization of the primary interaction vertex. Identification of secondary vertices is also achieved for weak decays of Λ, Σ and Ω particles. Particle identification is achieved using ionization energy loss, with an expected combined energy loss resolution (dE/dx) of 7%. The momentum resolution of the SVT and TPC reach a

value of $\delta p/p = 0.02$ for a majority of the tracks in the TPC. The resolution improves with an increase of the number of hit points along the track and with a decrease of the particle's momentum.

A two component, radial-drift TPC (Forward Time Projection Chamber) FTPC [62] is installed in the forward direction covering $2.5 < |\eta| < 4$ with complete azimuthal coverage and symmetry. It enables the tracking in the forward region. A ring imaging Cherenkov detector [63] covering $|\eta| < 0.3$ and $\Delta\phi = 0.11\pi$ and a Time-of-Flight (TOF) patch [64] covering $-1 < \eta < 0$ and $\Delta\phi = 0.04\pi$ have been installed to extend the particle identification to larger momenta over a small solid angle. A full-barrel electromagnetic calorimeter (BEMC) [65] and an endcap electromagnetic calorimeter (EEMC) [66] allow event-wise measurement of the transverse energy. They also act as trigger detectors for high transverse momentum photons, electrons, and electro-magnetically decaying hadrons. A set of shower-maximum detectors (SMD), inside the EMC, distinguishes high momentum single photons from photon pairs resulting from π and η meson decays. The EMCs also provide prompt charged particle signals essential to discriminate against pileup tracks inside the TPC, arising from other beam crossings falling within the 40 μs drift time of the TPC. A photon multiplicity detector (PMD) has been installed in the forward region at a distance of 540 cm from the interaction point [67]. With full azimuthal coverage and an η coverage from -3.8 to -2.4, PMD measures the photon multiplicity and spatial distribution on an event-by-event basis.

STAR Data Acquisition System (DAQ) combines custom VME-based receiver electronics with off-the-shelf computers in a parallel architecture interconnected with a Myrinet network [68]. Events of size 80 MB are processed at input rates up to 100 Hz. Events are reduced to 10 MB by zero suppression, performed in hardware, using custom-designed ASICs. A Level 3 Trigger [69] reconstructs tracks in real time and provides a physics-based filter to further reduce the sustained output data rate

to ∼30 MB/s. Built events are sent via Gigabit Ethernet to the RHIC Computing Facility (RCF) and stored in tape using HPSS.

2.2.1 Silicon Vertex Tracker

Silicon Vertex Tracker (SVT) is a three-barrel micro-vertex detector based upon silicon drift detector (SDD) technology. Besides improving the primary vertexing, the two-track separation resolution, and the energy-loss measurement for particle identification, the SVT also adds unique physics capabilities to STAR [61]. It enables the reconstruction of very short-lived particles (primarily the strange as well as multi-strange baryons and D-mesons) through secondary vertexing close to the interaction zone. For charged particles that do not reach the active volume of the TPC, due to the applied magnetic field, the SVT expands the kinematical acceptance to very low momentum by using independent tracking. In addition to the position resolution, the detector also provides an energy measurement on the basis of the charged particle energy loss (dE/dx) in each layer. Position resolutions of 20 μm as well as energy loss (dE/dx) measurements with a resolution of about 7% are achieved with the STAR-SVT.

2.2.2 Silicon Strip Detector

The STAR Silicon Strip Detector (SSD) provides a fourth layer of additional tracking detector surrounding the SVT, located inside the TPC [70]. The SSD is placed at a distance of 230 mm from the beam axis, covering a pseudo-rapidity range of $|\eta| < 1.2$. It has a total silicon surface are of $\sim 1\ m^2$. This detector enhances the tracking capabilities of STAR by providing two-dimensional hit position and energy loss measurements for charged particles. It improves the extrapolation of TPC tracks through SVT hits, increasing the average number of space points measured near the

collision point. This ensures better detection efficiency for long-lived meta-stable particles.

2.2.3 Barrel Electro-Magnetic Calorimeter

The STAR BEMC is positioned inside the Al coil of the STAR solenoid and covers a region $-1 < \eta < +1$ in pseudo-rapidity with full azimuthal coverage. It matches the full acceptance of TPC. This feature of BEMC allows STAR to trigger on and study rare, high p_T processes such as jets, leading hadrons, direct photons and heavy quarks. It provides large acceptance for photons, electrons, π_0 and η_0 mesons in all collision systems spanning polarized p+p to Au+Au collisions [65]. The BEMC design includes 120 calorimeter modules and is segmented into a total of 4800 towers. Each of the towers is projective and pointing back to the center of the interaction diamond. Each module consists of a lead-scintillator stack and a set of SMDs situated approximately 5 radiation lengths away from the front of the stack. The SMD is used to provide fine spatial resolution in a calorimeter which has segmentations (towers) significantly larger than an electromagnetic shower size. While the BEMC towers provide precise energy measurements for isolated electromagnetic showers, the high spatial resolution provided by the SMD is essential for π_0 reconstruction and direct γ as well as electron identification.

2.2.4 Forward Time Projection Chamber (FTPC)

In order to extend the phase space coverage of the STAR experiment to the region of $2.5 < |\eta| < 4.0$, two cylindrical FTPC's were constructed [62]. The increased acceptance improves the event characterization and allows the study of asymmetric systems. The full two-component system measures the momenta and production rates of charged particles. Each of the units is a 120 cm cylindrical structure, 75 cm in

diameter with a radial drift field. It has readout chambers located in five rings on the outer cylinder surface. This radial configuration improves the two track separation in the highest particle density region (close to the beam pipe). The FEE (Front End Electronics) boards are mounted on the back of readout chambers. The ionization electrons drift to the anode sense wires. The induced signals on the adjacent cathode surface are read out by 9600 pads (each of area $1.6 \times 20\ mm^2$). Curved readout chambers are used to keep the radial field as ideal as possible. The low electron diffusion and the radial drift principle results in the required 2-track separation of about 1 mm. The two FTPC's have 19,200 channels of electronics, capable of measuring the charge drifting to the readout chambers in short time samples. The FTPC's use a mixture Ar and CO_2 with $Ar : CO_2$::50:50. The track points are calculated from the charge distribution measured by the readout electronics. These track points are grouped to tracks which, together with magnetic field maps, can be used to get the particle momenta. Due to the high multiplicity, in a central Au+Au collision, event-by-event observables like $< p_T >$ and fluctuations of charged particle multiplicity can be studied.

2.2.5 Endcap Electromagnetic Calorimeter

The Endcap Calorimeter is installed in the west poletip of the STAR detector. It has a pseudo-rapidity coverage of $1 < \eta < 2$ over full azimuthal range. It is capable of detecting photons and electromagnetically decaying mesons. It also identifies electrons and positrons and acts to trigger on high energy particles [66]. The triggering capabilities and its coverage are crucial for the spin physics program in polarized p+p collisions. It includes a scintillating-strip SMD to provide fine granularity. This helps to distinguish the transverse shower characteristic of single photons versus the photon pairs coming from π^0 and η^0 decay. It is also useful in electron hadron discrimination correlating the electron hits with TPC tracks.

2.2.6 Photon Multiplicity Detector

A preshower Photon Multiplicity Detector (PMD) is installed on the east wall of the wide angle hall in STAR. It is designed to measure photon multiplicity in the forward region where high particle density precludes the use of a calorimeter. The inclusion of the PMD enhances the phase space coverage of STAR with photons considerably, in pseudo-rapidity range of $-3.7 \leq \eta \leq -2.4$ with full azimuthal acceptance [67]. The detector is based on a proportional counter design using $Ar + CO_2$ gas mixture (70% Ar and 30% CO_2). It measures the spatial distribution and multiplicity of photons on an event by event basis. This can probe critical phenomena near the phase boundary, leading to fluctuations in global observables like multiplicity and pseudo-rapidity distributions.

2.2.7 Trigger Detectors

The STAR Trigger, a 10 MHz pipelined system based on output from fast detector, is supposed to control the event selection for the much slower tracking detectors [71]. Trigger detectors are required to select the centrality of collisions in $A+A$ and $p+A$ interactions based on charged particle multiplicity in the TPC acceptance. In addition, they are required to select ultra-peripheral collisions, jet events and events based on bunch polarization. Also they select cosmic ray events useful for system debugging and calibration. These requirements have led to the development of a fast detectors based pipelined electronic system. The primary trigger detectors for STAR are the Central Trigger Barrel (CTB), the Zero Degree Calorimeters (ZDC), the Beam Beam Counters (BBC), a Forward Pion Detector (FPD) and the BEMC.

The CTB consists of 240 scintillator slats arranged in four cylindrical bands, each covering 1/2 unit of pseudo-rapidity. The slats surround the outer cylinder of the TPC and trigger on the flux of charged particles in mid-rapidity region. The

CTB selects central triggered events by measuring the occupancy of the slats. In order to provide some universal characterization of heavy ion collisions, all the four detectors have one common detector subsystem, namely a pair of ZDC's [72] that are located behind the beam-splitting point outside the DX magnets. Each ZDC is a small calorimeter, consisting of layers of tungsten plates and scintillator slabs. It detects neutron multiplicities from the heavy ion collisions, giving one of the collision centrality measures. The ZDC pair at each crossing point is also used as a luminosity monitor in steering the beams to the collision point. The BBC measures the beam jets at high rapidity from NSD (Non Singly Diffractive) inelastic p+p collisions. It covers $3.3 < |\eta| < 5.0$ in pseudo-rapidity. It has two sets of scintillating detectors positioned at the east and the west magnetic poletip of the STAR magnet. It has scintillating tiles arranged in a hexagonal close packing structure. The time difference between the two counters is used to locate the primary vertex position.

2.3 The Time Projection Chamber (TPC)

The STAR TPC is the primary tracking device that records the tracks of charged particles as they traverse the gas volume of the TPC. It measures the charged particle momenta and identifies the charged particles by measuring their ionization energy loss (dE/dx). It can identify charged particles over a momentum range from 100 MeV/c to greater than 1 GeV/c and can measure their momenta from 100 MeV/c to 30 GeV/c. The acceptance of TPC covers ± 1.8 units of η and with full azimuthal coverage ($0 < \phi < 2\pi$) over the full range of multiplicities [60].

A schematic of STAR TPC is shown in Figure 2.5. It consists of a 4.2 m long cylinder whose diameter is 4.0 m. The inner and outer radii of the active volume are 0.5 m and 2.0 m respectively and the cylinder is concentric with the beam pipe. A thin conductive Central Membrane (CM), held at a voltage of 28 kV, divides

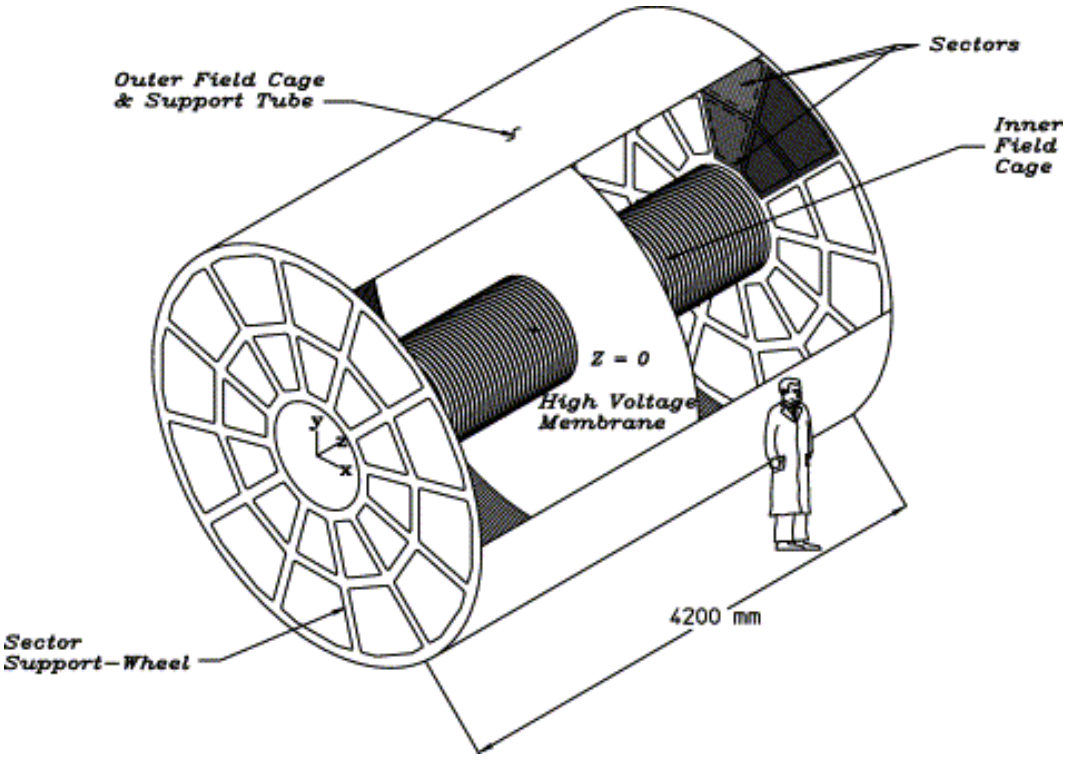

Figure 2.5: The STAR TPC surrounds a beam-beam interaction region at RHIC. The collisions take place at the center of the TPC [60].

the TPC into two equal halves. The working gas of the TPC is P10 which is a mixture of two gases (10% Methane and 90% Argon) regulated at a pressure of 2 mbar above the atmospheric pressure. A uniform electric field of 135 V/cm is maintained between the Central Membrane and the readout end caps. A chain of 183 resistors and equipotential rings along the concentric field cage cylinders help to maintain this uniformity of the electric field which is critical for uniform electron drift [60] .

The Central Membrane (CM), which forms the cathode, consists of a number of pie shaped, 70 μm thick carbon loaded kapton film. An outer support hoop mounted on the outer field cage keeps the CM taut and secured under tension. Attached on each side of the CM, there are 36 Al stripes which act as targets emitting electrons for the TPC Laser Calibration System [73]. Since the position of the narrow stripes are

precisely measured, the emitted electrons, which are photo-ejected when an ultraviolet laser beam hits a stripe, can be used for spatial calibration. The primary attribute of the P10 gas used in the TPC is its fast drift velocity which peaks at low electric field strengths. Operating at peak drift velocity allows more stability as small changes in temperature and gas pressure have negligible effects. The readout planes of the TPC are Multi-Wire Proportional Counter (MWPC) chambers with pad readout systems mounted on the support wheels. The complete readout system is divided into 24 sectors, each sector being further divided into an outer and an inner sub-sector. The outer sector has 32 large, densely packed, pad rows which enables one to get an optimized dE/dx resolution. The inner sector, which is a region of high track density, consists of 13 pad rows. It has small pads which are optimized for good position as well as momentum resolution [74].

2.3.1 Track Reconstruction

The TPC track reconstruction starts by identifying the three dimensional space coordinate points. When a charged particle traverses through the volume of the TPC, it ionizes the gas atoms and molecules along its path leaving behind a cluster of electrons. The $x-y$ position of each cluster is found by measuring the signal in adjacent pads. The drift time from point of origin of the cluster to the endcap is measured and the z-position of the cluster is determined by dividing the drift time by the average drift velocity. Once the positions of the clusters are found, a Time Projection Chamber Tracker (TPT) algorithm is used to reconstruct the tracks by a helical trajectory fit. Each track is a helix to first order, but there can be deviations from the helical shape due to energy loss in the gas and multiple Coulomb scattering. The resulting track information collected from the TPC together with additional tracking information from other inner detectors (SVT, SSD) are then re-fit by application of the Kalman Fit Method [75] to find a global track. The z-vertex of the primary

collision vertex is determined by extrapolating the trajectories of the reconstructed global tracks back to the origin. If a global track has a distance of closest approach (DCA) (with respect to the primary vertex), less than 3 cm, then the track is refitted to include the primary vertex as an additional space point. These tracks are called primary tracks. The reconstruction efficiency for primary tracks depends on the track quality cuts, particle type and track multiplicity.

2.3.2 Particle Identification (PID) using dE/dx

Identification of the charged particles can be achieved by TPC through their energy loss (dE/dx) due to interactions in the medium inside the TPC. As the ionization fluctuations are large and the length over which the particle energy loss is measured is short, it is not possible to measure the average dE/dx accurately. Hence we measure the most probable dE/dx. This is done by removing 30% of the largest ionization clusters and then calculating the truncated mean of the remaining clusters. Figure 2.6 shows the energy loss (dE/dx) vs particle momentum (p) for tracks in the TPC. The TPC dE/dx resolution of around 7-8% allows identification of charged pions and kaons up to about a transverse momentum of 0.75 GeV/c. Protons and anti-protons can be identified up to about 1.1 GeV/c. The different solid lines in the figure represent the Bethe-Bloch distributions corresponding to different particle species [76]. The particle identification can be quantitatively described by the variable N_σ , which corresponds to the standard deviation of a Gaussian between the measured track and its expected value. $N_{\sigma\pi}$ (in case of pions), is defined as:

$$N_{\sigma\pi} = \frac{1}{R} \log \frac{dE/dx_{measured}}{< dE/dx >_\pi} \tag{2.1}$$

where $(dE/dx)_{measured}$ is the measured energy loss for a pion track, $< dE/dx >_\pi$ is the expected mean energy loss for a pion track at a given momentum [77] and R is

the dE/dx resolution which is around 8.1%.

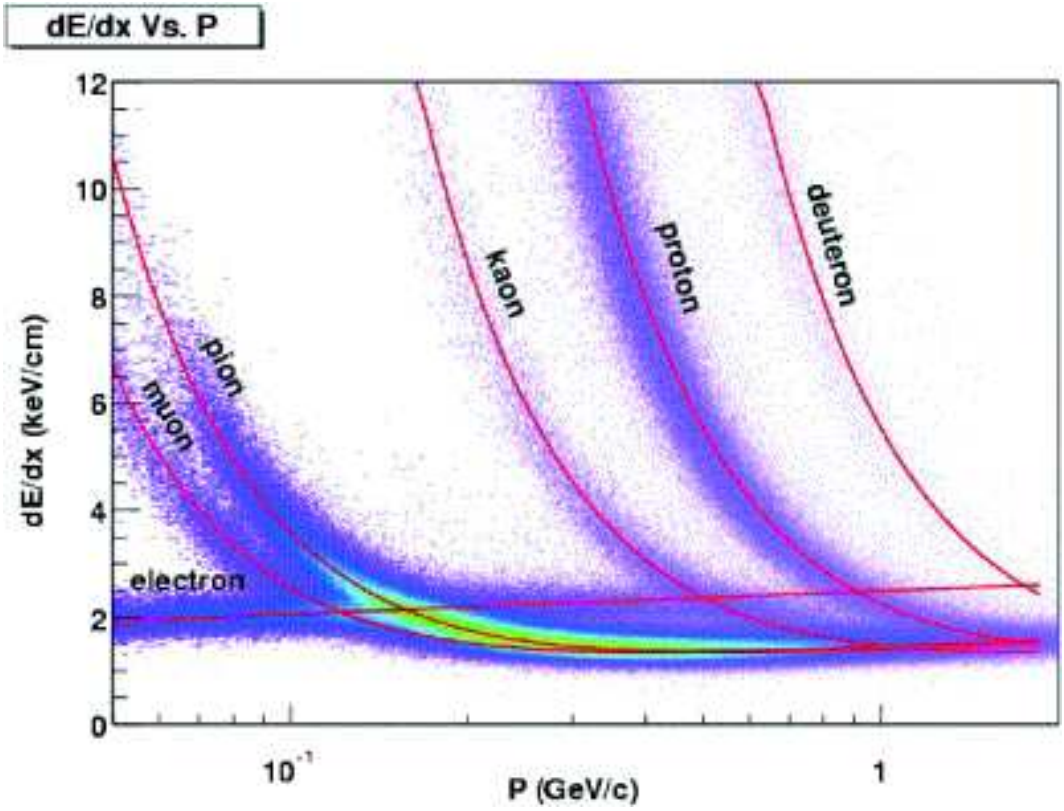

Figure 2.6: The energy loss distribution for charged particles in the STAR TPC as a function of momentum. The magnetic field was 0.25 T. The figure is taken from [60].

Chapter 3

The $K^*(892)$ Resonance Production in Au+Au and Cu+Cu Collisions at 62.4 GeV and 200 GeV

3.1 Data Analysis

3.1.1 Trigger

The dataset used in the presented analysis is from Au+Au collisions at $\sqrt{s_{NN}} = 62.4$ GeV and Cu+Cu collisions at $\sqrt{s_{NN}} = 62.4$ GeV and 200 GeV. The data were taken from the 2004 Au+Au RunIV and 2005 Cu+Cu RunV at RHIC using the STAR detector [58]. The primary tracking device, TPC (Time Projection Chamber) was used to measure the K^* production through the detection of its hadronic decay products (K, π). The TPC provides particle identification and momentum information of the charged particles by measuring their ionization energy loss dE/dx [60]. The dataset

corresponding to $Au+Au$ collisions at $\sqrt{s_{NN}} = 62.4$ GeV consisted of minimum-bias (MB) events only. The MB trigger, requiring coincidences between the two Zero Degree Calorimeters (ZDC) located in the beam direction at $\theta < 2$ mrad, was used in data selection. The MB events were chosen according to the raw charged track multiplicity within a pseudo-rapidity window $|\eta| < 0.5$, corresponding to 0-80 % of the total measured cross section. As the ZDC's were inefficient for central events, the combination of ZDC and the Beam Beam Counter (BBC) was used to provide the MB trigger for $Cu+Cu$ collisions at 62.4 GeV.

3.1.2 Event Selection

The analysed events were required to have a primary vertex Z position, V_Z within $\pm$ 30 cm from the center of the TPC, along the beam line. This was taken roughly to ensure uniform acceptance in the η range studied. Figure 3.1 shows the V_Z distribution for the different collision systems. The collision centrality is defined in accordance with the fraction of the charged particle reference multiplicity distribution within the pseudo-rapidity window $|\eta| < 0.5$ for all events. We have four centrality bins 0-20%, 20-40%, 40-60% and 60-80% for $Au+Au$ collisions at 62.4 GeV. The $Cu+Cu$ events in both 62.4 GeV and 200 GeV collisions were divided into three centality bins i.e 0-20%, 20-40% and 40-60%. The most peripheral events were not taken into account due to large trigger and vertex finding inefficiencies. Table 3.1 lists the uncorrected reference multiplicity ranges for different centrality bins in the datasets used. The approximate number of events analysed after imposing the mentioned event cuts are presented in Table 3.2.

Collision systems	Centrality Bin	Uncorr.RefMult Range
Au+Au(62.4 GeV)	0-20%	≥ 222
	20-40%	$102 \leq$ TPCRefMult < 222
	40-60%	$38 \leq$ TPCRefMult < 102
	60-80%	$9 \leq$ TPCRefMult < 38
Cu+Cu(62.4 GeV)	0-20%	≥ 71
	20-40%	$33 \leq$ TPCRefMult < 71
	40-60%	$14 \leq$ TPCRefMult < 33
Cu+Cu(200 GeV)	0-20%	≥ 98
	20-40%	$46 \leq$ TPCRefMult < 98
	40-60%	$19 \leq$ TPCRefMult < 46

Table 3.1: Centrality definitions for different uncorrected reference multiplicity ranges.

Collision systems	Centrality	$\|V_Z\|$ cm	Events
Au+Au(62.4 GeV)	0-80%	30	7×10^6
Cu+Cu(62.4 GeV)	0-60%	30	8.1×10^6
Cu+Cu(200 GeV)	0-60%	30	1.95×10^7

Table 3.2: List of datasets used in the analysis. Cuts on V_Z, centrality range selected and number of events used are also shown.

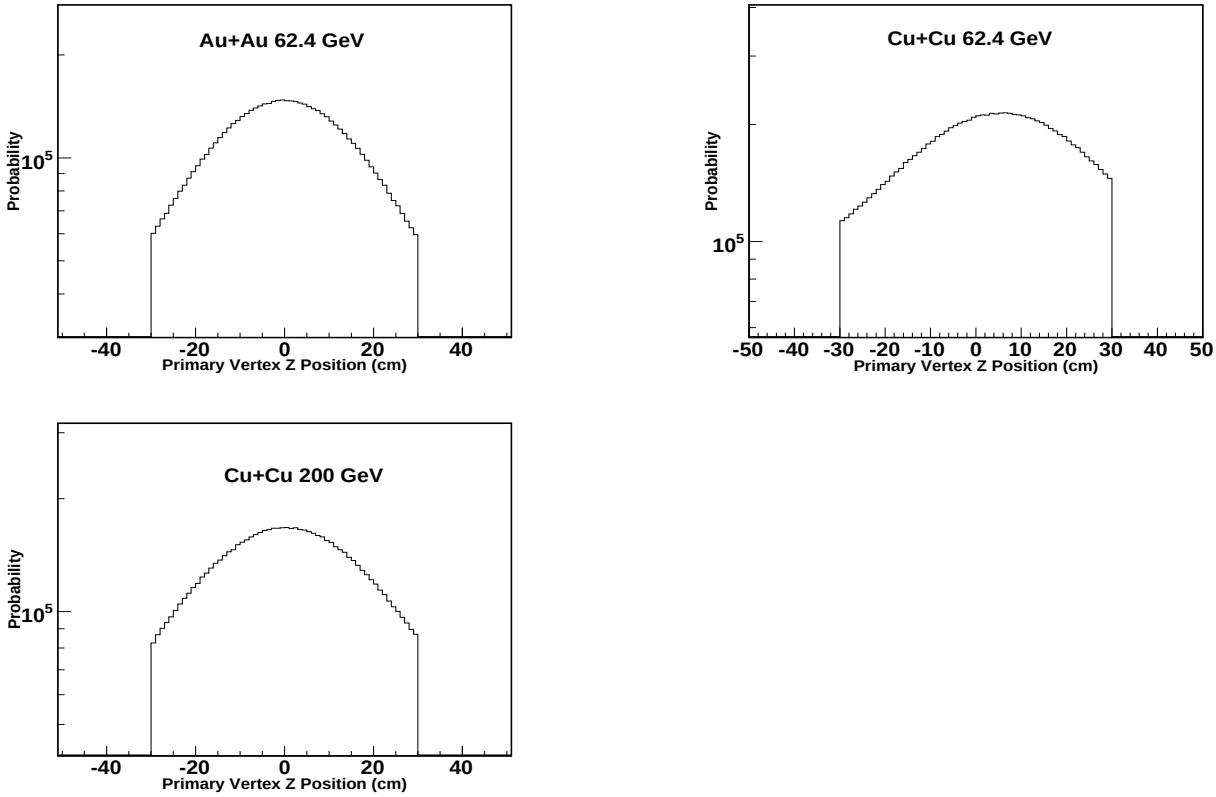

Figure 3.1: Z position of primary vertex for different data sets.

3.1.3 Track Selection

In the present analysis, the tracks used in all the datasets are primary tracks. To ensure optimal momentum resolution and particle identification, various quality cuts are required to be applied to each track measured in the TPC. In this analysis, K^{*0} mesons are detected through their hadronic decay channels i.e. $K^{*0} \rightarrow K^{+}\pi^{-}$ and $\overline{K^{*0}} \rightarrow K^{-}\pi^{+}$, using charged tracks measured inside the TPC. To improve statistics, K^{*0} and $\overline{K^{*0}}$ yields were combined to get the final result. Therefore, K^{*0} yield, in this analysis, refers to the average of K^{*0} and $\overline{K^{*0}}$ unless otherwise specified. Since K^{*0} decays within a very short time, its daughter particles seems to originate from the primary interaction point. For the K^{*0} reconstruction, charged kaons and pions whose

distances of closest approach (DCA) to the primary vertex were less than 1.5 cm, were selected. These charged kaons and pions were selected by requiring their dE/dx to be within two standard deviations (2σ) of the expected value ($|N_{\sigma K}|, |N_{\sigma\pi}| < 2$), as shown earlier in section 2.3.2. Further to assure good track fitting and good momentum, as well as dE/dx resolutions, the TPC tracks for both these particles, were required to have atleast 15 fit points (number of measured TPC hits used in track fit from a maximum of 45 fit points) inside the TPC. Also the ratio of the number of fit points to the number of maximum possible fit points was required to be greater than 0.55. This was done for all the candidate tracks to avoid any selection of split tracks. In order to avoid the acceptance drop in the high η range, all the candidate tracks were required to have $|\eta| < 1.0$. To improve statistics, kaon and pion tracks were selected with both momentum and transverse momentum (p_T) up to 10.0 GeV/c.

The charged K^* first decays to produce a K^0_S and a charged pion known as charged K^* daughter pion. The produced K^0_S decays through weak interaction into $\pi^+\pi^-$ with $c\tau$ = 2.67 fm. These two oppositely charged pions from K^0_S decay are known as grand-daughter pions. Daughter pions for the charged K^* reconstruction were required to originate from the interaction point and pass through the same analysis cuts as required by that of neutral K^*. The K^0_Ss were reconstructed through the decay topology method [79, 80] used earlier in the STAR data analysis. In this, a reconstruction chain called V_0 finder is used to identify the K^0_S particles. All pairs of oppositely charged pions tracks are extrapolated to see if they originate from a secondary vertex, representing the two-body decay topology of neutral K^0_S. The geometric cuts applied with the V_0 finder are illustrated in Figure 3.2. The main cuts applied are on the parameters shown *viz* the distance of closest approach (DCA) between the primary interaction vertex and the secondary decay vertex (DCA-V0), DCA between the primary vertex and the DCA of the charged decay tracks (DCA-Pos

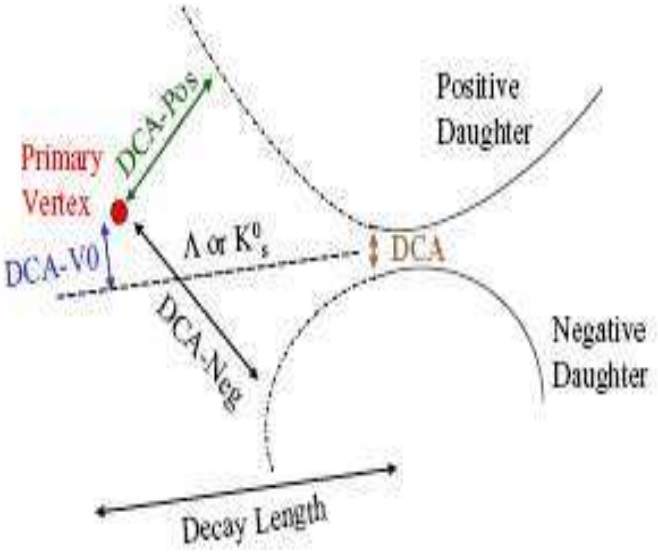

Figure 3.2: Schematic representation of K^0_S decay with the corresponding parameters used to identify the K^0_S particle [78].

and DCA-Neg for positive and negative charged tracks, respectively), DCA between the two charged tracks and finally the decay length. Upper and lower limits on these DCAs are applied to improve the signal of V_0 particles by minimizing the background contribution. The backgrounds are due to finite momentum resolution of the tracks in the TPC and a large number of fake secondary vertices resulting from primary tracks crossing each other. Since in the initial reconstruction chain the applied cuts are loose to accommodate different analysis needs, further cuts are applied to extract a clean sample of true V_0 particle (K^0_S).

The grand daughter charged pions, as required for the above K^0_S reconstruction, were selected from the global tracks with a DCAs to the interaction point greater than

Cuts	K^{*0}	$K^{*\pm}$ Daughter π	$K^{*\pm}$ K^0_S
$N_{\sigma K}$	(-2.0, +2.0)		$DecayLength > 2.0cm$
$N_{\sigma\pi}$	(-2.0, +2.0)	(-2.0, +2.0)	$dcaDaughters < 1.0cm$
Kaon p (GeV/c)	(0.2, 10.0)		$dcaV0PrmVx < 1.0cm$
Kaon $p_T(GeV/c)$	(0.2, 10.0)		$dcaPosPrmVx < 0.5cm$
Pion p (GeV/c)	(0.2, 10.0)	(0.2, 10.0)	$dcaNegPrmVx < 0.5cm$
Pion $p_T(GeV/c)$,	(0.2, 10.0)	(0.2, 10.0)	$M_{K^0_S}$ (GeV/c^2) : (0.48, 0.51)
NFitPnts,	> 15	> 15	$\pi^+ : NtpcHits > 15$
$NFitPnts/MaxPnts$,	> 0.55	> 0.55	$\pi^- : NtpcHits > 15$
Pseudo-rapidity η,	$\lvert\eta\rvert < 1.0$	$\lvert\eta\rvert < 1.0$	
DCA cm,	< 1.5 cm	< 1.5 cm	
Pair y	$\lvert y\rvert < 0.5$		$\lvert y\rvert < 0.5$

Table 3.3: List of track cuts for charged kaons, charged pions and topological cuts for $K^{*\pm}$ used in the K^* analysis in *Au+Au* and *Cu+Cu* collisions at 62.4 GeV and 200 GeV.

0.5 cm. In order to reduce the combinatorial background in the above reconstruction, the DCA between the pions was required to be less than 1.0 cm with each neutral vertex formed (DCA-V0) within 2 cm from the primary vertex position. Only the K^0_S signal for which the $\pi^+\pi^-$ invariant mass remained within 0.48 GeV/c to 0.51 GeV/c were selected. A typical invariant mass spectrum of K^0_S obtained this way is shown in Figure 3.3. The reconstructed K^0_S momentum vector is then required to point back to the primary vertex through a straight line. This is again to be paired up with pion tracks to get the charged K^* signal. For this $K\pi$ pairs with their parent rapidity (y) of $|y| < 0.5$ were selected. All the cuts used for the K^* reconstruction are summarised in Table 3.3.

3.1.4 K^* Reconstruction

In a typical collision event, several thousand tracks originate from the primary collision vertex. The decay daughters of K^{*0} are indistinguishable from other primary tracks. The K^{*0} was reconstructed by calculating the invariant mass for each $K\pi$ pair

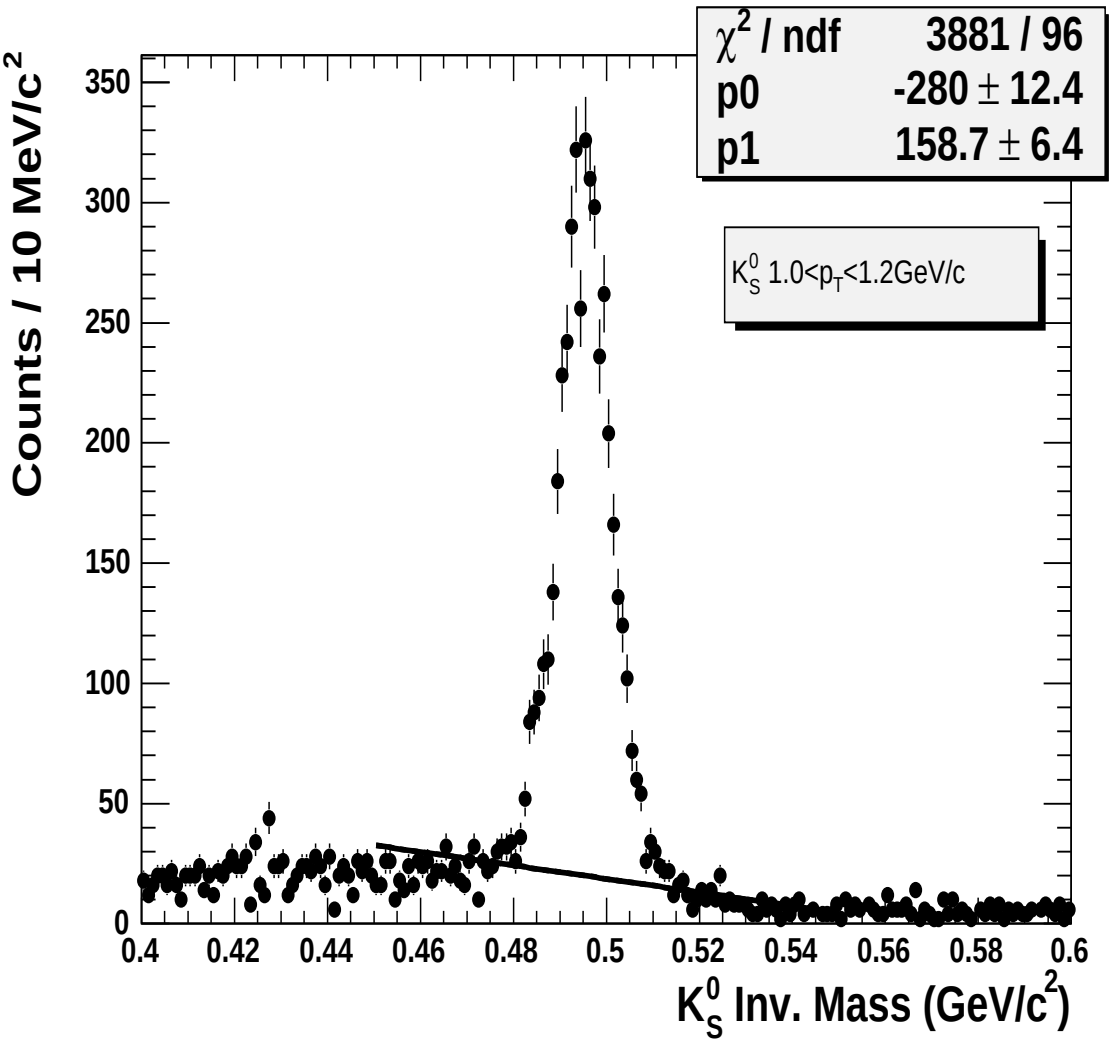

Figure 3.3: The K^0_S invariant mass distribution in Cu+Cu collisions at $\sqrt{s_{NN}}$= 62.4 GeV.

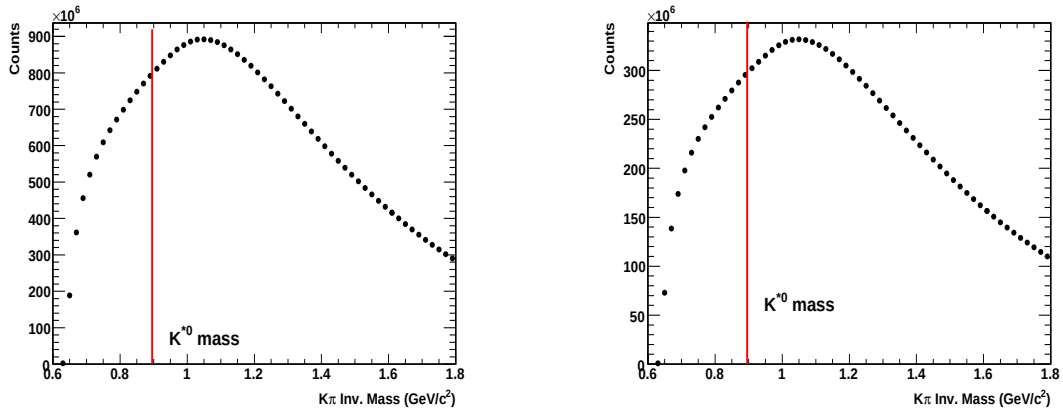

Figure 3.4: **Left Panel** $K\pi$ invariant mass distribution in Au+Au system (62.4 GeV). **Right Panel** $K\pi$ invariant mass distribution in Cu+Cu system (200 GeV). The solid symbols represent counts in the same-event pair.

in an event. Figure 3.4 shows the invariant mass distribution from the same event pairs in Au+Au collisions at 62.4 GeV and Cu+Cu collisions at 200 GeV. This pairing is done by randomly selecting the kaon-pion pairs and hence they are mostly uncorrelated. The true K^{*0} signal constitutes a very small fraction of the total invariant mass spectrum. Therefore, one must subtract the large combinatorial background from the same-event spectrum to observe the K^{*0} signal. The mixed-event technique [81, 82] was used to built the combinatorial background. This technique has earlier been successfully applied to various resonances detected at RHIC. Here, the reference background distribution was built with uncorrelated, unlike sign, Kπ pairs from different events. The data sample was divided into 10 bins in multiplicity and 10 bins in collision vertex position, V_Z along the beam direction. The pairs from events in same multiplicity and V_Z were selected for mixing. This was done to ensure that the event characteristics remained similar between different events. In the present analysis the number of events to be mixed was chosen to be 5. However, the mixed event spectrum thus generated needed to be normalized before its subtraction from the same-event unlike-sign invariant mass spectrum. The normalization factor was

calculated by taking the ratio between the number of entries in the same event spectrum and the mixed event distributions with invariant mass greater than 1.2 GeV/c. This was done because Kπ pairs are less likely to be correlated in the region greater than 1.2 GeV/c. Figure 3.5 shows the same event Kπ invariant mass spectrum and the mixed event Kπ spectrum after normalization.

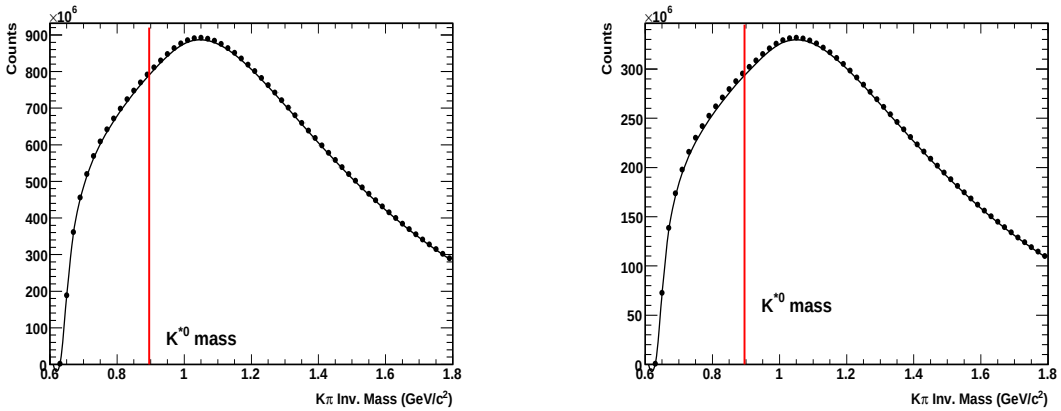

Figure 3.5: **Left Panel** *Au+Au* system at 62.4 GeV. **Right Panel** *Cu+Cu* system at 200 GeV. The $K\pi$ invariant mass distribution is shown for the mentioned systems. The solid symbols represent the same-event pair and the solid curve represent mixed-event pair.

The background subtraction and normalization of the same-event spectrum to get the true resonant signals, as mentioned above, can be written in the following form.

$$N_{K^{*0}}(m) = N_{K_1^+\pi_1^-}(m) + N_{K_1^-\pi_1^+}(m) - R \times \sum_{i=2}^{6}[N_{K_1^+\pi_i^-}(m) + N_{K_1^-\pi_i^+}(m) + N_{K_i^+\pi_1^-}(m) + N_{K_i^-\pi_1^+}(m)] \quad (3.1)$$

where, N stands for the number of $K\pi$ pairs in a bin, having bin center at m, R representing the normalization factor. After subtracting the normalized mixed event background (from the unlike-sign, same-event spectrum), we observe the K^* signal. A typical result is shown in Figure 3.6.

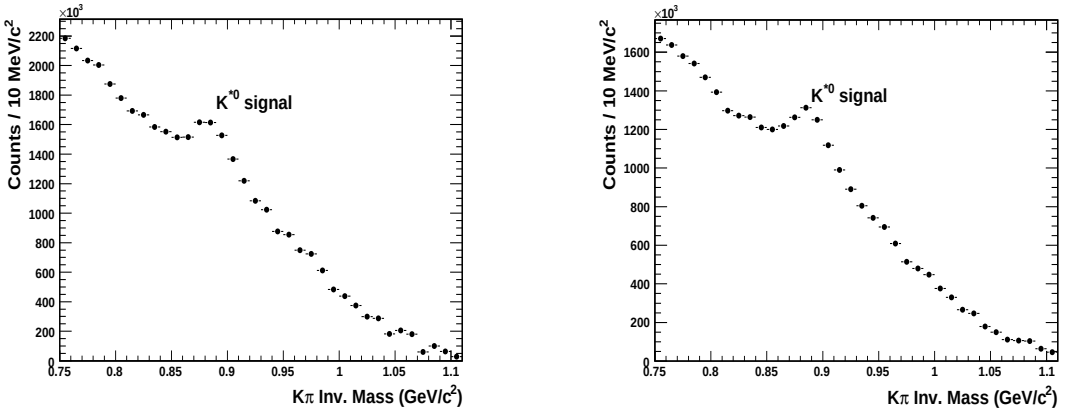

Figure 3.6: **Left Panel** *Au+Au* collisions at 62.4 GeV. **Right Panel** *Cu+Cu* collisions at 200 GeV. The $K\pi$ pair invariant mass spectrum after mixed-event background subtraction.

In the unlike-sign spectrum, we also have higher and/or lower $K\pi$ mass resonant states and non-resonant correlations. These are due to particle mis-identification and effects coming from elliptic flow in non-central collisions. These effects contribute significantly to the residual correlations observed near the true signal [83, 84]. In the same-event spectrum, there are correlated $K\pi$ pairs from other higher mass resonant states which decay into a K and a π. These attributes are not present in the mixed event spectrum and thus background subtraction using the mixed event spectrum only removes the uncorrelated background pairs from the unlike-sign spectrum.

3.2 Invariant Yield, Mass and Width Extraction for K^*

3.2.1 Fitting Function used for K^*

The raw K^* invariant mass distribution, obtained for different centralities were then fitted with a Simple Briet-Wigner (SBW) function riding over a linear background. The SBW function to be fitted is [85] given by

$$SBW(M_{K\pi}) = \frac{A\Gamma_0}{(M_{K\pi} - M_0)^2 + \frac{\Gamma_0^2}{4}} \tag{3.2}$$

where A is the area of Breit-Wigner distribution corresponding to the yield of K^* signal, $M_{K\pi}$ is the $K\pi$ invariant mass, M_0 is the natural K^{*0} mass and Γ_0 corresponds to natural width of K^{*0} .

As can be seen in Figure 3.6, there is a certain amount of residual background coming from unaccounted correlations mentioned in earlier section. This can be described by a linear function as given by

$$RBG(M_{K\pi}) = BM_{K\pi} + C \tag{3.3}$$

We can combine the above equation with equation (3.2) for SBW($M_{K\pi}$) to obtain the complete function to fit the $K\pi$ invariant mass spectrum. This is given as

$$f(M_{K\pi}) = SBW(M_{K\pi}) + RBG(M_{K\pi}) \tag{3.4}$$

where A, B, C, M_0 and Γ_0 are five open parameters of the fit. The mass and the full width of K^* can be extracted from the fit.

Figure 3.7 shows the mid-rapidity $K\pi$ invariant mass spectrum fitted to Equation 3.4 in *Au+Au* system at 62.4 GeV. The same is depicted for *Cu+Cu* system at 200 GeV in Figure 3.8. Figure 3.9 shows the $K^0_S\pi$ invariant mass spectrum in the mid-rapidity region for minimum-bias *Cu+Cu* collisions at 62.4 GeV.

In order to obtain the yield, mass and width of K^{*0}, as a function of p_T, we have to carry out all the above calculations for different p_T-bins. The invariant mass distributions in different p_T-bins for all centralities for *Au+Au* and *Cu+Cu* collisions are shown later in Figures 3.17 - 3.26.

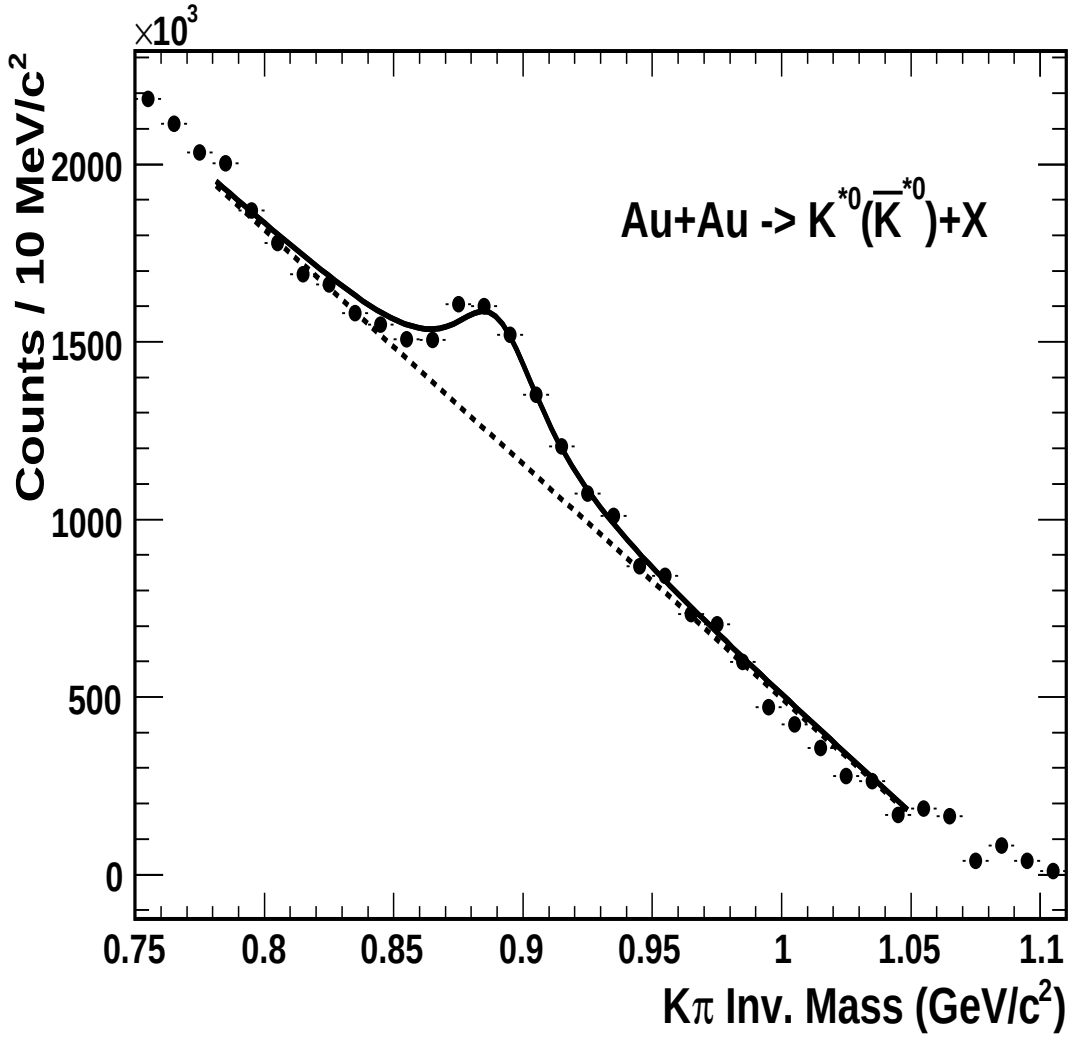

Figure 3.7: The $K\pi$ invariant mass distribution fitted to eqn. 3.4 to extract the K^{*0} yield in Au+Au collisions at $\sqrt{s_{NN}}$= 62.4 GeV. The solid curve represents the simple Breit-Wigner fit to the data points with a linear background as given by the dashed line (eqn. 3.3).

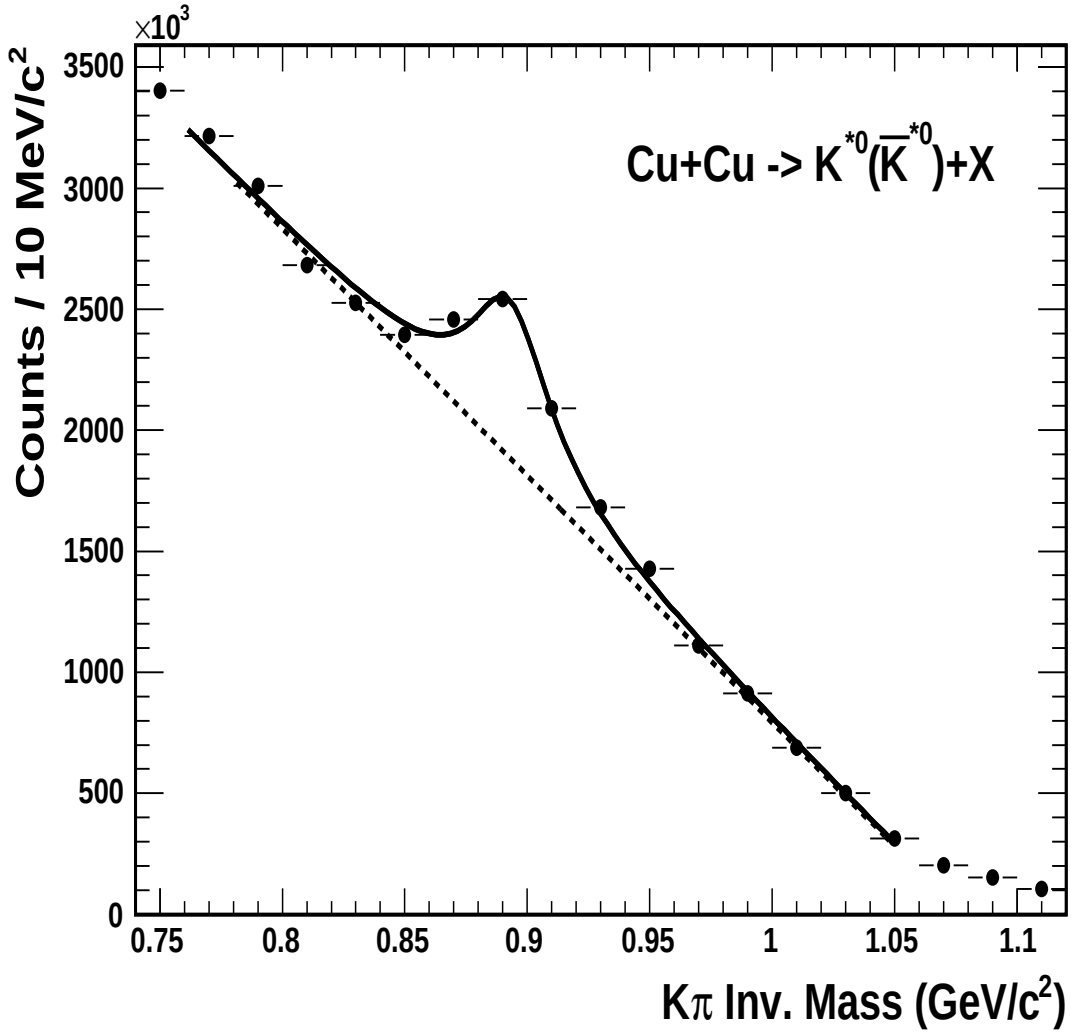

Figure 3.8: The $K\pi$ invariant mass distribution fitted to eqn. 3.4 to extract the K^{*0} yield in *Cu+Cu* collisions at $\sqrt{s_{NN}}$=200 GeV. The solid curve represents the Breit-Wigner fit to the data points with a linear background as given by the dashed line (eqn. 3.3).

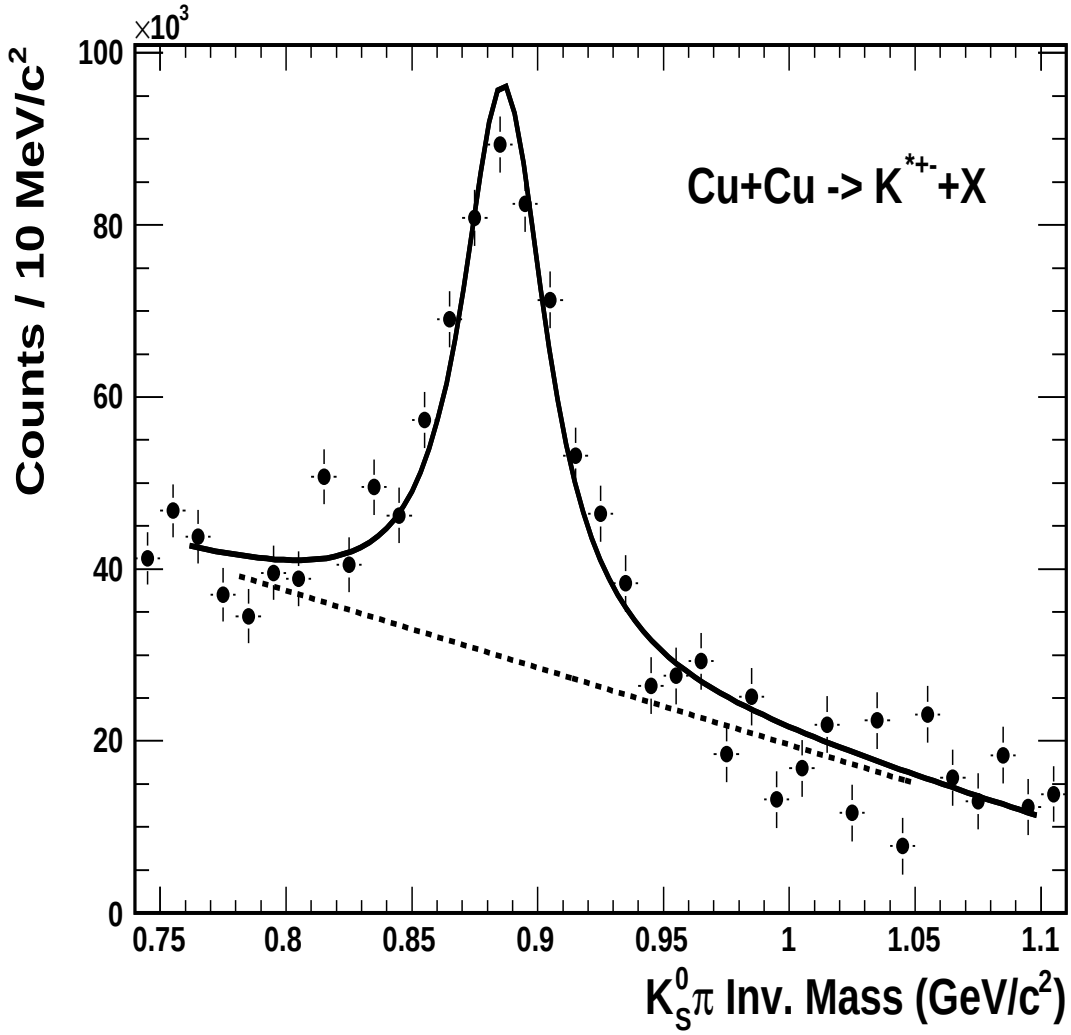

Figure 3.9: The $K^0_S\pi$ invariant mass distribution fitted to eqn. 3.4 to extract the K^{*+-} yield in *Cu+Cu* collisions at $\sqrt{s_{NN}}$= 62.4 GeV. The solid curve represents the Breit-Wigner fit to the data points with a linear background as given by the dashed line (eqn. 3.3).

3.2.2 Efficiency Correction

The raw K^{*0} and $K^{*\pm}$ yields, as obtained for various p_T-bins, need to be corrected for detector acceptance, detector response, tracking efficiency, and dynamical cut effects. All these constitute the reconstruction efficiency. The reconstruction efficiency factors are determined by comparing the results with the results obtained from Monte Carlo (MC) simulations.

MC simulated K^* mesons are generated using a flat p_T and rapidity distribution. They are then passed through GSTAR (the framework software package to run the STAR detector simulation using GEANT [86, 87] and TRS (TPC Response Simulator) [86]. The K^* mesons were then decayed by GEANT through their hadronic decay channel, $K^{*0} \rightarrow K\pi$ and $K^{*\pm} \rightarrow K^0_S\pi^{\pm}$. The simulated K^* mesons and their decayed daughters are then embedded into the real raw event. This combination of real and simulated data was then passed through the standard STAR reconstruction chain subjected to the same analysis cuts that were applied in the real data analysis. After reconstruction of the complete event, known as reconstructed event we head towards Association. The process of matching or associating the reconstructed information of decay daughters of K^* meson with the MC information is called Association. A cut of 10 common hit points was applied on the number of common hit points in the TPC for both the reconstructed and the input simulated tracks. The ratio of the reconstructed K^* mesons to the input K^* meson is the (efficiency $\times$ acceptance) factor.

Figure 3.10 and 3.11 shows a comparison between the various quality checks such as DCA and number of fit points inside the TPC between the real and the embedded tracks for various p_T bins. One can see a close agreement between the real data and the data obtained from embedding. This essentially ensures that the event characteristics do not change drastically on embedding the simulated tracks into the real event.

At low p_T, due to multiple scattering, there is energy loss of tracks for kaon

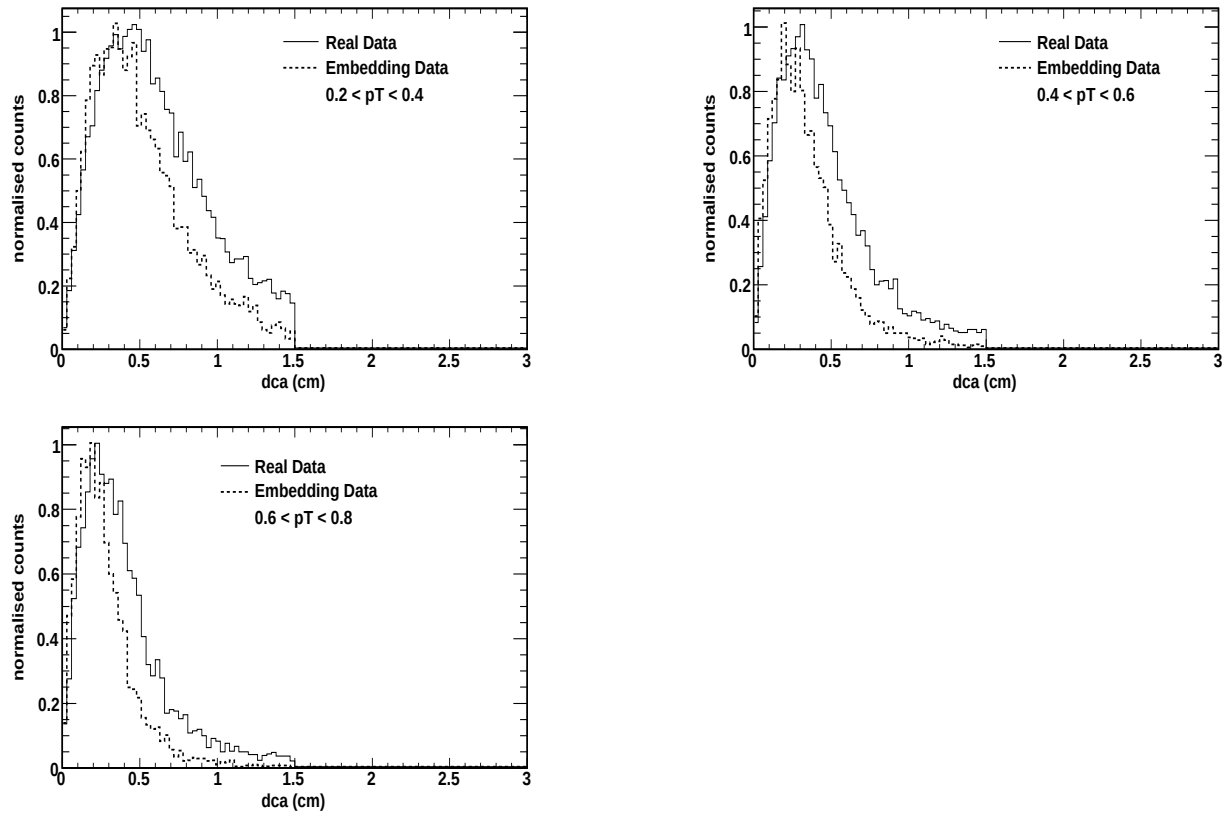

Figure 3.10: The DCA distribution of pions for both the embedded and the real data for various p_T bins. The dataset corresponds to $Cu+Cu$ collisions at 200 GeV.

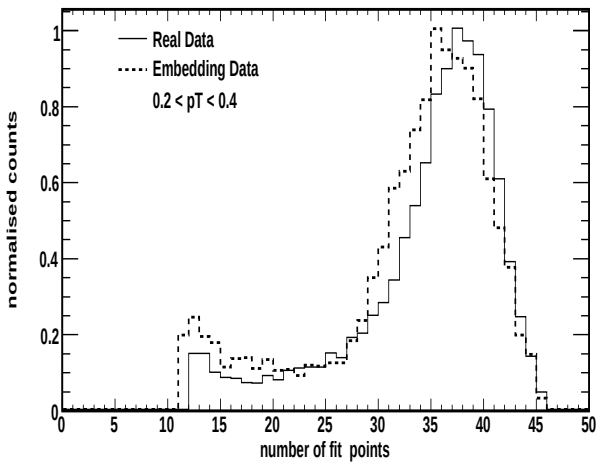

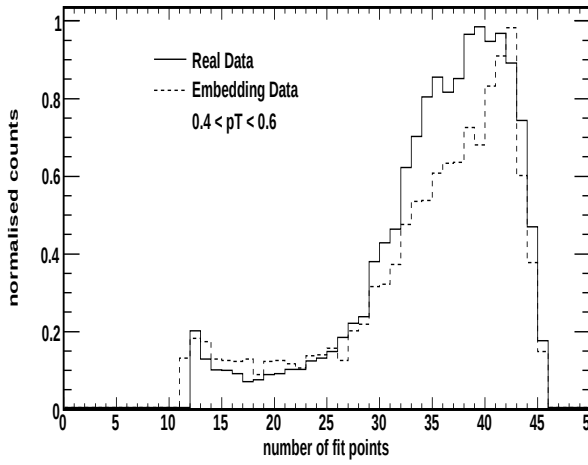

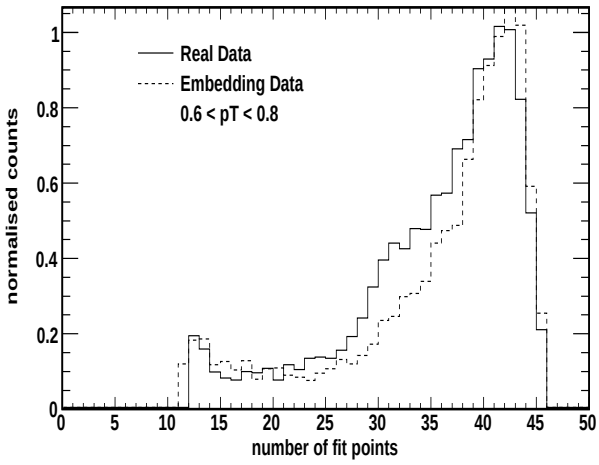

Figure 3.11: The number of fit points distribution of pions for both the embedded and the real data for various p_T bins. The dataset corresponds to Cu+Cu collisions at 200 GeV.

inside the detector. This is not fully corrected during track reconstruction. This may affect the reconstruction efficiency at lower p_T bins. To get an idea about the correction factor required for energy loss of tracks, one needs to calculate the difference $\Delta P_T = p_T^{MC} - P_T^{REC}$ when MC and REC represent the MC simulated and associated reconstructed tracks. Figure 3.12 shows a plot of this as a function of p_T^{rec}. In fact, to get a smooth correction value for every reconstructed p_T, a smooth exponential fit (as shown in the figure) has been used. This energy loss is expected to cause a drop in reconstructed K^{*0} mass in the low p_T region.

Figure 3.13 shows the variation in δp_T for K^{*0} after applying the energy loss correction as indicated above. From the figure one can see that the final p_T of K^{*0} is reconstructed correctly with almost zero difference from p_T used in MC. The energy loss correction which is required for only of low p_T tracks in the detector has been taken into account for determining the correct mass peak positions and the width in the invariant mass distribution. However, no significant difference was observed in the K^{*0} mass as obtained before and after the application of the energy loss correction. This is shown in Figure 3.14.

The reconstruction efficiency for a given p_T-bin can be determined as follows. First we obtain the total number of simulated K^{*0} meson in the above mentioned p_T-bin. Then we obtain the associated decay daughter information in the reconstructed event and subject them to the same dynamical cuts to get the number of reconstructed K^{*0} mesons in that that perticular bin. The ratio is the reconstruction efficiency. The reconstruction efficiency as derived above has been studied as a function of collision centrality for various p_T bins. The results are depicted in Figure 3.15 and 3.16.

3.2.3 Correction for Branching Ratio

The raw yields for K^{*0} and $K^{*\pm}$ also need to be corrected for the corresponding branching ratios. The decay modes of K^{*0} ($\sim$100%) as known from [76] are the

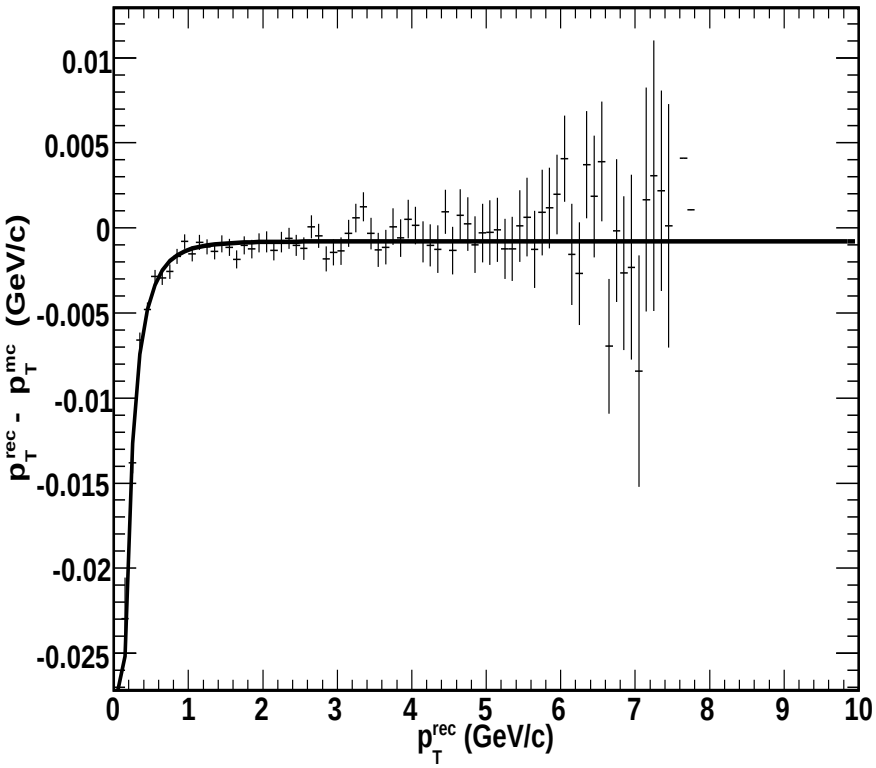

Figure 3.12: The energy loss plot for kaons. The solid line is the exponential fit on the obtained data points. The dataset corresponds to *Cu+Cu* collisions at 200 GeV.

following: (i) into two oppositely charged daughters ($K^{*0} \rightarrow K^{+}\pi^{-}$ or $K^{*0} \rightarrow K^{-}\pi^{+}$) and (ii) into two neutral daughters ($K^{*0} \rightarrow K^{0}\pi^{0}$). Two thirds of the K^{*0} mesons decay into oppositely charged daughters while one third of the K^{*0} decay into the channel with neutral daughters. This is understood from isospin considerations. In TPC, we detect the K^{*0} which decay into two oppositely charged daughters. Hence, the raw K^{*0} yields needs to be corrected using the branching ratio of 2/3 (0.66). Similarly, $K^{*\pm}$ mesons decay $\sim$100% via the following two decay channels: (i) into a neutral kaon and a charged pion ($K^{*\pm} \rightarrow K^{0}\pi^{\pm}$) and (ii) into a charged kaon and a neutral pion ($K^{*\pm} \rightarrow K^{\pm}\pi^{0}$). Again from isospin considerations, we know that two-thirds of the $K^{*\pm}$ mesons would decay producing a neutral kaon, while one-third

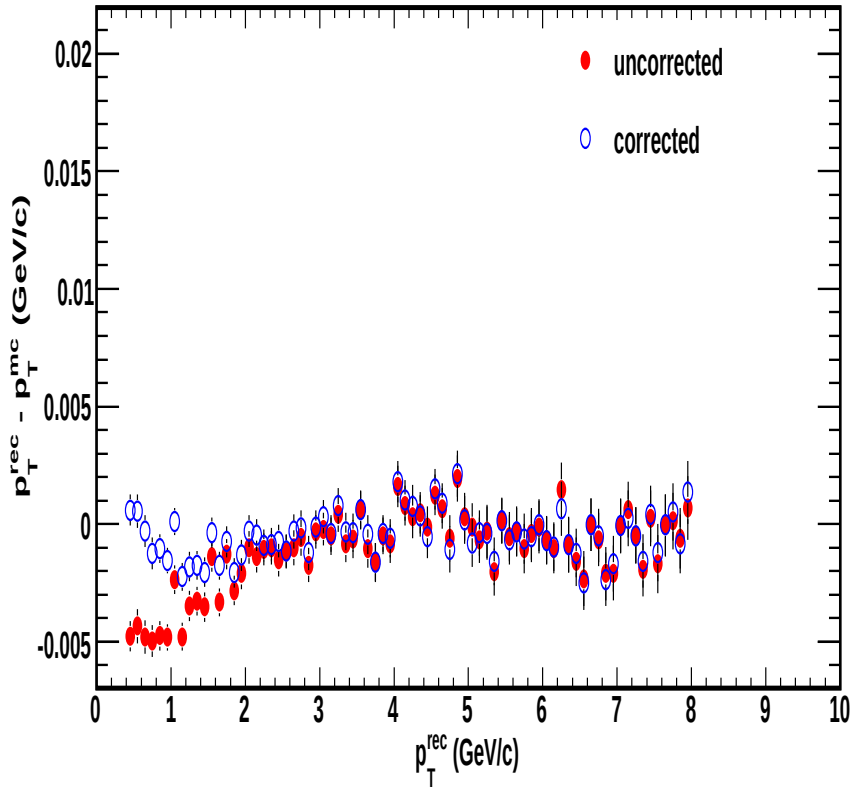

Figure 3.13: The energy loss correction plot for K^{*0}. The dataset corresponds to Cu+Cu collisions at 200 GeV.

of them decay into a neutral pion. We select the first channel where K^0 decays into K^0_S which again decays into pions via $K^0_S \rightarrow \pi^+\pi^-$. Also we have to consider that only half of the K^0 mesons decay as K^0_S the other half decaying as K^0_L which we don't detect. The branching ratio for $K^0_S \rightarrow \pi^+\pi^-$ is 68.61% [76]. Therefore the total decay branching ratio for $K^{*\pm}$ is equal to 2/3×1/2× 0.6861 which is 0.2287. The total K^* yield is the corrected using the above factor. It was found that the event vertex finding efficiency, which is fraction of events having reconstructed vertices, drops rapidly for low multiplicity events. Thus, a vertex efficiency correction is applied. The efficiency factor is 94.5% for Au+Au collisions at 62.4 GeV and 92.2% for Cu+Cu collisions at 62.4 GeV and 200 GeV.

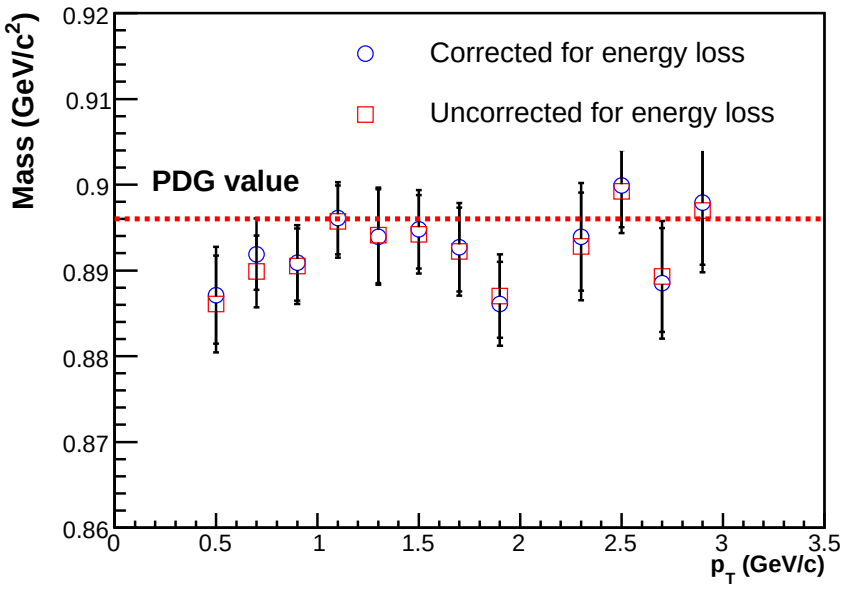

Figure 3.14: The K^{*0} mass as a function of p_T before and after applying energy loss corrections for Cu+Cu collisions at 200 GeV.

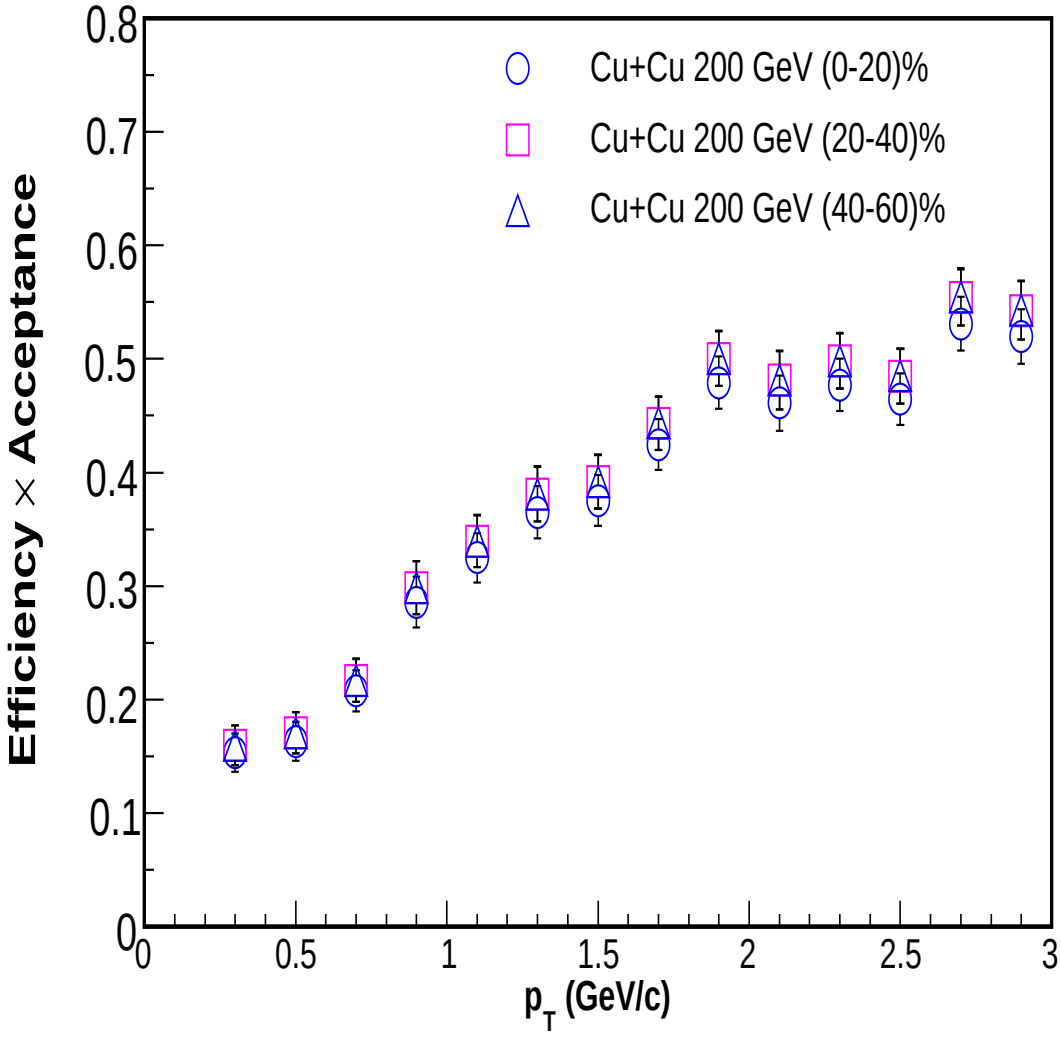

Figure 3.15: The total reconstruction efficiency as a function of p_T for K^{*0} for different centralities of Cu+Cu collisions at 200 GeV.

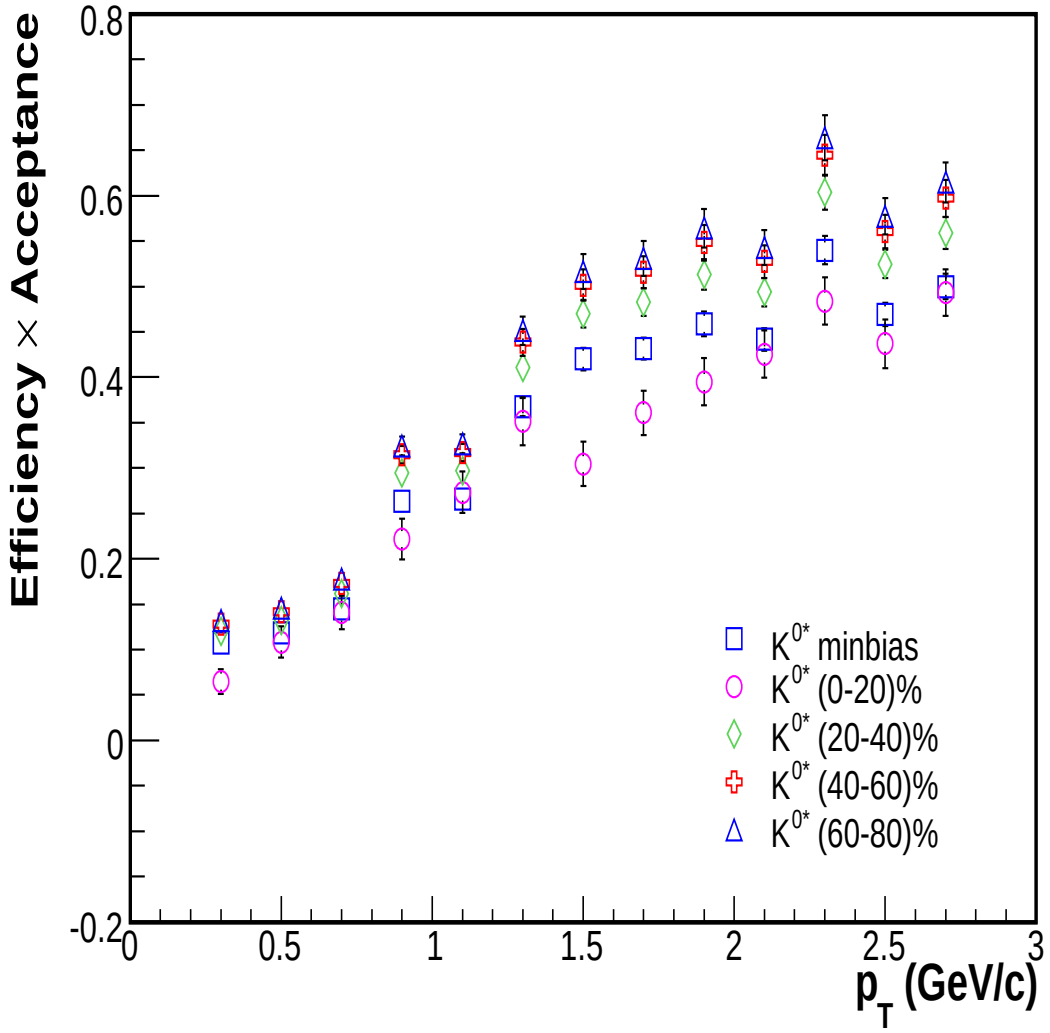

Figure 3.16: The total reconstruction efficiency as a function of p_T for K^{*0} for different centralities of Au+Au collisions at 62.4 GeV.

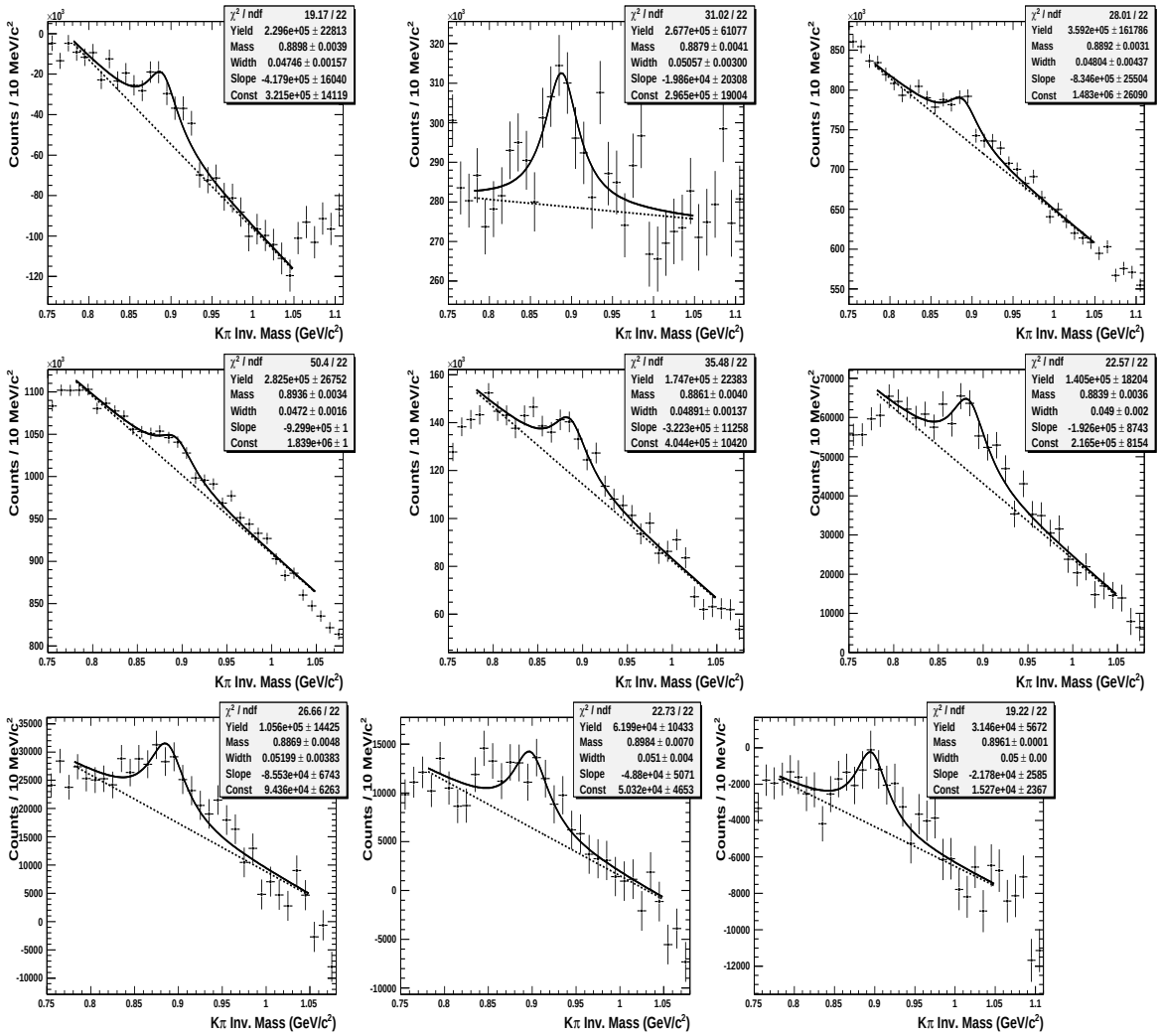

Figure 3.17: The $K\pi$ invariant mass distributions in Au+Au collisions at 62.4 GeV for different p_T bins, each having bin width 0.2 GeV/c for (0-20)% centrality. The solid curve stands for the fit function using eqn. 3.4 and the dashed lines stands for the linear residual background.

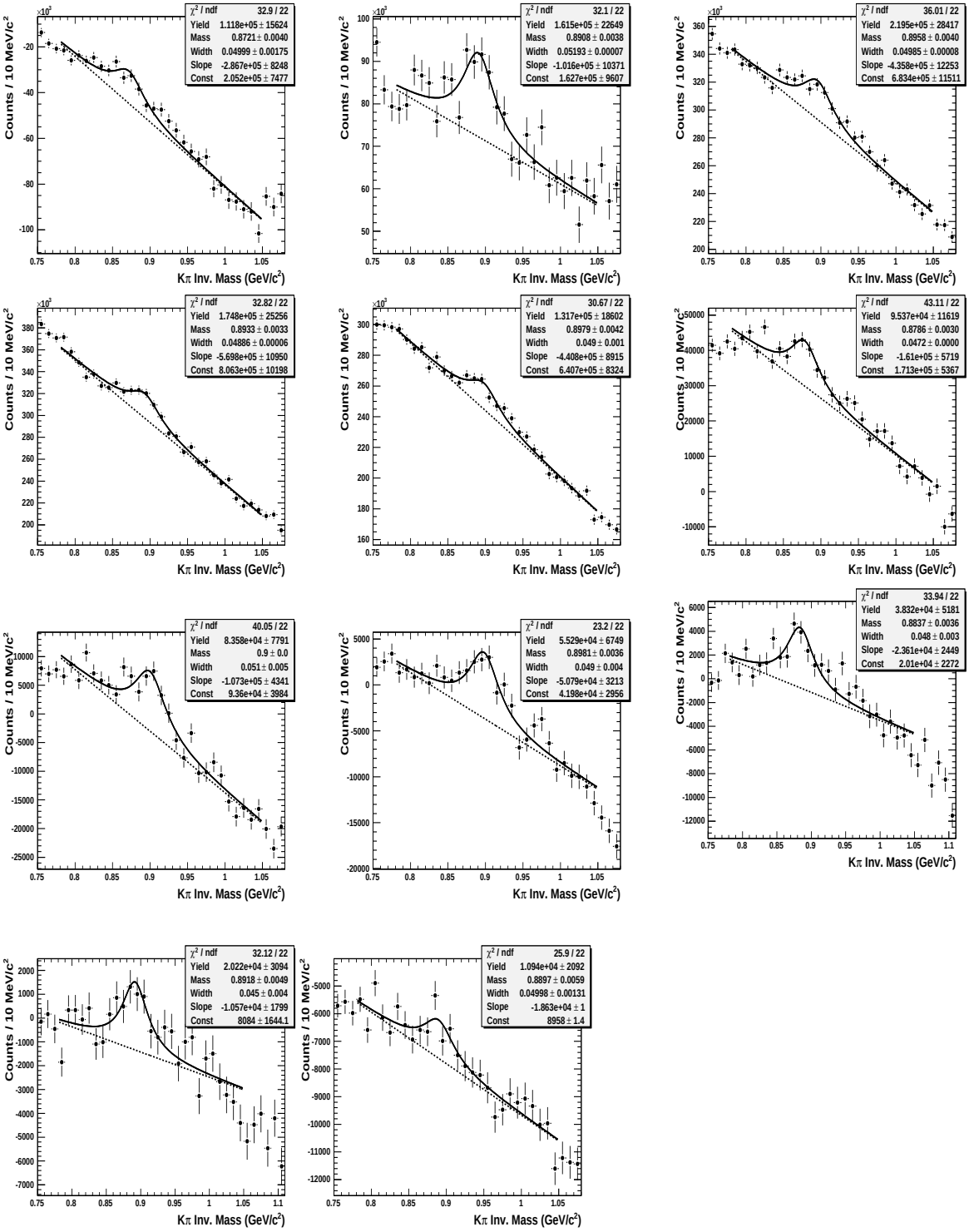

Figure 3.18: The $K\pi$ invariant mass distributions in Au+Au collisions at 62.4 GeV for different p_T bins, each having bin width 0.2 GeV/c for (20-40)% centrality. The solid curves stand for the fit function using eqn. 3.4 and the dashed lines stand for the linear residual background.

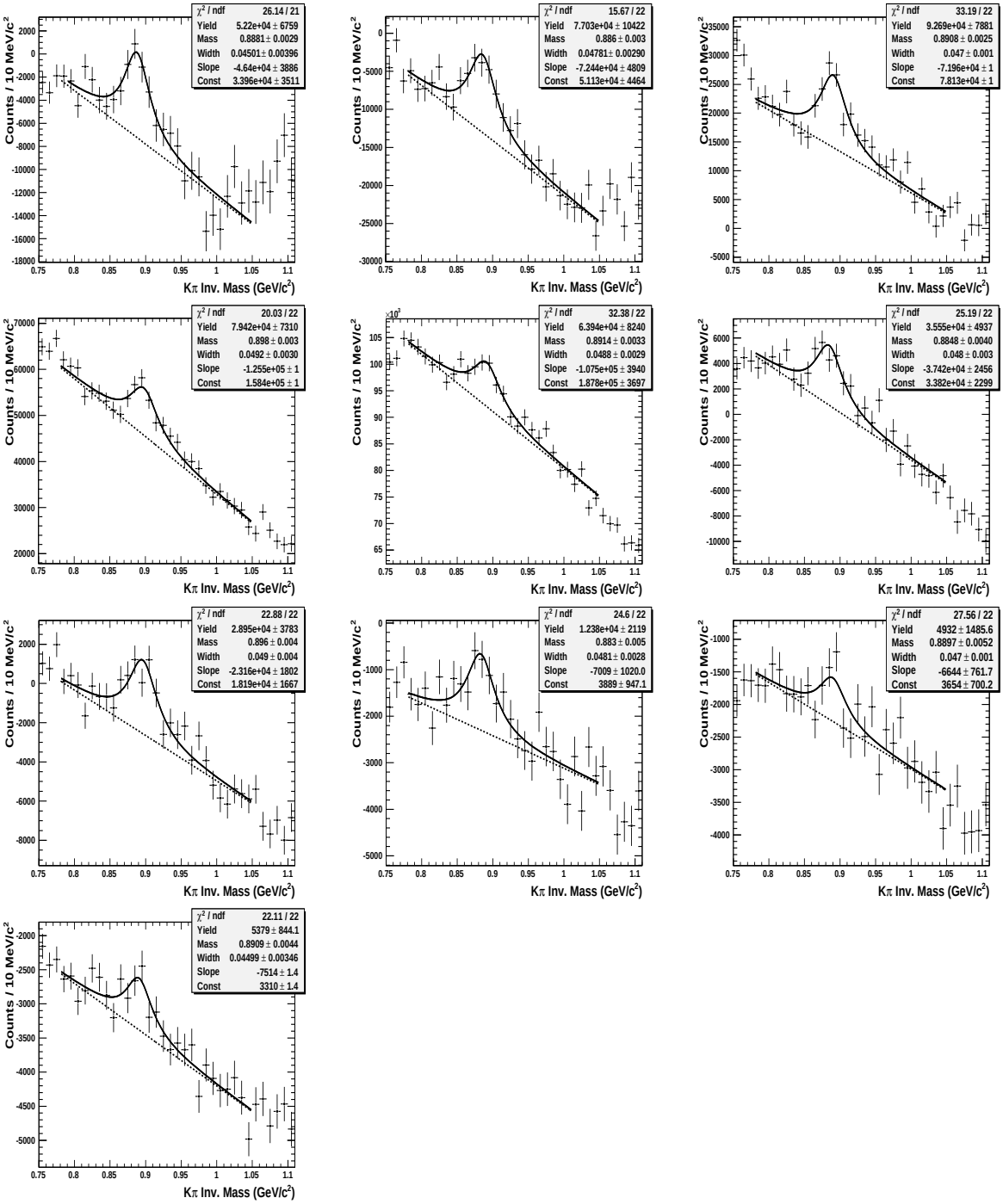

Figure 3.19: The $K\pi$ invariant mass distributions in Au+Au collisions at 62.4 GeV for different p_T bins, each having bin width 0.2 GeV/c for (40-60)% centrality. The solid curves stand for the fit function using eqn. 3.4 and the dashed lines stand for the linear residual background.

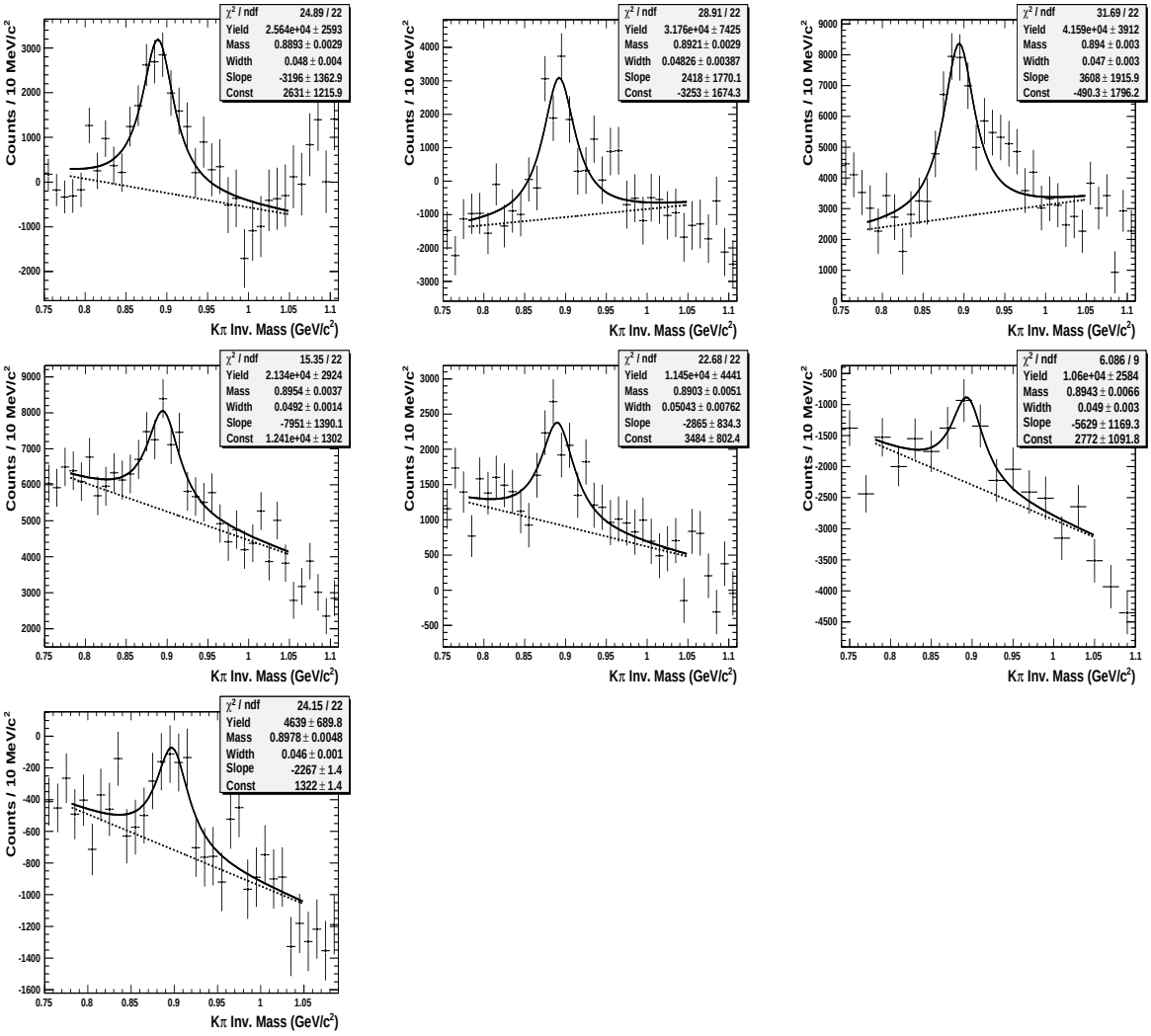

Figure 3.20: The $K\pi$ invariant mass distributions in Au+Au collisions at 62.4 GeV for different p_T bins, each having bin width 0.2 GeV/c for (60-80)% centrality. The solid curves stand for the fit function using eqn. 3.4 and the dashed lines stand for the linear residual background.

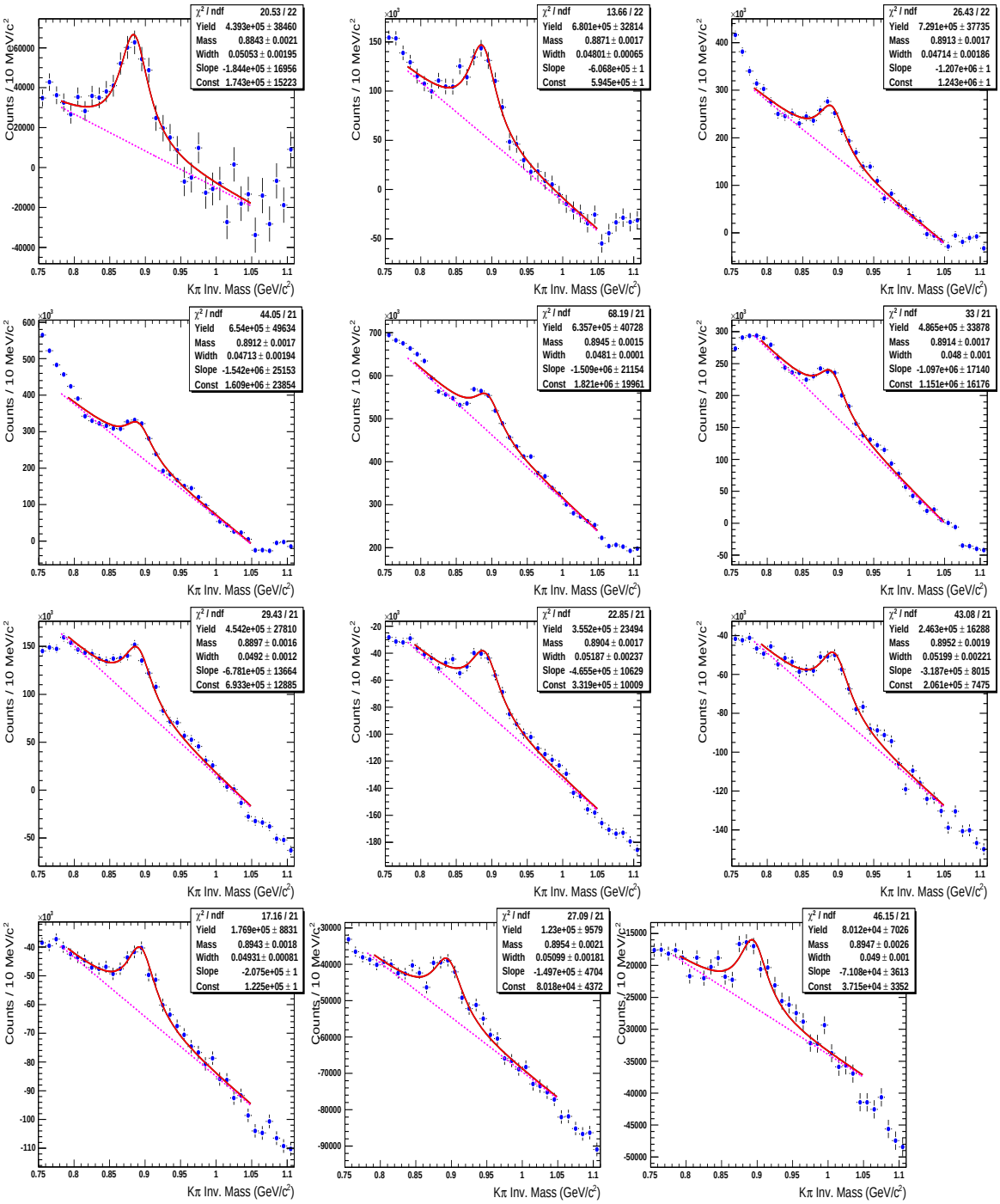

Figure 3.21: The $K\pi$ invariant mass distributions in Cu+Cu at 200 GeV for different p_T bins, each having bin width 0.2 GeV/c for (0-20)% centrality. The solid curve stands for the fit function using eqn. 3.4 and the dashed lines stands for the linear residual background.

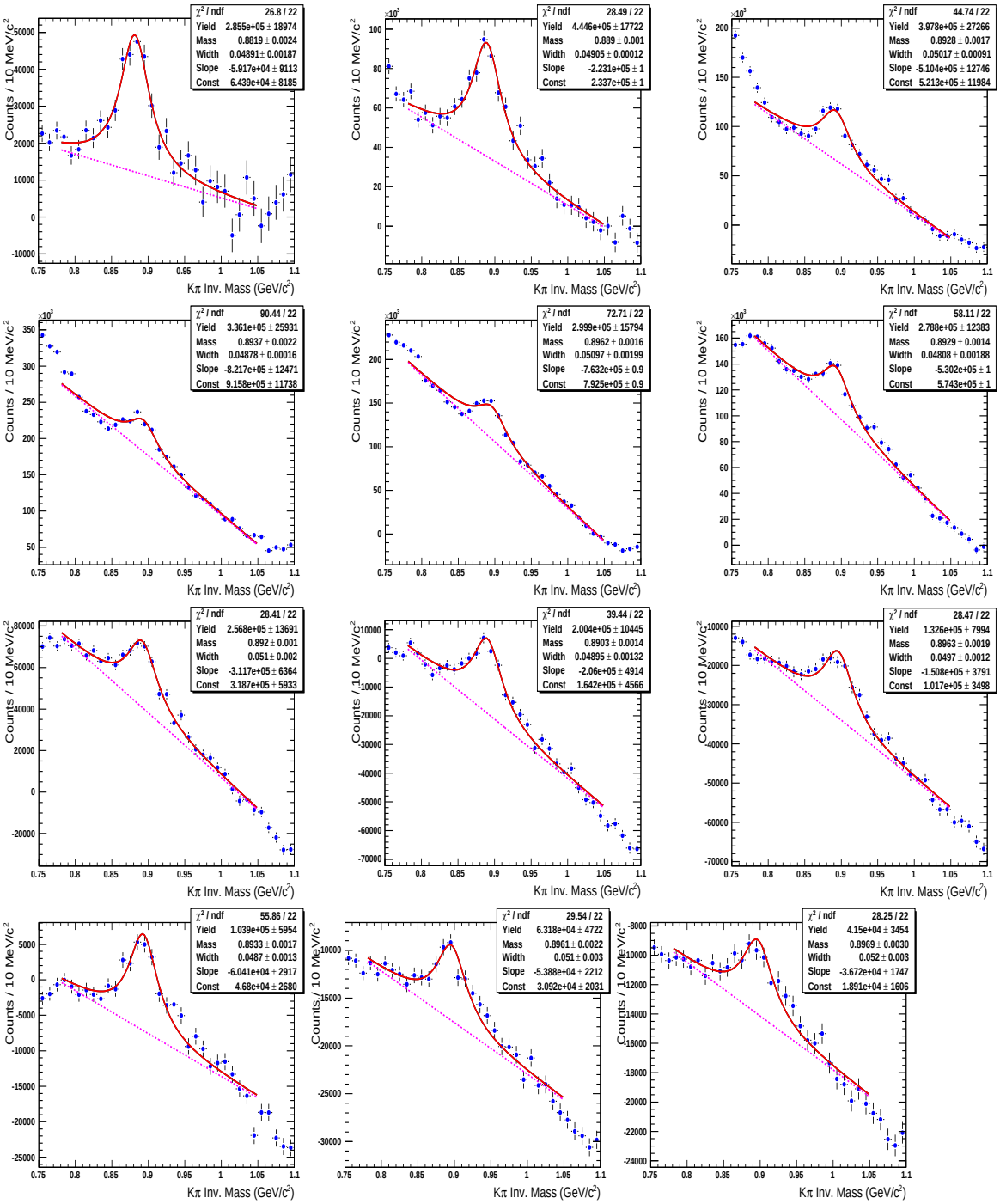

Figure 3.22: The $K\pi$ invariant mass distributions in *Cu+Cu* at 200 GeV for different p_T bins, each having bin width 0.2 GeV/c for (20-40)% centrality. The solid curve stands for the fit function using eqn. 3.4 and the dashed lines stands for the linear residual background.

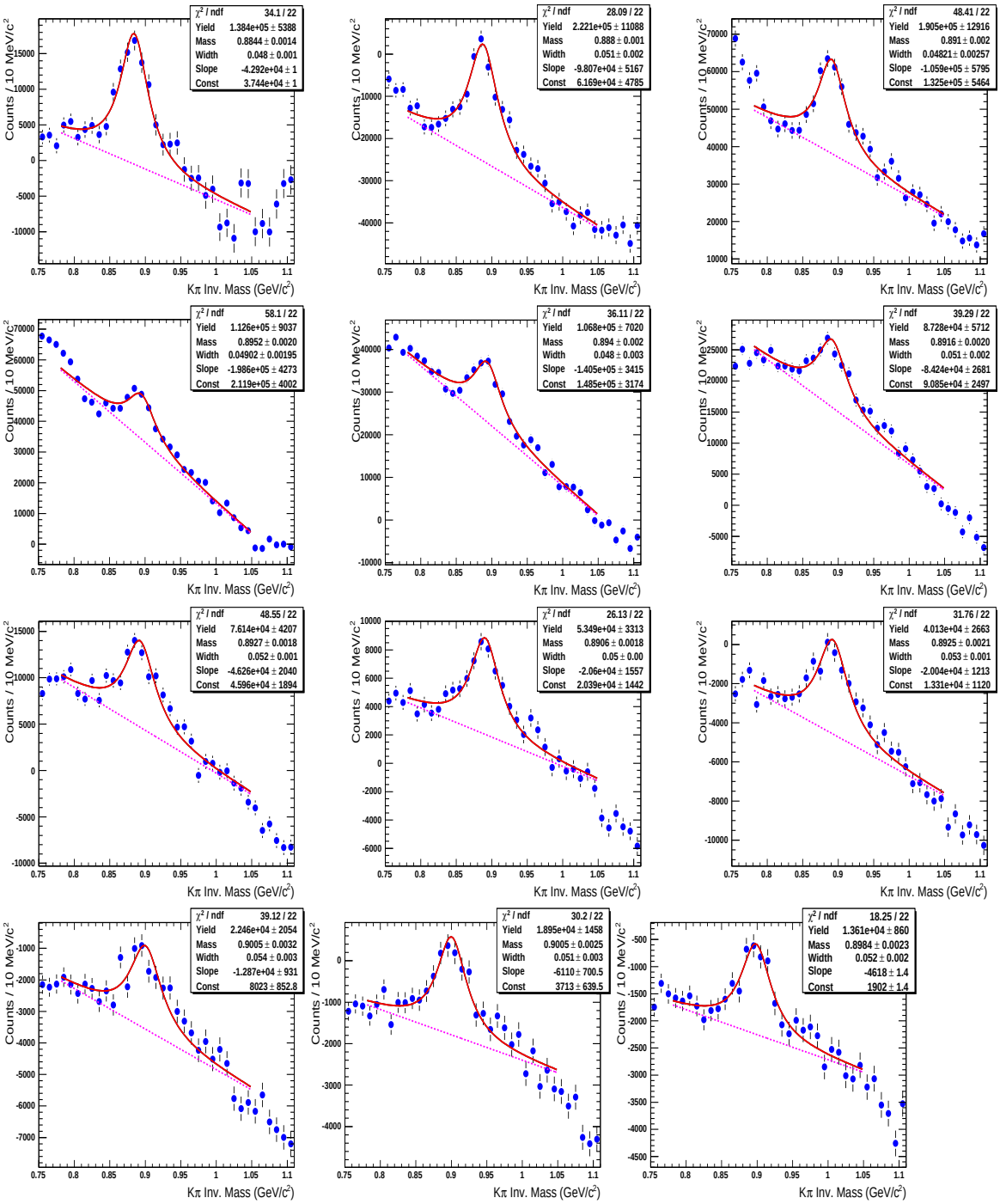

Figure 3.23: The $K\pi$ invariant mass distributions in *Cu+Cu* at 200 GeV for different p_T bins, each having bin width 0.2 GeV/c for (40-60)% centrality. The solid curve stands for the fit function using eqn. 3.4 and the dashed lines stands for the linear residual background.

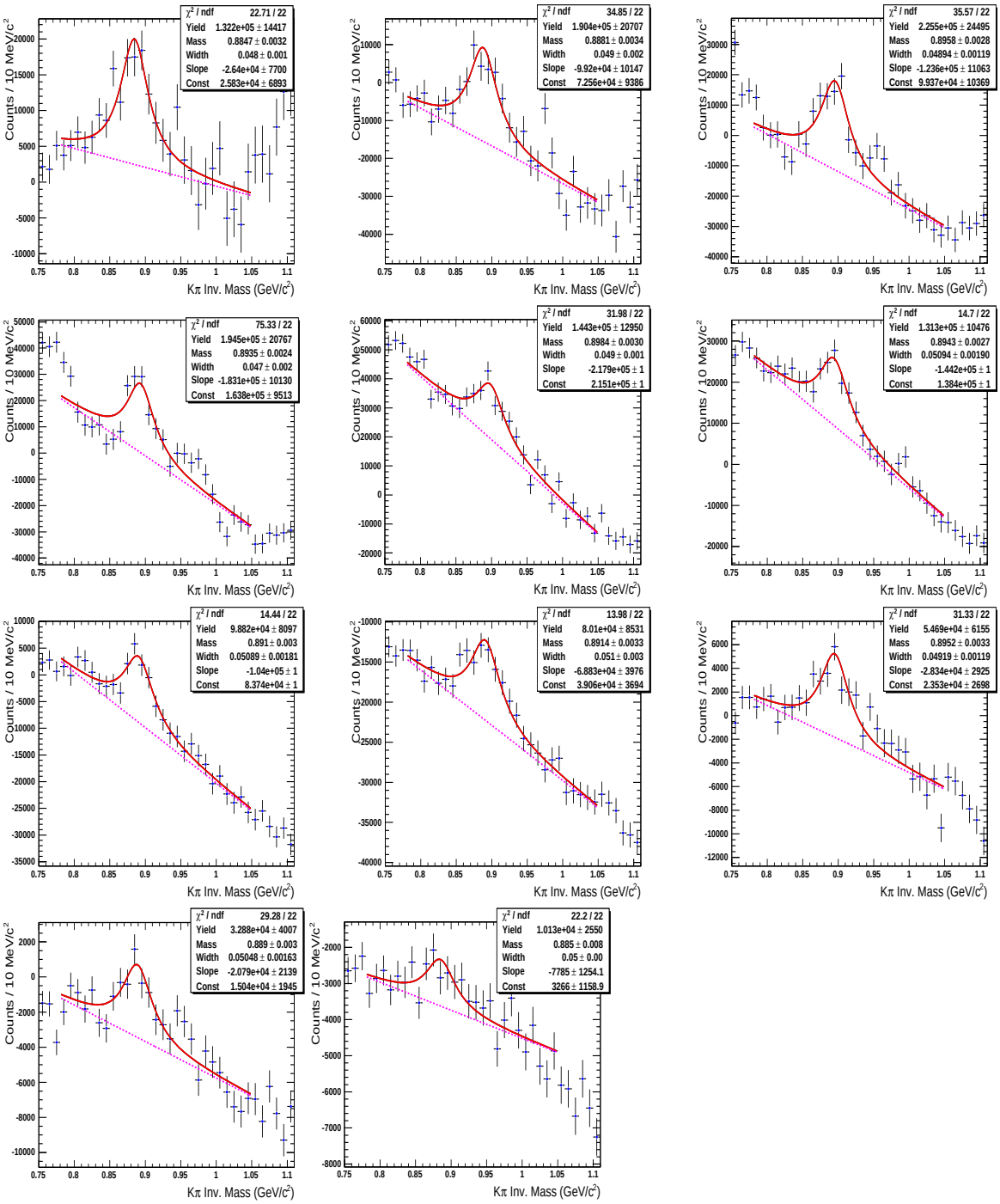

Figure 3.24: The $K\pi$ invariant mass distributions in *Cu+Cu* at 62 GeV for different p_T bins, each having bin width 0.2 GeV/c for (0-20)% centrality. The solid curve stands for the fit function using eqn. 3.4 and the dashed lines stands for the linear residual background.

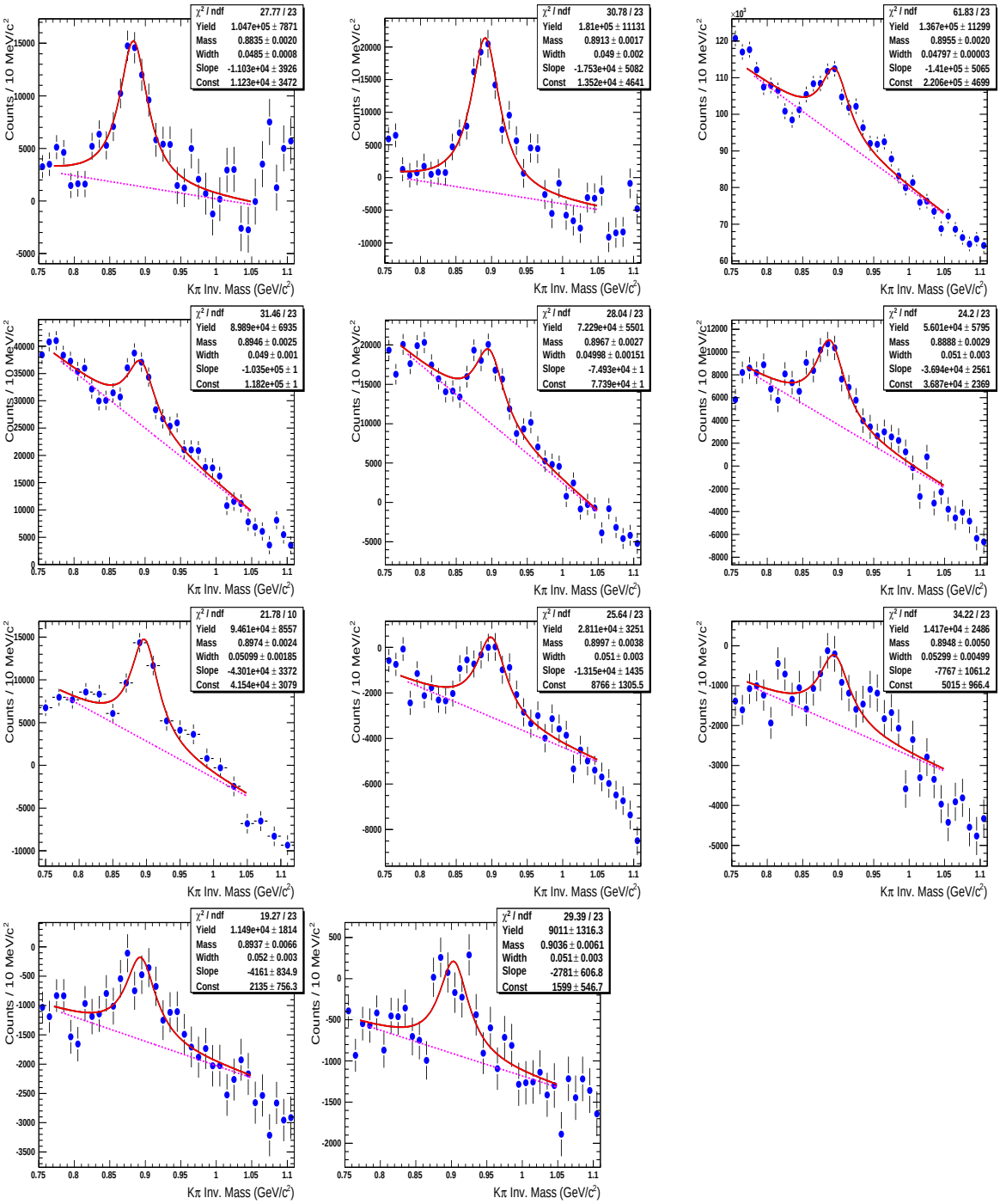

Figure 3.25: The $K\pi$ invariant mass distributions in Cu+Cu at 62.4 GeV for different p_T bins, each having bin width 0.2 GeV/c for (20-40)% centrality. The solid curve stands for the fit function using eqn. 3.4 and the dashed lines stands for the linear residual background.

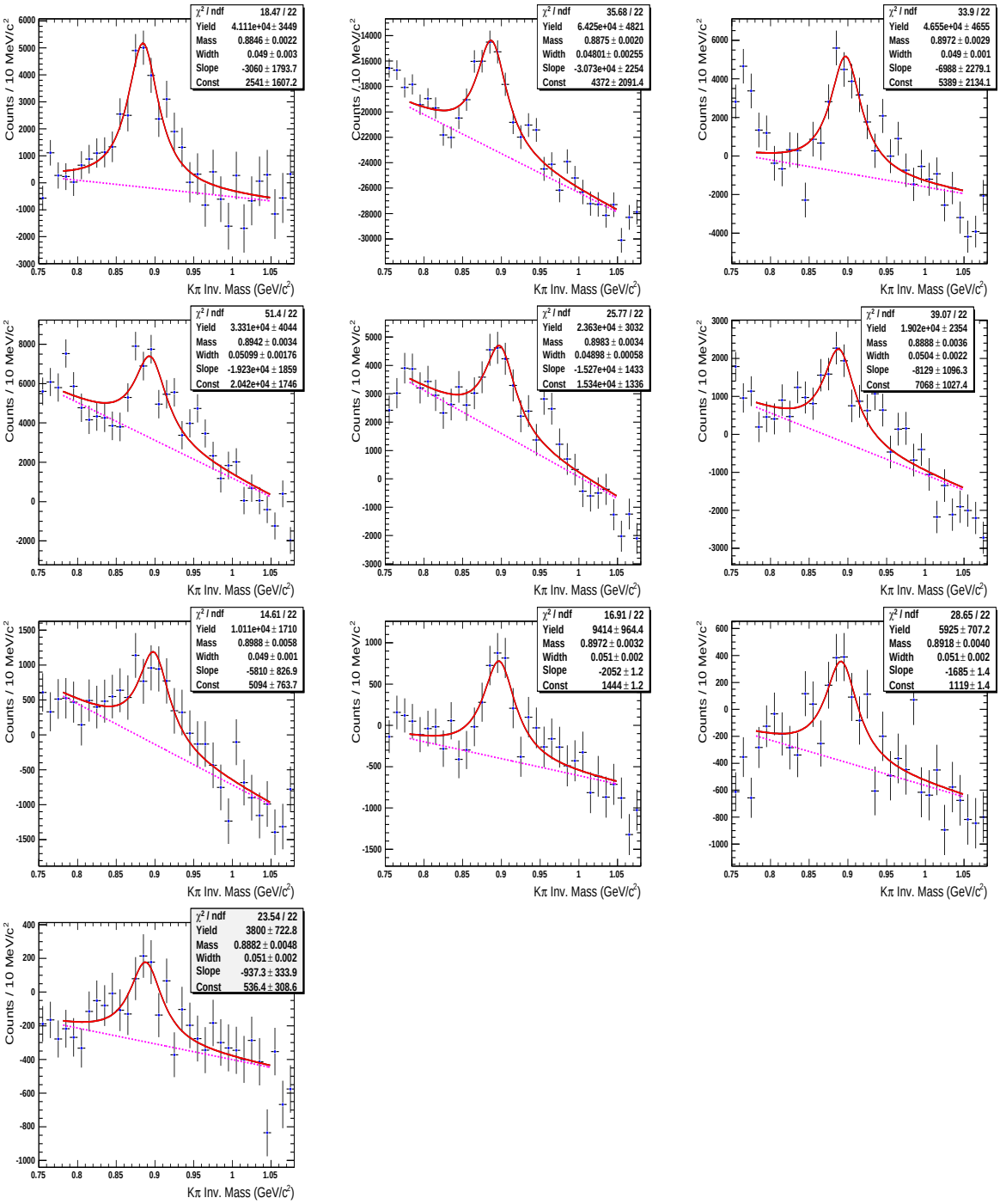

Figure 3.26: The $K\pi$ invariant mass distributions in Cu+Cu at 62.4 GeV for different p_T bins, each having bin width 0.2 GeV/c for (40-60)% centrality. The solid curve stands for the fit function using eqn. 3.4 and the dashed lines stands for the linear residual background.

Chapter 4

Experimental Findings

In this chapter we first present results on K^{*0} mass and its width, for minimum-bias events, as a function of transverse momentum, p_T. This has been done in case of *Cu+Cu* collisions at 62.4 GeV as well as 200 GeV and *Au+Au* collisions at 62.4 GeV, to look at medium induced modification effects on the above two parameters. The p_T distributions of K^{*0} yields for different systems have also been studied. This is expected to provide valuable information on particle production mechanism. Next we look at the nuclear modification factor R_{CP} which is defined as the ratio of central-to-peripheral yields, scaled to the number of binary collisions. We have studied the K^{*0}/K^{-} and ϕ/K^{*0} ratios to look at effects of regeneration against re-scattering and possible strangeness enhancement effects. In the following section results are shown along with systematic errors whose sources are presented in the later half of the discussion.

4.1 K^{*0} Mass and Width Distributions

The variation of K^{*0} invariant mass peak positions with respect to p_T for minimum bias *Au+Au* and *Cu+Cu* collisions in 62.4 GeV and 200 GeV is shown in Figure 4.1

p_T (GeV/c)	Au+Au (62.4 GeV)	Cu+Cu (62.4 GeV)	Cu+Cu (200 GeV)
0.4 - 0.6	(884.0±3.0±5.8)	(883.8±1.4±6.1)	(886.1±2.4±5.1)
0.6 - 0.8	(887.2±2.7±4.87)	(889.1±1.4±7.7)	(889.9±1.9±3.7)
0.8 - 1.0	(890.9±2.2±5.84)	(895.2±1.5±6.1)	(890.5±2.1±3.8)
1.0 - 1.2	(894.8±2.6±5.4)	(897.3±1.1±4.9)	(895.7±1.9±3.7)
1.2 - 1.4	(895.1±3.2±6.5)	(895.6±1.7±6.4)	(894.1±1.7±5.3)
1.4 - 1.6	(888.6±3.7±8.8)	(895.2±1.6±4.6)	(894.2±2.3±3.9)
1.6 - 1.8	(881.7±3.1±7.0)	(892.5±0.6±3.2)	(892.2±2.5±4.5)
1.8 - 2.0	(887.1±4.1±2.0)	(891.9±2.3±1.9)	(887.0±2.0±4.4)
2.0 - 2.2	(891.2±3.7±8.2)	(896.2±2.5±9.5)	(892.8±2.3±5.8)
2.2 - 2.4	(887.7±4.2±7.3)	(886.5±2.9±6.2)	(892.8±2.3±5.8)
2.4 - 2.6	(893.6±4.0±5.6)	(891.6±4.0±5.9)	(899.2±2.8±3.9)
2.6 - 2.8	(896.1±3.6±4.8)	(895.5±4.0±6.4)	889.3±4.3±4.8)
2.8 - 3.0		(894.1±3.8±3.1)	897.0±3.0±6.5)

Table 4.1: The K^{*0} mass for each p_T bin, for minimum-bias collisions, in different collision systems. Both statistical and systematic errors are listed. The first and the second error components correspond to statistical and systematic errors, respectively.

(Upper Panel). The solid line represents the standard mass value as given in the Particle Data book for K^{*0} (896 MeV/c^2) [76]. The error bars shown correspond to statistical errors while the bands represent systematic uncertainties. Figure 4.1 (Lower panel) depicts the comparison between the K^{*0} mass distribution in *Cu+Cu* collisions at 200 GeV with the results obtained from Monte Carlo (MC) simulations. In the lower p_T region ($<$ 1 GeV) the measured masses, although systematically smaller than the PDG values and MC simulation results, within systematic errors, are in reasonable agreement with PDG values. Table 4.1 lists the K^{*0} invariant mass for different p_T bins, for minimum-bias collisions involving different systems as taken in the present case.

Figure 4.2 (Upper Panel) shows the variation of K^{*0} width with p_T for minimum-bias *Au+Au* and *Cu+Cu* collisions in 62.4 GeV and 200 GeV. The solid line represents the standard K^{*0} width of 50 MeV/c^2 [76]. In the figure, we do not see any significant difference between the measured widths and the PDG value for the three different

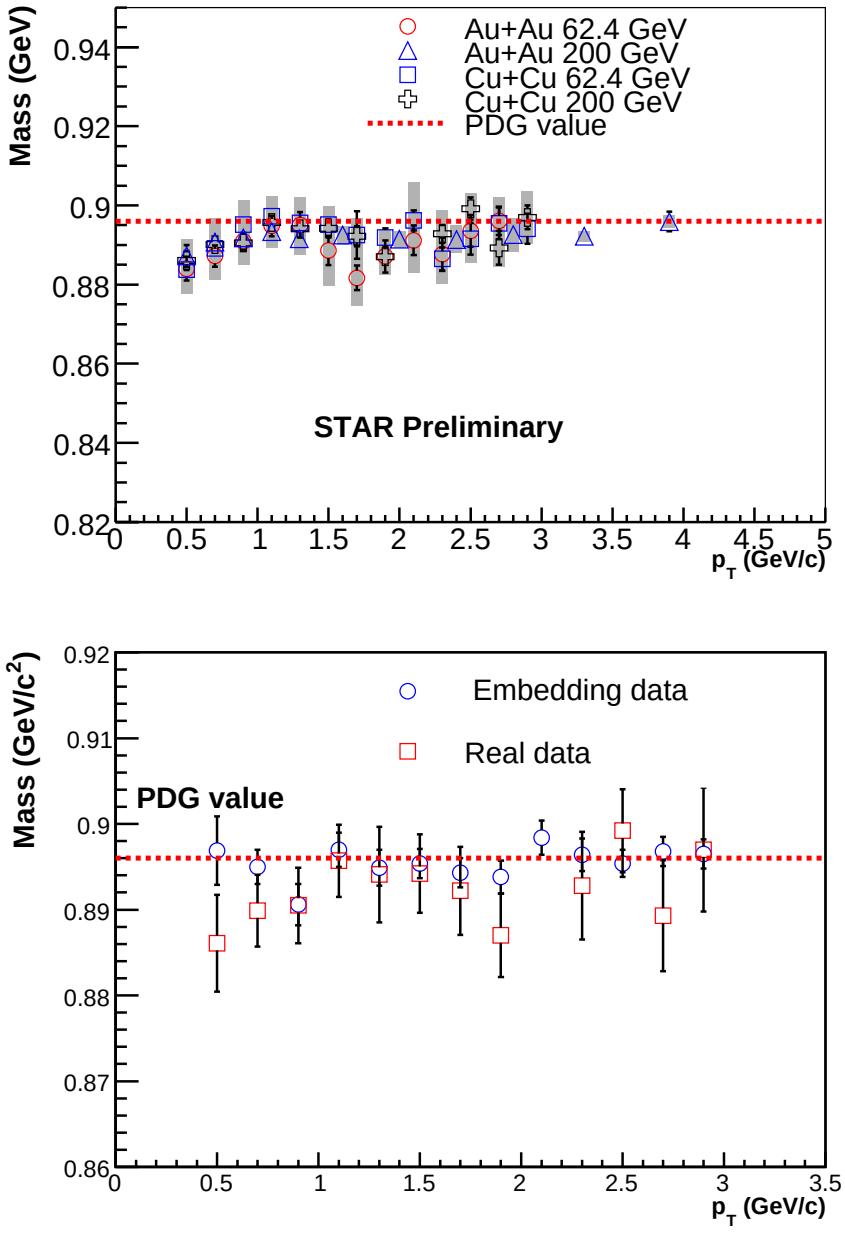

Figure 4.1: **Upper Panel** The K^{*0} mass as a function of p_T for different collision systems. The dashed line represent the K^{*0} mass value from Particle Data Book [76]. The shaded region shows the systematic uncertainties on the obtained values. **Lower Panel** The K^{*0} mass from real data and the K^{*0} mass obtained from the Monte Carlo (MC) simulation as a function of p_T for Cu+Cu collisions at 200 GeV.

p_T (GeV/c)	Au+Au (62.4 GeV)	Cu+Cu (62.4 GeV)	Cu+Cu (200 GeV)
0.4 - 0.6	(884.0±3.0±5.8)	(883.8±1.4±6.1)	(886.1±2.4±5.1)
0.6 - 0.8	(887.2±2.7±4.87)	(889.1±1.4±7.7)	(889.9±1.9±3.7)
0.8 - 1.0	(890.9±2.2±5.84)	(895.2±1.5±6.1)	(890.5±2.1±3.8)
1.0 - 1.2	(894.8±2.6±5.4)	(897.3±1.1±4.9)	(895.7±1.9±3.7)
1.2 - 1.4	(895.1±3.2±6.5)	(895.6±1.7±6.4)	(894.1±1.7±5.3)
1.4 - 1.6	(888.6±3.7±8.8)	(895.2±1.6±4.6)	(894.2±2.3±3.9)
1.6 - 1.8	(881.7±3.1±7.0)	(892.5±0.6±3.2)	(892.2±2.5±4.5)
1.8 - 2.0	(887.1±4.1±2.0)	(891.9±2.3±1.9)	(887.0±2.0±4.4)
2.0 - 2.2	(891.2±3.7±8.2)	(896.2±2.5±9.5)	(892.8±2.3±5.8)
2.2 - 2.4	(887.7±4.2±7.3)	(886.5±2.9±6.2)	(892.8±2.3±5.8)
2.4 - 2.6	(893.6±4.0±5.6)	(891.6±4.0±5.9)	(899.2±2.8±3.9)
2.6 - 2.8	(896.1±3.6±4.8)	(895.5±4.0±6.4)	889.3±4.3±4.8)
2.8 - 3.0		(894.1±3.8±3.1)	897.0±3.0±6.5)

Table 4.2: The K^{*0} width for each p_T bin for minimum-bias collisions in different collision systems. Both the statistical and systematic errors are listed. The first and the second error components correspond to statistical and systematic errors, respectively.

collision systems studied. The lower panel of the Figure 4.2 shows a comparison of the measured K^{*0} width with MC simulations in *Cu+Cu* collisions at 200 GeV. We observe that the widths determined from MC simulations agree reasonably well with the real data. Table 4.2 lists the K^{*0} width values for various p_T bins in different collision systems. The systematic uncertainties in the K^{*0} mass and width were calculated bin by bin as a function of p_T by using different residual background function, different fitting function to the K^{*0} invariant mass spectrum, varying the particle types and the dynamical cuts on tracks. The sources of systematic errors are presented later.

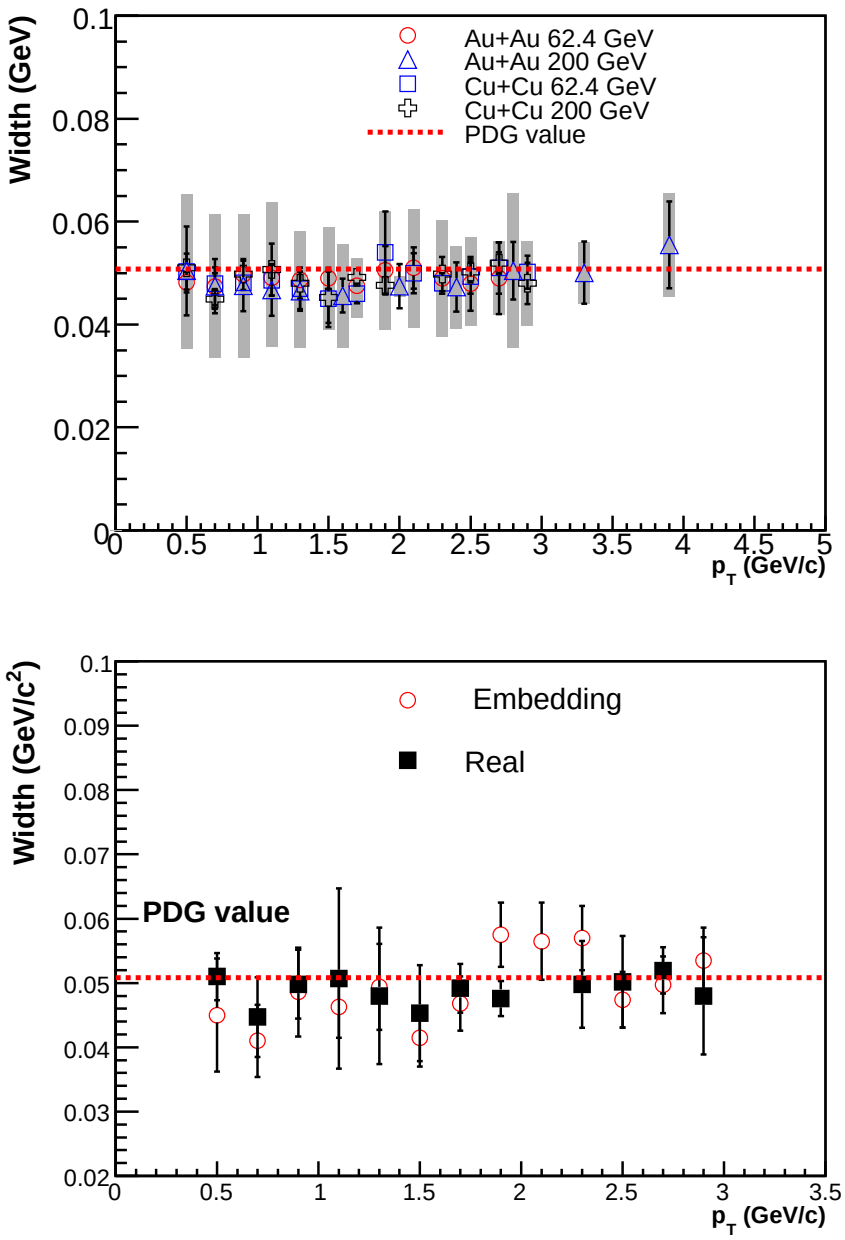

Figure 4.2: **Upper Panel** The K^{*0} width as a function of p_T for different collision systems. The dashed line represents the K^{*0} width as obtained from the Particle Data Book [76]. The shaded region shows the systematic uncertainties on the obtained values. **Lower Panel** The K^{*0} width from real data and the same obtained from the MC simulation as a function of p_T for Cu+Cu collisions at 200 GeV.

p_T (GeV/c)	(0-20)%	(20-40)%	(40-60)%	(60-80)%
0.4 - 0.6	1.5348±0.301019	0.57±0.13	0.27±0.055	0.13±0.03
0.6 - 0.8	0.73158±0.237592	0.38±0.094	0.18±0.039	0.073±0.018
0.8 - 1.0	0.57483±0.0978938	0.35±0.074	0.148±0.022	0.065±0.018
1.0 - 1.2	0.366661±0.118472	0.148±0.039	0.067±0.014	0.028±0.009
1.2 - 1.4	0.219792±0.0308119	0.081±0.015	0.039±0.006	0.013±0.004
1.4 - 1.6	0.1487082±0.0385214	0.065±0.018	0.026±0.004	0.008±0.002
1.6 - 1.8	0.0762579±0.0204201	0.038±0.010	0.014±0.003	0.005±0.0013
1.8 - 2.0	0.0636098±0.0121927	0.028±0.004	0.0097±0.0016	0.002±0.0004
2.0 - 2.2	0.0413884±0.00744718	0.016±0.003	0.004±0.0010	0.0013±0.0003
2.2 - 2.4	0.0192156±0.00445683	0.010±0.002	0.003±0.0008	
2.4 - 2.6	0.0122577±0.0033473	0.005±0.001	0.0012±0.0004	
2.6 - 2.8	0.00823321±0.00202523	0.002±0.0009	0.0011±0.0002	

Table 4.3: The average of K^{*0} and $\overline{K^{*0}}$ invariant yields, $d^2N/(2\pi p_T dp_T dy)$, in each p_T bin for different collision centralities in Au+Au collisions at 62.4 GeV.

4.2 Transverse Momentum Spectra

The transverse momentum, p_T, distributions of K^{*0} meson from Au+Au collisions at 62.4 GeV and Cu+Cu collisions at 62.4 GeV and 200 GeV are presented in Figure 4.3, 4.4 and 4.5 respectively. The spectra are corrected for detector efficiency and acceptance for various collision centralities. The error bars depicted are the quadratic sums of both statistical and systematic errors. The dashed lines shows an exponential fit to the data points, as given by

$$\frac{1}{2\pi p_T}\frac{d^2N}{dp_T dy} = \frac{dN/dy}{2\pi T(m_0+T)} exp[-(m_T - m_{K^{*0}})/T] \tag{4.1}$$

The fitting function has two open parameters, *viz* T and dN/dy. T is known as the inverse slope parameter and dN/dy is the K^{*0} yield per unit rapidity. As can be seen in the figures, the spectra, for both the collision systems at a given energy, are very similar. Table 4.3, 4.4 and 4.5 list the $(K^{*0} + \overline{K^{*0}})/2$ invariant yields, $d^2N/(2\pi p_T dp_T dy)$, at mid-rapidity in each p_T bin for different collision systems.

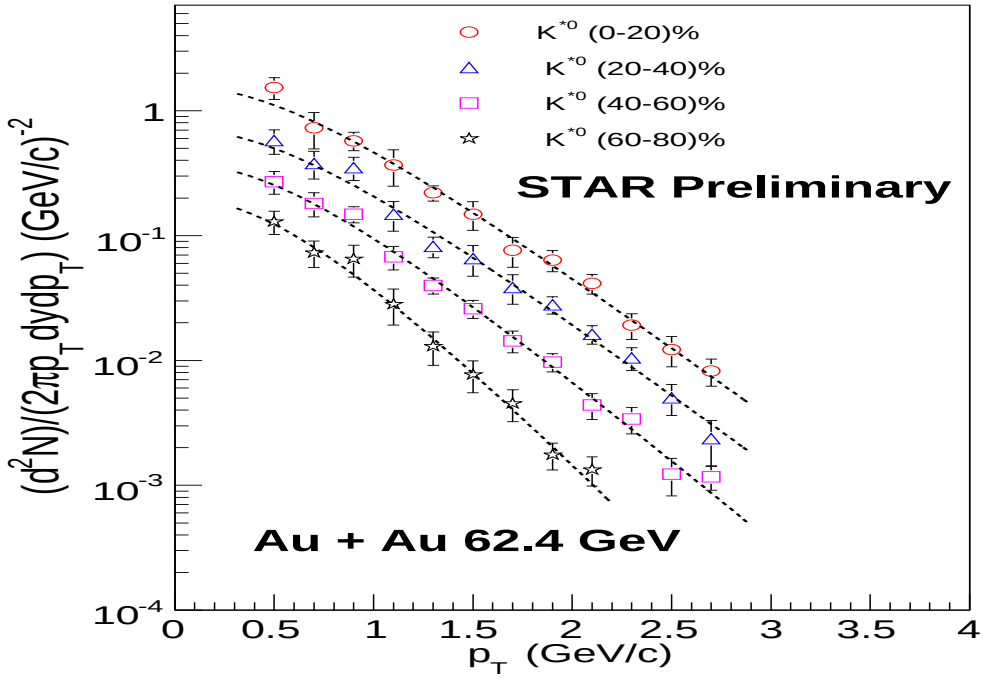

Figure 4.3: K^{*0} meson transverse momentum spectra for different centralities in Au+Au collisions at 62.4 GeV. The error bars shown are quadratic sums of the statistical and systematic errors. The dashed line represents an exponential function fit to the data points as given by Eqn.(4.1).

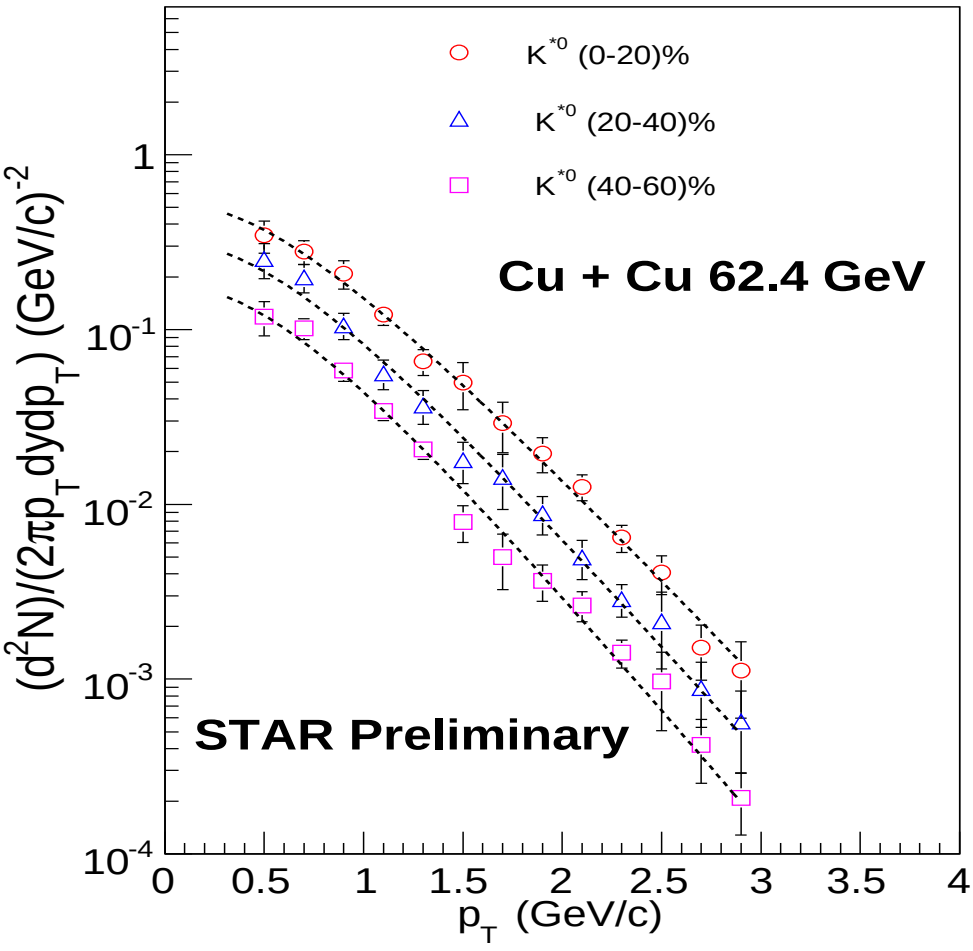

Figure 4.4: K^{*0} meson transverse momentum spectra for different centralities in Cu+Cu collisions at 62.4 GeV. The error bars shown are quadratic sum of the statistical and systematic errors. The dashed line represents an exponential fit (Eqn. 4.1) to the data points.

p_T (GeV/c)	(0-20)%	(20-40)%	(40-60)%
0.4 - 0.6	0.345±0.07	0.57±0.13	0.27±0.055
0.6 - 0.8	0.279±0.044	0.38±0.094	0.18±0.039
0.8 - 1.0	0.209±0.039	0.35±0.074	0.148±0.022
1.0 - 1.2	0.122±0.016	0.148±0.039	0.067±0.014
1.2 - 1.4	0.066±0.011	0.081±0.015	0.039±0.006
1.4 - 1.6	0.049±0.014	0.065±0.018	0.026±0.004
1.6 - 1.8	0.029±0.009	0.038±0.010	0.014±0.003
1.8 - 2.0	0.020±0.004	0.028±0.004	0.0097±0.0016
2.0 - 2.2	0.013±0.002	0.016±0.003	0.004±0.0010
2.2 - 2.4	0.006±0.0011	0.010±0.002	0.003±0.0008
2.4 - 2.6	0.004±0.001	0.005±0.001	0.0012±0.0004
2.6 - 2.8	0.0015±0.00053	0.002±0.0009	0.0011±0.0002
2.8 - 3.0	0.0011±0.00052	0.002±0.0009	0.0011±0.0002

Table 4.4: The average of K^{*0} and $\overline{K^{*0}}$ invariant yields, $d^2N/(2\pi p_T dp_T dy)$, in each p_T bin for different collision centralities in *Cu+Cu* collisions at 62.4 GeV.

p_T (GeV/c)	(0-20)%	(20-40)%	(40-60)%
0.4 - 0.6	1.5348±0.301019	0.57±0.13	0.27±0.055
0.6 - 0.8	0.73158±0.237592	0.38±0.094	0.18±0.039
0.8 - 1.0	0.57483±0.0978938	0.35±0.074	0.148±0.022
1.0 - 1.2	0.366661±0.118472	0.148±0.039	0.067±0.014
1.2 - 1.4	0.219792±0.0308119	0.081±0.015	0.039±0.006
1.4 - 1.6	0.1487082±0.0385214	0.065±0.018	0.026±0.004
1.6 - 1.8	0.0762579±0.0204201	0.038±0.010	0.014±0.003
1.8 - 2.0	0.0636098±0.0121927	0.028±0.004	0.0097±0.0016
2.0 - 2.2	0.0413884±0.00744718	0.016±0.003	0.004±0.0010
2.2 - 2.4	0.0192156±0.00445683	0.010±0.002	0.003±0.0008
2.4 - 2.6	0.0122577±0.0033473	0.005±0.001	0.0012±0.0004
2.6 - 2.8	0.00823321±0.00202523	0.002±0.0009	0.0011±0.0002

Table 4.5: The average of K^{*0} and $\overline{K^{*0}}$ invariant yields, $d^2N/(2\pi p_T dp_T dy)$, in each p_T bin for different collision centralities *in Cu+Cu* collisions at 200 GeV.

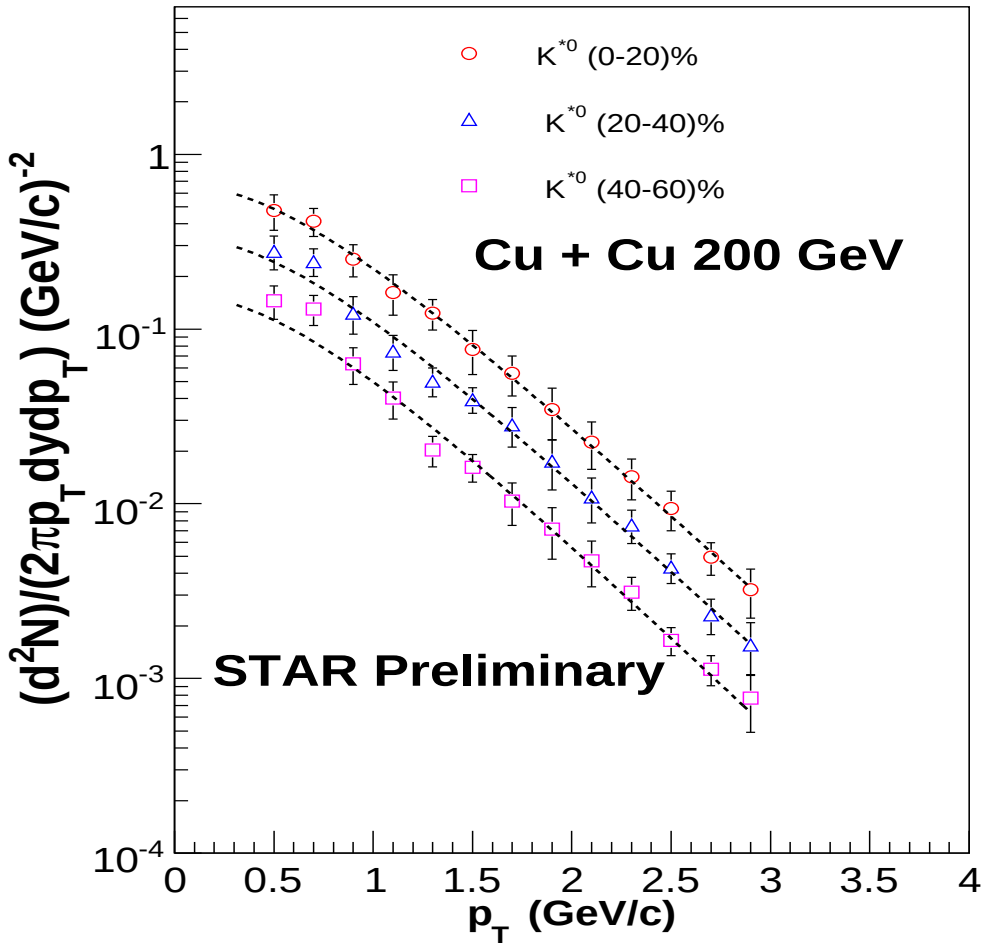

Figure 4.5: K^{*0} meson transverse momentum spectra for different centralities in Cu+Cu collisions at 200 GeV. The error bars shown are quadratic sums of the statistical and systematic errors. The dashed line represents an exponential fit (Eqn. 4.1) to the data points.

The particle production at low p_T is primarily due to non-perturbative soft processes and thus the p_T distribution at this regime is expected to be exponential in nature. However, at higher p_T, pQCD hard processes dominate particle production and we expect a power-law like distribution. This motivates one to compare the results obtained using a Levy function [92]. The Levy function is similar in shape to an exponential function at low p_T and behaves as a power law at higher p_T [93]. To generate the total yield, as given by dN/dy one needs to integrate the p_T distribution which is defined over a finite range of p_T. This integration can be done using either of the fits over an extrapolated p_T range, the difference defining the systematic uncertainties.

The Levy function used in the present case is given by

$$\frac{1}{2\pi p_T}\frac{d^2N}{dp_T dy} = \frac{(dN/dy)(n-1)(n-2)}{2\pi nT(nT + m_{K^*}(n-2))}[1 + \frac{m_T - m_{K^*}}{nT}]^{-n} \tag{4.2}$$

There are three open parameters in the fit function, which represents the mid-rapidity yield dN/dy, inverse slope parameter T and the exponent n. The differences in the invariant yield dN/dy and T are included in systematic uncertainties of the two variables.

The K^{*0} mid-rapidity yield, dN/dy, as a function of charged particle multiplicity, $dN_{ch}/d\eta$ (or centrality) is shown in Figure 4.6 . The base-line yield at mid-rapidity is calculated from the data points in the measured range while an exponential fit function was used to extract the yield outside the measured range. The figure shows, with an increase in $dN_{ch}/d\eta$ there is a corresponding rise in dN/dy indicating a scaling of dN/dy with N_{ch}, in both Au+Au and Cu+Cu collisions. Table 4.6 lists the K^{*0} mid-rapidity yield, dN/dy, in various collision systems for different centrality classes.

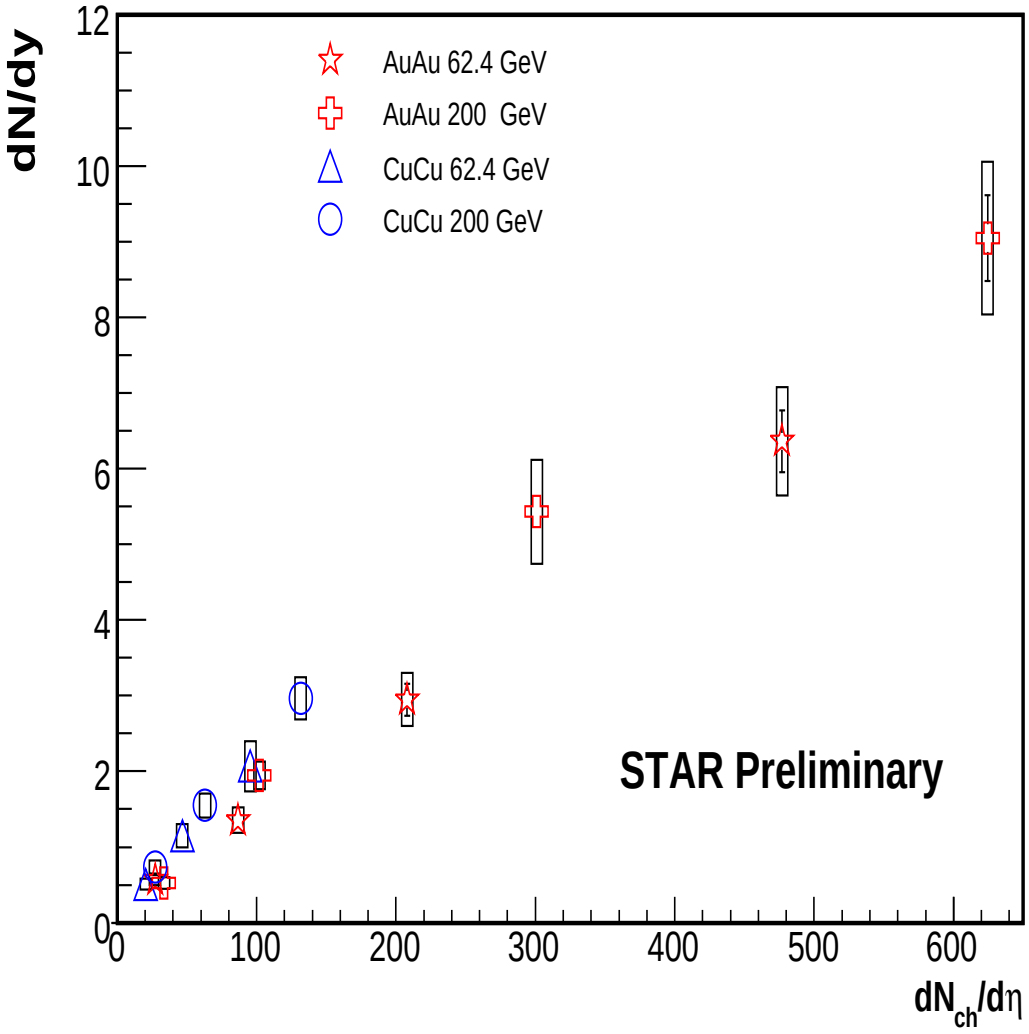

Figure 4.6: The K^{*0} dN/dy at mid-rapidity as a function charged particle multiplicity for different collision systems. The boxes represent the systematic errors.

Collision systems	Centrality	dN/dy
Au+Au(62.4 GeV)	0-20%	$6.3637 \pm 0.4053 \pm 0.712$
	20-40%	$2.95 \pm 0.212 \pm 0.35$
	40-60%	$1.353 \pm 0.09 \pm 0.17$
	60-80%	0.56180.030.07
Cu+Cu(62.4 GeV)	0-20%	$2.070013 \pm 0.074 \pm 0.33$
	20-40%	$1.15 \pm 0.063 \pm 0.15$
	40-60%	$0.5087 \pm 0.026 \pm 0.074$
Cu+Cu(200 GeV)	0-20%	$2.963 \pm 0.124 \pm 0.28$
	20-40%	$1.55 \pm 0.063 \pm 0.16$
	40-60%	$0.733 \pm 0.028 \pm 0.086$

Table 4.6: The K^{*0} dN/dy at $|y| < 0.5$ measured in *Au+Au* and *Cu+Cu* collisions at 62.4 GeV and 200 GeV for different centralities. Both statistical and systematic errors are shown. The first and the second error components correspond to statistical and systematic errors, respectively.

4.3 Mean Transverse Momentum

The UrQMD transport model calculations [88] predict that the high p_T K^* mesons are more likely to be reconstructed than the low p_T ones. This is because K^* mesons with larger p_T are more likely to escape the medium, much earlier than the kinetic freeze-out stage and hence they are less affected by the in-medium effects. Thus, in heavy ion collisions, $\langle p_T \rangle$ or the inverse slope parameter is expected to be larger than what is predicted in elementary *p+p* collisions [83].

Next we proceed to estimate the mean transverse momentum, $\langle p_T \rangle$ of K^{*0} which is determined using the following equation.

$$\langle p_T \rangle = \frac{\int_0^\infty p_T^2 exp[-(\sqrt{p_T^2 + m_{K^*}^2} - m_{K^*})/T] dp_T}{\int_0^\infty p_T exp[-(\sqrt{p_T^2 + m_{K^*}^2} - m_{K^*})/T] dp_T} \tag{4.3}$$

where, m_{K^*} is the standard K^* mass which is 896 MeV. The results for various systems as taken in the present case *viz Cu+Cu* (62.4 GeV and 200 GeV) and *Au+Au* (62.4 GeV) collisions, are presented in Table 4.7. The $\langle p_T \rangle$ was determined using the data

Collision systems	Centrality	$< p_T >$
Au+Au(62.4 GeV)	0-20%	$0.926912 \pm 0.047 \pm 0.0877$
	20-40%	$0.920687 \pm 0.045 \pm 0.0843$
	40-60%	$0.86326 \pm 0.056 \pm 0.082$
	60-80%	$0.754018 \pm 0.044 \pm 0.072$
Cu+Cu(62.4 GeV)	0-20%	$0.93604 \pm 0.049 \pm 0.06$
	20-40%	$0.8637 \pm 0.036 \pm 0.058$
	40-60%	$0.83329 \pm 0.037 \pm 0.057$
Cu+Cu(200 GeV)	0-20%	$1.02037 \pm 0.041 \pm 0.083$
	20-40%	$1.00553 \pm 0.040 \pm 0.086$
	40-60%	$0.9497 \pm 0.023 \pm 0.072$

Table 4.7: The K^{*0} $\langle p_T \rangle$ at $|y| < 0.5$ measured in *Au+Au* and *Cu+Cu* collisions at 62.4 GeV and 200 GeV for different centralities. Both statistical and systematic errors are shown. The first and the second error components correspond to statistical and systematic errors, respectively.

points in the measured range of the p_T spectrum while assuming an exponential behavior outside the fiducial range.

The K^{*0} $\langle p_T \rangle$ as a function of number of participants is shown in Figure 4.7 for several collision systems at different energies. As can be seen in the figure, the mean transverse momentum, $\langle p_T \rangle$, has no significant centrality and system size dependence in heavy ion collisions (*Au+Au* and *Cu+Cu*). However, $\langle p_T \rangle$ for the collision systems at 200 GeV is slightly higher than that at 62.4 GeV (in both *Au+Au* and *Cu+Cu* systems). In addition, we find that the K^{*0} $\langle p_T \rangle$ in heavy ion collisions is larger than the same in elementary *p+p* collisions, in agreement with the predictions of UrQMD model. These results are also consistent with the initial picture that high p_T resonances are more likely to be detected (reconstructed) since their daughter particles have reduced re-scattering effects. This would result in a higher value of the $\langle p_T \rangle$. In case of elementary *p+p* collisions low p_T resonances can also get efficiently detected (due to reduced re-scattering/in-medium effects) along with the ones with higher p_T. This makes the p_T spectrum steeper. Therefore $\langle p_T \rangle$ has a lower value.

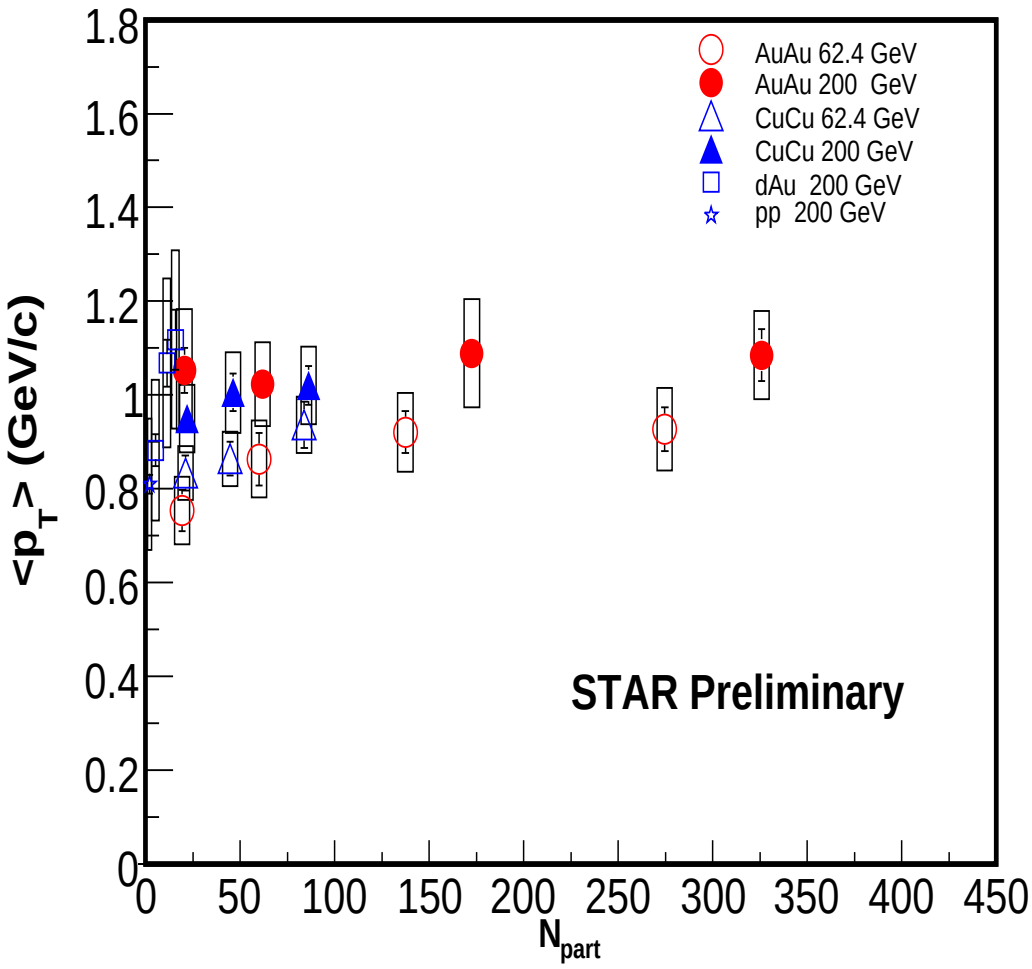

Figure 4.7: The K^{*0} $\langle p_T \rangle$ at mid-rapidity as a function of number of participants in different collision systems. The boxes represent the systematic uncertainties.

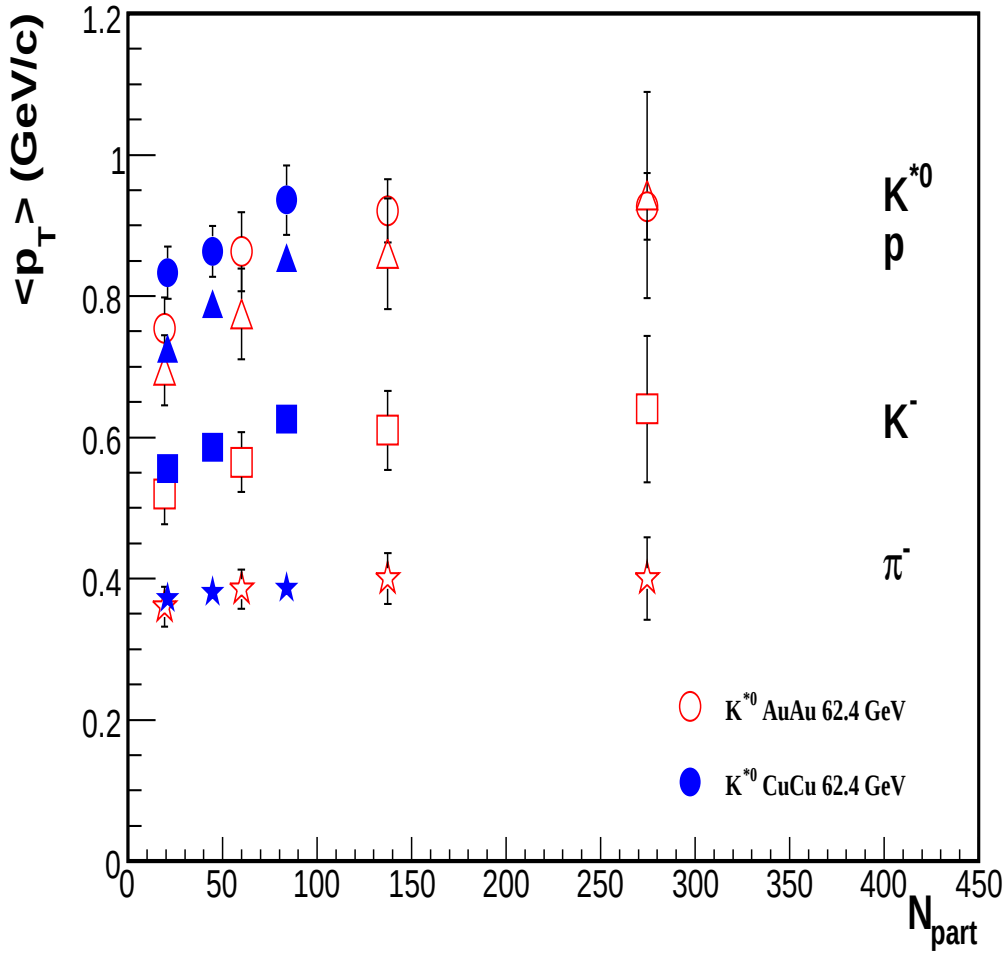

Figure 4.8: The mean transverse momentum, $\langle p_T \rangle$, of K^{*0}, as a function of number of participants compared to same for π^-, K^- and $\overline{p}$ in Au+Au and Cu+Cu collisions at 62.4 GeV.

Figure 4.8 shows the dependence of $\langle p_T \rangle$ for kaons, pions and protons, on the number of participants, N_{part} (for various centralities), as detected in the present Cu+Cu and Au+Au collision. The systematic errors include contributions from several different sources which consist of differences resulting from variations in functions fitted to K^{*0} mass peak as well as background, variations coming from Levy and exponential fits to the p_T distributions, variations coming from 2σ and 3σ cuts in particle identification and variations in other dynamical cuts applied at various stages. A more elaborate discussion on this is given in a following section. The values of N_{part} have been determined from Glauber model calculations [31]. We observe that $\langle p_T \rangle$ of K^{*0} mesons, for various values of N_{part} are higher than that of kaons and pions but are close to that of protons. The fact that the masses of protons and kstars are comparable, seems to indicate that $\langle p_T \rangle$ is strongly coupled with the mass of the particle.

4.4 Nuclear Modification Factor

The nuclear modification factors R_{CP} (central-to-peripheral ratio) and R_{AA} (scaled to p+p data) probe the dynamics of particle production during hadronization. Both are related to the source size and density of the medium produced in the heavy ion collisions [89, 90]. The variable R_{CP} corresponds to the ratio of the invariant yields, scaled to the number of binary collisions, N_{bin}, as obtained in central and peripheral collisions. It is defined as

$$R_{CP} = \frac{[dN/(N_{bin}dp_T)]^{central}}{[dN/(N_{bin}dp_T)]^{peripheral}} \tag{4.4}$$

N_{bin} is determined using the Glauber model [31]. The R_{CP} is taken to represent the nuclear modification factor since the peripheral collisions produce a medium that results in very little "in-medium" effects, similar to what happens in inelastic p+p

collisions. These results can really be compared with the modification factor R_{AA} which corresponds to the ratio of the invariant yields, as obtained in A+A and inelastic p+p collisions. This is given by

$$R_{AA} = \frac{[dN/(N_{bin}dp_T)]^{A+A}}{[dN/(\sigma_{pp}^{inelas}dp_T)]^{p+p}} \tag{4.5}$$

Here σ_{pp}^{inelas} is taken to be 42 mb. We expect the above mentioned ratios to be unity if nucleus-nucleus collisions were mere superpositions of nucleon-nucleon collisions. Any deviation observed from unity would signal towards nuclear effects.

As shown in Figure 4.9, in the intermediate p_T range, the R_{CP} of K^0_S and Λ [53], as obtained in Au+Au collisions are significantly lower than unity. This shows that there is energy loss of high p_T particles while traversing through the dense medium created in the collisions. We also observe that, in the intermediate p_T range, R_{CP} of K^0_S and Λ behave differently. As the mass of K^{*0} is close to the mass of baryons such as p and Λ and K^{*0} is a vector meson, the measurements of K^{*0} R_{AA} or R_{CP} compared to those of K^0_S and Λ can be used to distinguish whether the differences of nuclear modification factor between K^0_S and Λ is tied with the particle mass or species.

Figure 4.9 shows the present K^{*0} R_{CP} as obtained for Au+Au systems, as a function of p_T compared to that for Λ and K^0_S, obtained earlier [53]. In the present case the K^{*0} R_{CP} was obtained from ratio of the p_T spectra for top 10% (central) and 60-80% (peripheral) centrality classes corresponding to 200 GeV. For Au+Au collisions at 62.4 GeV, R_{CP} values were determined taking the p_T spectra of top 20% and 60-80% centrality classes. The Λ and K^0_S R_{CP} were obtained from the p_T spectra of the top 5% and 60-80% Au+Au collisions at 200 GeV. As can be seen in the figure, for $p_T < 1.8$ GeV/c, the R_{CP} for K^{*0} is smaller than the same for Λ and K^0_S. This is consistent with the fact that the re-scattering effect dominates over regeneration of K^{*0} at low p_T. For $p_T > 1.8$ GeV/c, the K^{*0} R_{CP}, for Au+Au collisions at 200

GeV, closely follows the R_{CP} of K^0_S which is found to be different from the R_{CP} of Λ. Since the masses of Λ and K^{*0} are similar, the observed difference seem to originate from effects other than mass. In such a scenario the observed differences could be visualised in terms of fact that one is a baryon while the other is a meson. This further supports the quark coalescence picture of particle production in the intermediate p_T range. This has been seen in an earlier publication where the elliptic flow parameter showed a scaling in terms of the number of constituent quarks, n [95]. High statistics Au+Au data at 200 GeV show $n = 2$ indicating a meson like behavior.

Figure 4.10 shows the K^{*0} R_{AA} for Au+Au and Cu+Cu collisions at 200 GeV. Top 10% and top 20 % central collision data, for Au+Au and Cu+Cu collisions respectively, were considered along with p+p data as a function of p_T. At $p_T > 1.0$ GeV/c, the K^{*0} R_{AA} in Au+Au is smaller than that of Cu+Cu collisions. This suggests greater energy loss for high p_T particles, in the medium formed in Au+Au collisions, as compared to the same in Cu+Cu system at the same energy. This indicates that the medium formed is more dense in Au+Au collisions at 200 GeV.

4.5 Particle Ratio

The ratio of the yields of resonances to that for stable particle such as kaon, pion and protons, produced in various collision systems at different beam energies, can shed light on the particle production mechanisms during hadronization. These ratios probe the dynamics involved in heavy ion collisions and also help to constrain the predictions of thermal model calculations. The measurement of K^{*0}/K^- yield ratio can provide vital information on the K^{*0} production properties as K^{*0} and K^- have different masses and spin but identical quark content. This ratio was observed to be smaller in Au+Au collisions compared to p+p collisions at the same beam energy [46, 91]. Figure 4.11 (Upper panel) shows the K^{*0}/K^- ratio as a function of number

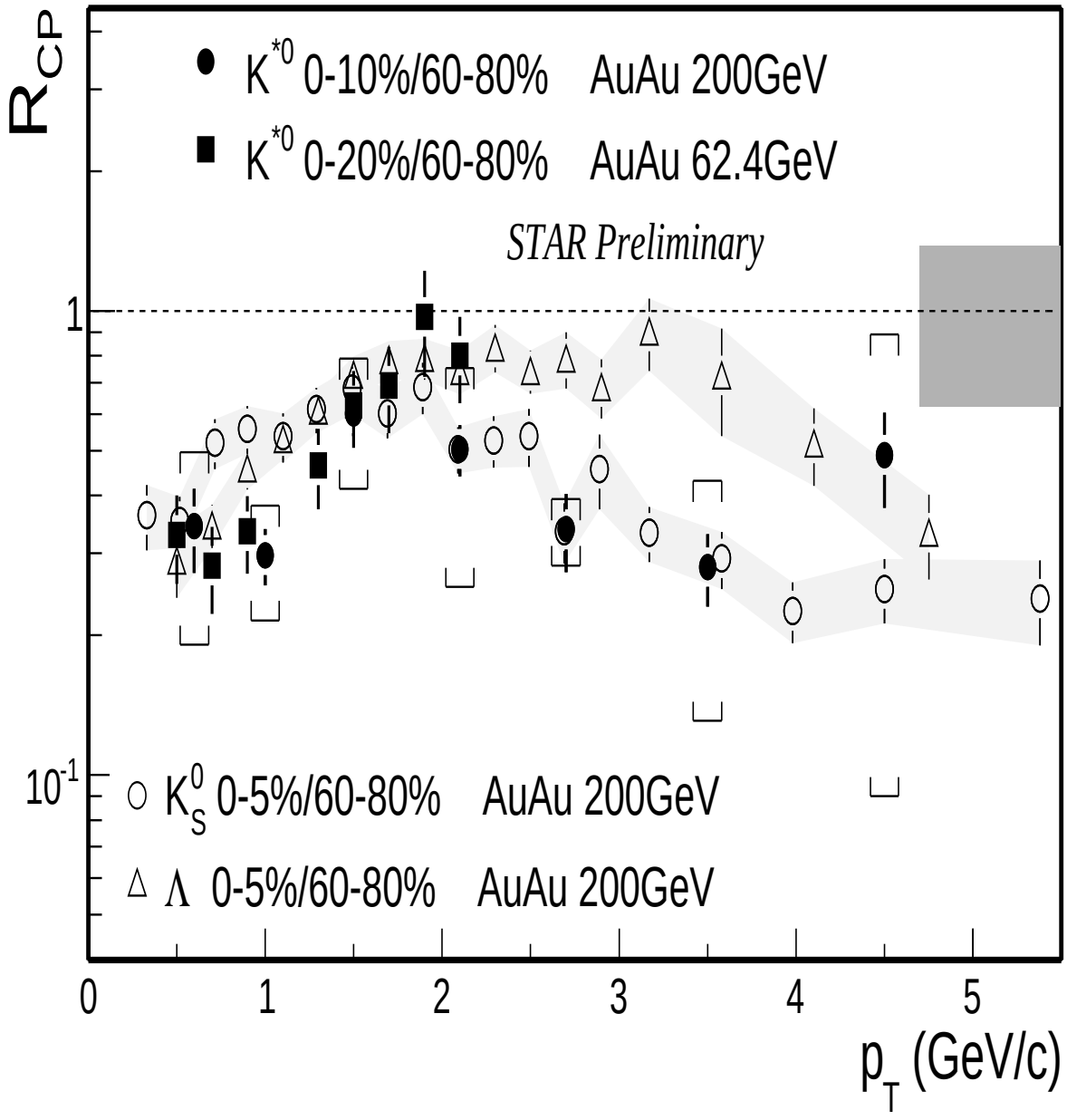

Figure 4.9: The K^{*0} R_{CP} as a function of p_T in $Au+Au$ collisions at 62.4 GeV and 200 GeV compared to the R_{CP} of K^0_S and Λ at 200 GeV. The widths of grey band represent the systematic uncertainties due to model calculations of N_{bin}. The dashed line represent the N_{bin} scaling.

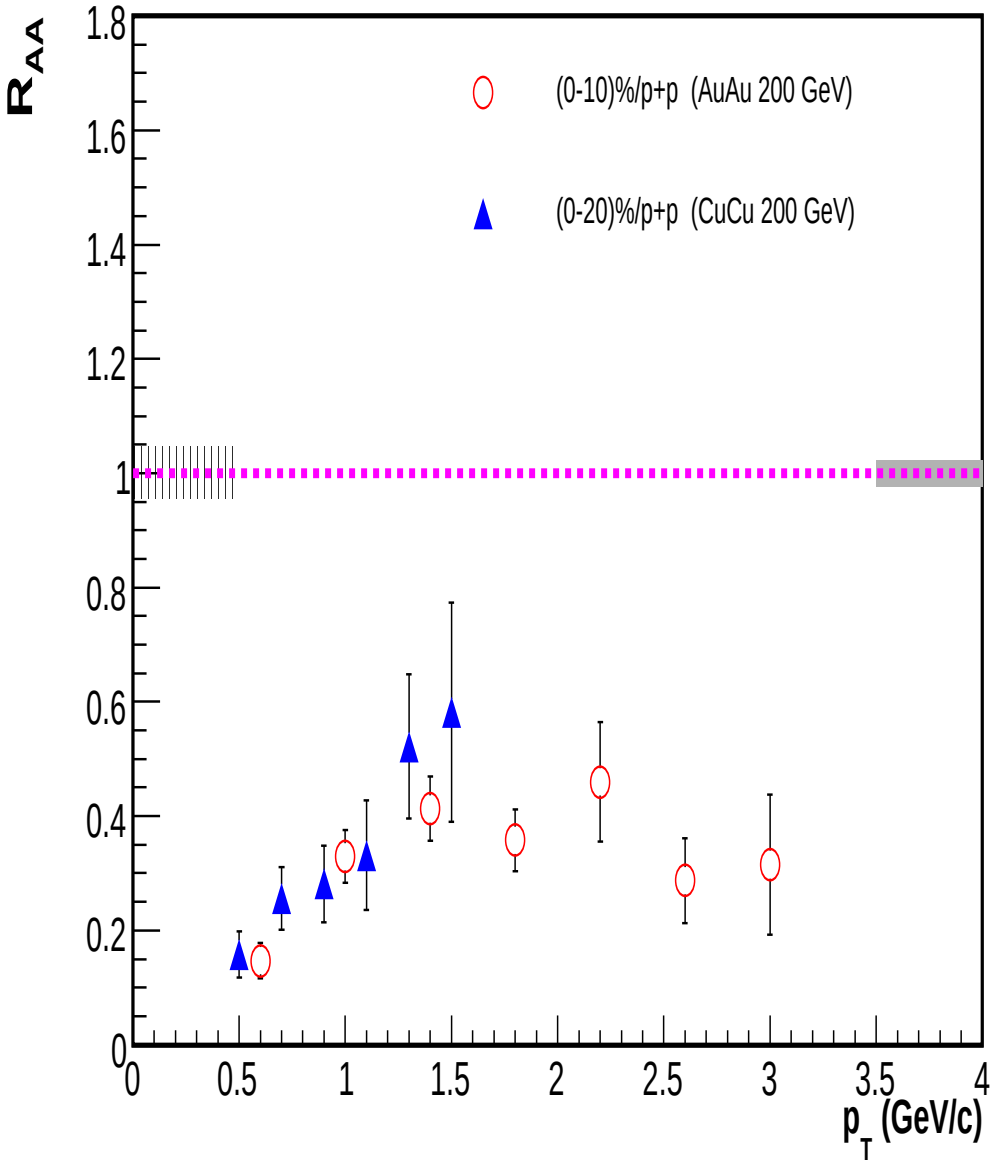

Figure 4.10: The K^* nuclear modification factor, R_{AA} as function of p_T in Au+Au and Cu+Cu collisions at 200 GeV. The width of shaded band on the left and right axis of the plot represent the systematic uncertainties due to model calculations of N_{bin} in Cu+Cu and Au+Au collisions at 200 GeV respectively.

of participants, N_{part}, in Au+Au and Cu+Cu collisions at 62.4 GeV and 200 GeV. The lower panel of the figure shows the K^{*0}/K^{-} yield ratio, normalized by their values measured in p+p collisions at similar $\sqrt{s_{\rm NN}}$. The kaon yield for p+p collisions at 200 GeV has been taken from [96]. We observe that K^{*0}/K^{-} yield ratio is much smaller than unity in central Au+Au collisions. This signals towards strong re-scattering of decay daughters of K^{*0} meson, resulting in loss of reconstructed K^{*0} signal. As mentioned in an earlier section, the re-scattering of K^{*0} daughter particles depends on the $\sigma_{\pi\pi}$ which is considerably larger than $\sigma_{\pi K}$. But $\sigma_{\pi K}$ is responsible for regeneration of K^{*0} meson. So we expect a decrease of K^{*0}/K^{-} yield ratio in heavy ion collisions owing to strong re-scattering of K^{*0} daughter particles. The observed decrease in the K^{*0}/K^{-} yield ratio, normalized by the same obtained for p+p collisions, indicates an extended life time for the hadronic phase as we move from p+p, d+Au to A+A collisions. The extended life time enhances the re-scattering effect.

Another parameter of considerable interest is ϕ/K^{*0} yield ratio as both ϕ and K^{*0} have similar masses with the same spin. However they have different strangeness and life-times. The life-time of ϕ is $\sim$40 fm which is about 10 times that of K^{*0}. Due to relatively longer life time, ϕ mesons are expected to decay outside the fireball. Therefore there is negligible re-scattering of its daughter particles. In addition, the cross-section for ϕ regeneration through two kaons, σ_{KK} is quite small. Therefore both the re-scattering and regeneration effect are negligible for ϕ meson. Thus an increase in ϕ/K^{*0} yield ratio is expected if there is a strong re-scattering of daughter particles of K^{*0}. It must also be mentioned here that ϕ has two strange quarks $(s, \overline{s})$ while K^{*0} has only one. Based on this, ϕ/K^{*0} yield ratio is also expected to provide information regarding strangeness enhancement. Figure 4.12 (Upper panel) depicts the ϕ/K^{*0} yield ratio with respect to number of participants in Au+Au and Cu+Cu collisions in 62.4 and 200 GeV. The lower panel of the figure shows the ϕ/K^{*0} yield ratio normalized by the same for p+p collisions at similar beam energy. As can

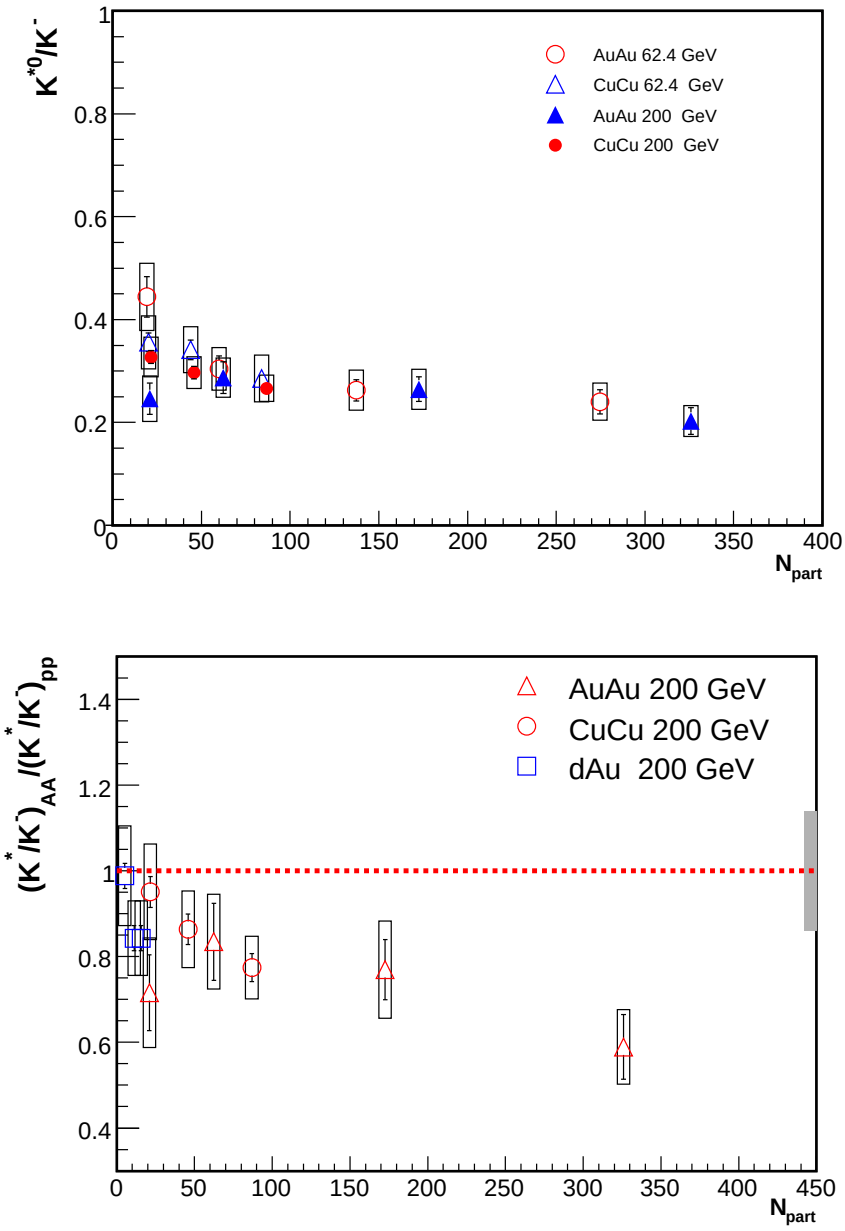

Figure 4.11: **Upper Panel** K^{*0}/K^{-} ratio at mid-rapidity as a function of N_{part}. **Lower Panel** K^{*0}/K^{-} ratio normalized by the same in p+p collisions as a function of N_{part}. The boxes represent the systematic errors. The width of grey band in the lower panel represent the systematic uncertainties due to p+p collisions.

be observed in the figure, this ratio increases with centrality favoring re-scattering scenario of K^{*0} daughter particles. However, in central Au+Au collisions at 200 GeV, the observed increase can have contributions from possible strangeness enhancement. The ϕ yield used for calculation of ratios has been taken from [98, 97]. The data for d+Au is from [48]. Table 4.8 shows the values of K^{*0}/K^{-} and ϕ/K^{*0} yield ratio in Au+Au and Cu+Cu collision at 62.4 GeV and 200 GeV for different centralities.

Collision systems	Centrality	K^{*0}/K^{-}	ϕ/K^{*0}
Au+Au(62.4 GeV)	0-20%	$0.240 \pm 0.0235 \pm 0.0358$	$0.506 \pm 0.034 \pm 0.085$
	20-40%	$0.26 \pm 0.021 \pm 0.039$	$0.49 \pm 0.034 \pm 0.075$
	40-60%	$0.304 \pm 0.025 \pm 0.041$	$0.392 \pm 0.027 \pm 0.064$
	60-80%	$0.444 \pm 0.0395 \pm 0.0655$	$0.240 \pm 0.014 \pm 0.042$
Cu+Cu(62.4 GeV)	0-20%	$0.285 \pm 0.010 \pm 0.045$	$0.507 \pm 0.020 \pm 0.096$
	20-40%	$0.341 \pm 0.018 \pm 0.044$	$0.434 \pm 0.024 \pm 0.083$
	40-60%	$0.355 \pm 0.018 \pm 0.051$	$0.373 \pm 0.020 \pm 0.073$
Cu+Cu(200 GeV)	0-20%	$0.266 \pm 0.011 \pm 0.025$	$0.658 \pm 0.028 \pm 0.086$
	20-40%	$0.297 \pm 0.012 \pm 0.030$	$0.580 \pm 0.024 \pm 0.092$
	40-60%	$0.327 \pm 0.012 \pm 0.038$	$0.450 \pm 0.018 \pm 0.091$

Table 4.8: The K^{*0}/K^{-} and ϕ/K^{*0} yield ratio in Au+Au and Cu+Cu collision systems at 62.4 GeV and 200 GeV for different centralities. The first and the second error components correspond to statistical and systematic errors, respectively.

In Figure 4.13, K^{*0}/K^{-} yield ratio is plotted as a function of center of mass energies. The ratios are compared to that of p+p collisions at different energies. We observe that K^{*0}/K^{-} in Au+Au collisions is significantly lower than that observed in p+p collisions in both 62.4 GeV and 200 GeV. This signifies that heavy ion collisions provide more suitable ambiance for stronger re-scattering of K^{*0} daughter particles and thus there is a suppression in the K^{*0} yield. The p+p data shown for K^{*0} and ϕ yield at 63 GeV are taken from ISR data [99]. The lower panel of Figure 4.13 depicts ϕ/K^{*0} yield ratio as a function of center of mass energies. The figure shows an enhancement of ϕ/K^{*0} when compared to same in p+p collisions favoring the re-scattering scenario over K^{*0} regeneration.

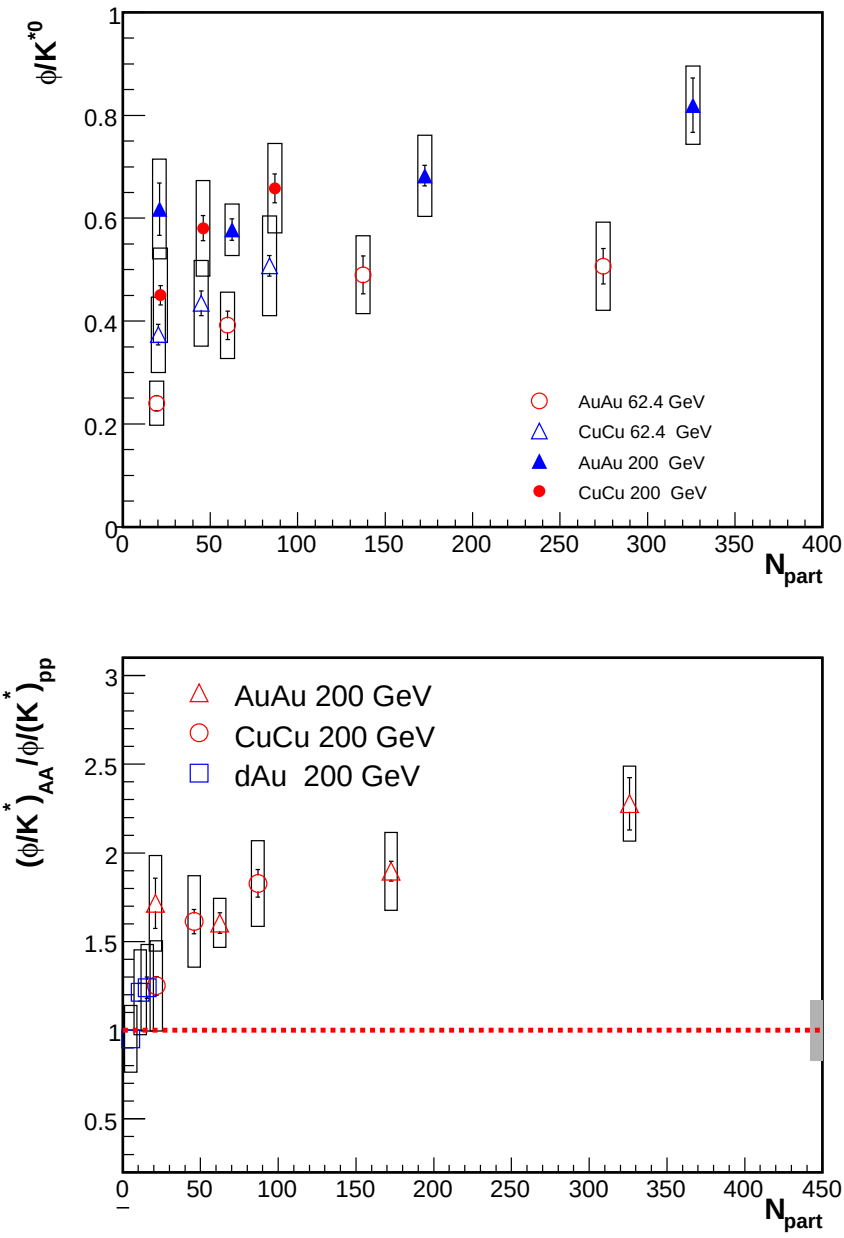

Figure 4.12: **Upper Panel** ϕ/K^{*0} ratio at mid-rapidity as a function of N_{part}. **Lower Panel** ϕ/K^{*0} ratio normalized by the same in p+p collisions as a function of N_{part}. The boxes represent the systematic errors.

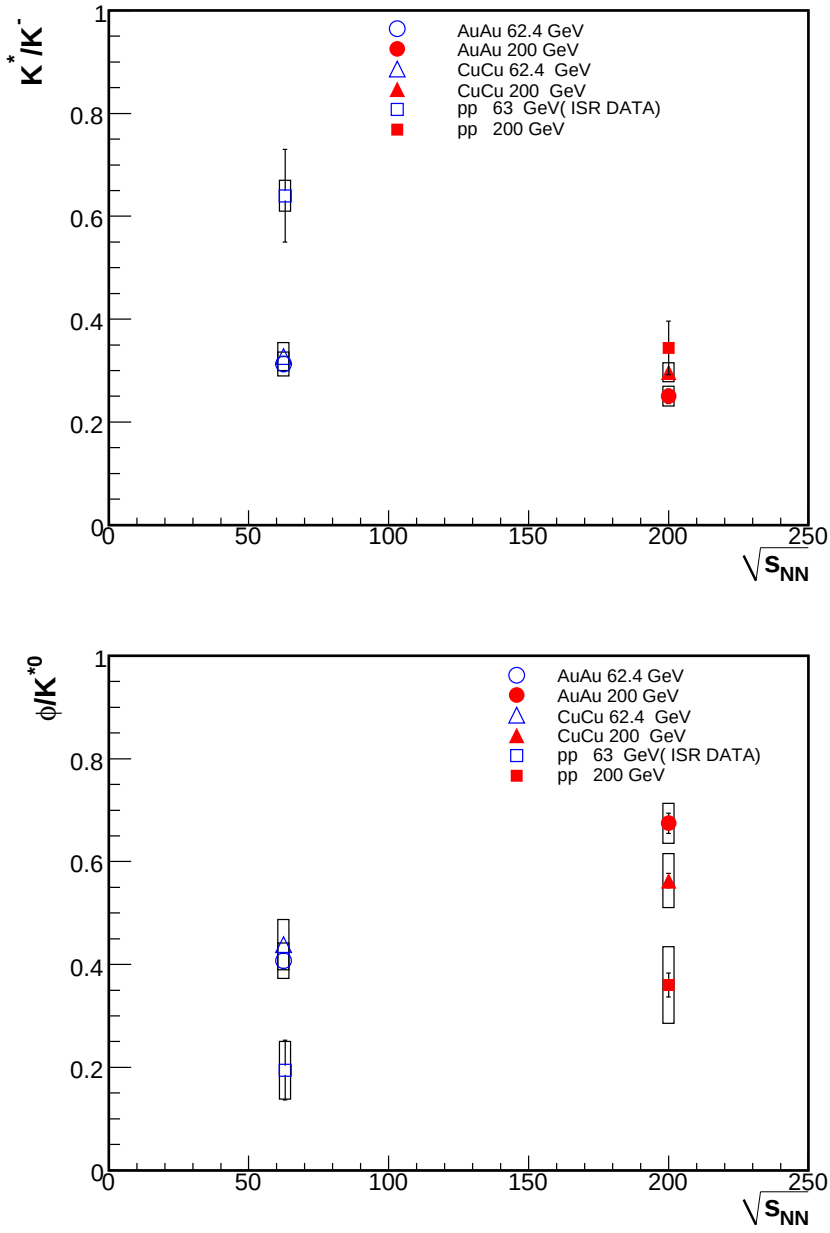

Figure 4.13: **Upper Panel** K^{*0}/K^{-} at mid-rapidity in minimum-bias p+p, Cu+Cu and Au+Au collisions as a function of $\sqrt{s_{NN}}$. **Lower Panel** ϕ/K^{*0} at mid-rapidity in minimum-bias p+p, Cu+Cu and Au+Au collisions as a function of $\sqrt{s_{NN}}$.

4.6 Systematic Uncertainties for Yield and Inverse Slope Parameter (or $\langle p_T \rangle$) for K^*

In order to study the systematic uncertainties on the dN/dy and $\langle p_T \rangle$ of K^* at mid-rapidity, one needs to consider the systematic errors, which come from different sources. The sources of these errors are: (1) different functions used to fit the invariant mass spectra of K^*, (2) different functions used to fit the p_T spectra, (3) different residual background functions, (4) variations in track types, (5) different V_Z cuts, and (6) all kinds of dynamical cuts and detector effects. Some of these sources are discussed below.

4.6.1 Fit Functions

The simple Breit-Wigner function as given by Equation 3.2, has been used to fit the K^* invariant mass signal and extract the yield for various p_T bins. One can try to fit the mass spectra using a different fitting function and see the relative differences which can be considered as systematic errors. In the present case, to determine the systematic errors, the invariant mass spectra for different p_T bins were fitted using the relativistic Breit-Wigner formula as given by

$$BW(M_{K\pi}) = \frac{Y M_{K\pi} M_{K^*} \Gamma(M_{K\pi})}{(M_{K\pi}^2 - M_{K^*}^2)^2 + M_{K^*}^2 \Gamma(M_{K\pi})^2} \tag{4.6}$$

where Y is a constant parameter proportional to the yield, $M_{K\pi}$ is the $K\pi$ invariant mass, M_{K^*} is the natural K^* mass (896 MeV), $\Gamma(M_{K\pi})$ representing the momentum dependent width which can be written as

$$\Gamma(M_{K\pi}) = \left[\frac{M_{K\pi}^2 - (m_\pi + M_K)^2}{M_{K^*}^2 - (m_\pi + M_K)^2}\right]^{3/2} \frac{\Gamma_{K^*} M_{K^*}}{M_{K\pi}} \tag{4.7}$$

where, Γ_{K^*} is the natural $K^*(892)$ width (50.7 MeV), m_π is the natural pion mass

(139 MeV), m_K being the natural kaon mass (493 MeV). K^* can also be re-generated through kaon and pion scattering in the hadronic medium. Because of this, the invariant mass of K^* is expected to be modified by the initial kaon and pion phase space distribution. So, the p-wave Breit-Wigner fitting function needs to be multiplied by a phase space factor which is given in the following equation.

$$PSF(M_{K\pi}) = \frac{M_{K\pi}}{\sqrt{M_{K\pi}^2 + p_T^2}} \times exp(\frac{-\sqrt{M_{K\pi}^2 + p_T^2}}{T_{fo}}) \tag{4.8}$$

where, p_T is the transverse momentum of the K^* and T_{fo} (160 MeV) is the expected freeze-out temperature at which the K^* resonance is emitted. In this case also there is a certain amount of residual background even after the subtraction of background obtained from mixed-events. This residual background, denoted by RBG, can be represented by a linear function:

$$RBG(M_{K\pi}) = BM_{K\pi} + C \tag{4.9}$$

Combining the above, with the phase space factor (PSF) and the BW function, we write the following function to fit the $K\pi$ invariant mass spectrum.

$$f(M_{K\pi}) = BW(M_{K\pi}) \times PSF(M_{K\pi}) + RBG(M_{K\pi}) \tag{4.10}$$

in which, Y, B, C, M_{K^*} and Γ_{K^*} are five open parameters with their usual meaning. We can now extract the mass and width of the $K^*(892)$ from the fit.

4.6.2 Uncertainty in residual background shape

There is some residual background (RBG) present in the reconstructed spectra even after the subtraction of the mixed event combinatorial background from the the same event invariant mass distribution. The shape of the residual background varies as a function of p_T. This may be due to contamination of the kaon and pion sample from

particle mis-identification due to overlap of dE/dx bands. In the present analysis we have used a linear function to describe the residual background. The systematic effects induced by this background function was studied by using second order polynomial to describe the residual background.

The first order and the second order polynomial functions used for background are defined as follows:

$$B_1(M) = aM + b \tag{4.11}$$

$$B_2(M) = aM^2 + bM + c \tag{4.12}$$

4.6.3 Track Types

In order to measure the various properties of K^* at mid-rapidity, we had combined the invariant mass spectra of K^{*0} and $\overline{K^{*0}}$. This was done to increase the statistics. To account for the systematic errors induced by this addition, we have obtained the invariant mass spectra of K^{*0} and $\overline{K^{*0}}$ separately for all the p_T bins and had extracted the mass, width and raw yields. After extracting them separately the data were combined to see the differences for various p_T bins.

4.6.4 Dynamical Cut Effects

There are systematic uncertainties on K^* results which occur due to various dynamical cuts, like: number of fit points on the TPC tracks (nfit), the ratio of number of fit points to the maximum number of possible fit points, DCA cut on detected tracks, acceptance cut based on η range, and $N_{\sigma K}$, $N_{\sigma\pi}$ cuts based on dE/dx. For the baseline analysis, the minimum number of fit points for tracks was taken to be 15 and the DCA cut was 1.5 cm for both pions and kaons. Further, all kaon and pion tracks with

$|\eta| < 1.0$ were selected. To get an idea about systematic uncertainties due to some relaxation of various cuts, we studied the variation of the number of fit points inside the TPC and N_σ cuts. We carried out the analysis with nfit points equal to 22 and opened up the $N_{\sigma K}$ and $N_{\sigma\pi}$ cuts from $(|N_{\sigma K}|, |N_{\sigma\pi}| < 2)$ to $(|N_{\sigma K}|, |N_{\sigma\pi}| < 3)$.

4.6.5 Detector Effects

For the baseline analysis, the collision vertex $(Z - vertex)$ was required to be within 30 cm. This was done to achieve uniform acceptance over the pseudo-rapidity range defined as $|\eta| < 1.0$. For studying the effect on Z-vertex shift, we have constrained the Z-vertex cut to 20 cm and estimated the differences.

4.6.6 Fit Function Used to Fit the p_T Spectra

In order to extract the yield (dN/dy) and the inverse slope parameter (or $\langle p_T \rangle$) of the p_T distribution, an exponential fit (explained earlier) was used for the baseline analysis. However, a Levy distribution was used over for extrapolating the data points outside the fiducial range.

4.6.7 Total Systematic Errors

All the systematic uncertainties coming from different sources, as discussed above, are listed in Table 4.9, 4.10 and 4.11. In table 4.12, we present an estimate of the total systematic errors which in every case has been evaluated as per the quadrature rule of error addition.

Different Cuts	dN/dy	$\langle p_T \rangle$ (GeV/c)
exponential fit	0%	0%
Levy fit	5.24%	0.44%
Backgrnd eqn 4.34	4.49%	2.88%
Relativistic BW	2.64%	0.542%
|Z-vertex| < 20	1.6%	1.05%
Track type (K^{*0})	3.6%	4.3%
Track type ($\overline{K}^{*0}$)	4.05%	5.96%
$nfit = 22$	4.32%	1.35%
$N_\sigma = 3$	4.45%	4.87%
Final Sys. Error	$\pm$11.18%	$\pm$9.47%

Table 4.9: The systematic uncertainties in percentages for K^{*0} at mid-rapidity ($|y|$ <0.5) on dN/dy and $\langle p_T \rangle$ in 0-20% Au+Au collisions at 62.4 GeV.

Different Cuts	dN/dy	$\langle p_T \rangle$ (GeV/c)
exponential fit	0%	0%
Levy fit	4.09%	0.156%
Backgrnd eqn 4.34	0.833%	1.76%
Relativistic BW	3.04%	0.99%
|Z-vertex| < 20	1.94%	0.908%
Track type (K^{*0})	3.69%	3.22%
Track type ($\overline{K}^{*0}$)	3.6%	3.21%
$nfit = 22$	3.09%	1.61%
$N_\sigma = 3$	4.76%	6.15%
Final Sys. Error	$\pm$9.44%	$\pm$8.13%

Table 4.10: The systematic uncertainties in percentages for K^{*0} at mid-rapidity ($|y|$ <0.5) on dN/dy and $\langle p_T \rangle$ in 0-20% Cu+Cu collisions at 200 GeV.

Different Cuts	dN/dy	$\langle p_T \rangle$ (GeV/c)
exponential fit	0%	0%
Levy fit	14.2%	3.48%
Backgrnd eqn 4.34	1.65%	1.39%
Relativistic BW	3.4%	1.46%
|Z-vertex| < 20	1.4%	2.32%
Track type (K^{*0})	3.6%	2.1%
Track type ($\overline{K}^{*0}$)	3.86%	2.2%
$nfit = 22$	1.73%	2.78%
$N_\sigma = 3$	2.3%	1.65%
Final Sys. Error	±15.94%	±6.4%

Table 4.11: The systematic uncertainties in percentages for K^{*0} at mid-rapidity ($|y|$ <0.5) on dN/dy and $\langle p_T \rangle$ in 0-20% Cu+Cu collisions at 62.4 GeV.

Table 4.12: The total systematic uncertainties in percentages for K^* at mid-rapidity ($|y|$ <0.5) on dN/dy and $\langle p_T \rangle$ in different collision systems.

Collision systems	Centrality	dN/dy	$\langle p_T \rangle$ (GeV/c)
Au+Au(62.4 GeV)	0-20%	11.18%	9.47%
	20-40%	11.86%	9.17%
	40-60%	12.59%	9.5%
	60-80%	12.5%	10.1%
Cu+Cu(62.4 GeV)	0-20%	15.94%	6.4%
	20-40%	13.04%	6.72%
	40-60%	14.56%	6.8%
Cu+Cu(200 GeV)	0-20%	9.44%	8.13%
	20-40%	10.32%	8.55%
	40-60%	11.73%	7.55%

Chapter 5

Conclusion

The aim of this thesis has been to study about the evolution of the medium created in relativistic heavy ion collisions through measurement of K^* resonance production. We have looked at *Au+Au* and *Cu+Cu* collisions at center-of-mass energies ($\sqrt{s_{\rm NN}}$) of 62.4 GeV and 200 GeV . The resonance production in the mid-rapidity, its centrality dependences, its transverse momentum distribution and medium dependent effects on mass as well as width have been studied. Earlier, similar studies have been carried out in *Au+Au* and *d+Au* collisions at 200 GeV. In the present case to see the system size dependence *Cu+Cu* collisions at both 62.4 GeV and 200 GeV have been taken into account. In addition, we have looked at *Au+Au* data at 62.4 GeV which is expected to yield some information on beam energy dependence of the observables. The data set taken correspond to Run IV and Run V data taken by the STAR at RHIC.

K^{*0} resonance production has been studied through its hadronic decay channel ($K^{*0} \rightarrow K^+\pi^-$ and $\overline{K^{*0}} \rightarrow K^-\pi^+$) with the decay particles detected in the STAR Time projection chamber. The mass and widths of the above resonance have been extracted from the reconstructed invariant mass distributions as functions of p_T. In the low p_T region, although the K^{*0} mass is found to be slightly lower than the PDG value, over the p_T range studied, in all collision systems taken, there is a reasonable

agreement between the two. Its width also agrees with the PDG value for all the collision systems.

The K^{*0} mid-rapidity integrated yield, dN/dy and the inverse slope parameter have been extracted from the p_T spectra for a wide range of centralities. The yield dN/dy is found to scale with charged particle multiplicity which is expected. The p_T spectra have been found to be well described by an exponential function for all the centralities. The $\langle p_T \rangle$ calculated from the above spectra are found to show no significant centrality dependence. However, it is found to be systematically higher for a beam energy of 200 GeV than that at 62.4 GeV. This is mainly because at higher energy there is greater re-scattering reducing the probability of detection of low p_T resonances. This re-scattering effect is much reduced in elementary p+p collisions where no loss in low p_T particles occurs. The presence of low p_T particles lower the mean value leading to a much lower value for the $\langle p_T \rangle$ ($\sim 0.81 GeV/c$) as compared to what one finds with heavy ion collisions ($\sim 1 GeV/c$). Therefore the mean, decided by the higher p_T particles, increases. Further, the $\langle p_T \rangle$ of K^{*0} mesons, while being comparable to that for protons, is found to be higher than that of charged kaons and pions. This seems to indicate that $\langle p_T \rangle$ is somehow coupled with the mass of the particle.

We have also looked at the nuclear modification factor, R_{CP} of K^{*0} for beam energies at 200 GeV and 62.4 GeV for Au+Au collisions. This was obtained taking the ratio of p_T spectra for 10% and 60-80% centrality classes. The results were compared with R_{CP} for K^0_S and Λ as obtained earlier. In the low p_T region, R_{CP} for K^{*0} is found to be smaller than the same for Λ and K^0_S. This indicates the dominance of re-scattering effects over regeneration. In the intermediate p_T range ($p_T > 1.8$ GeV/c), the K^{*0} R_{CP} is found to closely follow the R_{CP} of K^0_S which is different from the R_{CP} of Λ. Since the masses of Λ and K^{*0} are similar, the observed difference seem to originate from effects other than mass. In this scenario the observed

differences could be visualised in terms of fact that one is a baryon while the other is a meson. This goes in line with the quark coalescence model. We have also looked at medium induced effects on K^{*0} yield through the nuclear modification factor as defined by R_{AA}. In this case we have looked at the K^{*0} yield (scaled to number of binary collisions) in *Cu+Cu* as well as *Au+Au* collisions at 200 GeV, divided by the same as obtained from *p+p* collisions at the same energy. At intermediate and high p_T (> 1 GeV/c) R_{AA} is found to be smaller for *Au+Au* collisions than that in *Cu+Cu* collisions. This indicates that the system formed in *Au+Au* collisions at 200 GeV is denser than the medium formed in *Cu+Cu* collisions at the same energy.

Finally we have also studied the K^{*0}/K^{-} and ϕ/K^{*0} ratio in both *Cu+Cu* and *Au+Au* collisions. The measured K^{*0}/K^{-} ratio is found to be much smaller than the same in elementary *p+p* collisions. The daughter particles, coming from K^{*0} decay, interact among other particles in the medium. Their re-scattering depends on the $\sigma_{\pi\pi}$ which is considerably larger than $\sigma_{\pi K}$. But $\sigma_{\pi K}$, is responsible for regeneration of K^{*0}. As for results we have found a decrease of in the K^{*0}/K^{-} ratio, normalized by the same as measured in *p+p* collisions. This indicates that there is an extended lifetime of hadronic phase as we move from *p+p* through *d+Au* to heavy ion collisions. Also it suggests that the re-scattering effect in the hadronic phase is dominant over K^{*0} regeneration. The ϕ/K^{*0} ratio is observed to increase with centrality. This again favors the re-scattering scenario of K^{*0} daughter particles over their regeneration. The observed increase can have contributions from possible strangeness enhancement in more central collisions. The study of both the ratios as a function of various colliding species, collision centrality and beam energy favors the re-scattering scenario over K^{*0} regeneration.

Bibliography

[1] H. Kastrup, P. Zerwas, eds., QCD 20 yrs later *World Scientific, singapore*, (1993).

[2] D.J.Gross and F.Wilczek, *Phys. Rev. Lett.* **30**, 1343 (1973); H. Politzer, *Phys. Rev. Lett.* **30**, 1346 (1973).

[3] G.F. Chaplin, M.H. Johnson, E.Teller and M.S. Weiss, *Phys. Rev. D* **8**, 4302 (1973).

[4] T.D.Lee and G.C.Wick, *Phys. Rev. D* **9**, 2291 (1974).

[5] T.D.Lee, *Rev. Mod. Phys.* **47**, 267 (1975).

[6] J. C. Collins and M.J. Perry, *Phys. Rev. Lett.* **34**, 1353 (1975).

[7] K.Adcox *et al.*, *Nucl. Phys.* **A 757**, 184-283 (2005).

[8] J.Adams *et al.*, *Nucl. Phys.* **A 757**, 102-183 (2005).

[9] F.Karsch, Lecture Notes in Physics **583**, 209 (2002).

[10] P.Braun Munzinger, *Nucl. Phys.* **A 681**, 119 (2001).

[11] T.Csorgo, *Nucl.Phys.Proc.Suppl.* **92**, 62-74 (2001).

[12] M.Gazdzicki, *The Europ. Phys. Journal -Special Topics.* **155**, 37-44 (2008).

[13] B.B.Back *et al*, *Nucl. Phys.* **A 757**, 28 (2005).

[14] I.Arsene *et al*, *Nucl. Phys.* **A 757**, 1 (2005).

[15] J.Cleymans, B.Kampfer, M.Kaneta, S.Wheaton and N.Xu, *Phys. Rev.* **C 71** 054901 (2005).

[16] P. Braun-Munzinger, K.Redlich, and J.Stachel , nucl-th/0304013.

[17] J.Cleymans and K.Redlich, *Phys. Rev.* **C 60**, 054908 (1999).

[18] O.Barannikova *et al.*,STAR Collaboration, nucl-ex/0403014.

[19] A.M.Poskanzer and S.A. Voloshin, *Phys. Rev.* **C 58**, 1671-1678 (1998).

[20] C. Alt *et al.*, *Phys. Rev.* **C 68**, 034903 (2003).

[21] C. Adler *et al.*, *Phys. Rev.* **C 66**, 034904 (2002).

[22] A.Tang *et al.*, STAR Collaboration, *AIP Conf. Proc.* **698** , 701 (2004), J. Adams *et al.*, nucl-ex/0409033.

[23] J.Adams *et al.*, *Phys. Rev.* **C 72**, 14904 (2005).

[24] P.Huovinen, P.F.Kolb, U.Heinz, P.V. Ruuskanen, and S.A.Voloshin , *Phys. Lett.* **B 503**, 58 (2001).

[25] D.Molnar and S.A.Voloshin , *Phys. Rev. Lett.*, **91**, 092301 (2003).

[26] J.Rafelski and B.Muller, *Phys. Rev. Lett.* **48**, 1066 (1982).

[27] J.Cleymans, K.Redlich and E.Suhonen, *Z. Phys.* **C 51**, 137 (1991).

[28] F.Becattini and G.Pettini, *Phys.Rev.* **C 67**, 015205 (2003).

[29] B.Muller, *Nucl. Phys.* **A 527**, 617c-620c (1991).

[30] J.Adams *et al.*,*Phys. Rev.* **C 77**, 44908 (2008).

[31] J.Adams *et al.*,*Phys. Rev. Lett.* **91**, 172302 (2003).

[32] J.Adams *et al.*, *Phys. Rev. Lett.* **91**, 072304 (2003).

[33] D. Kharzeev *et al.*, *Phys. Lett.* **B 561**, 93 (2003); J. L. Albacete *et al.*, *Phys. Rev. Lett.* **92**, 082001 (2004); D. Kharzeev *et al.*, *Phys. Rev. D* **68**, 094013 (2003); R. Baier *et al.*, *Phys. Rev. D* **68**, 054009 (2003).

[34] T.Matsui and H.Satz,*Phys. Lett* **B 178**, 416 (1986).

[35] B.Alessandro *et al.*, *Euro. Phys.J.* **C 39**, 335-345 (2005).

[36] R.Arnaldi *et al.*, *Phys. Rev. Lett.* **99**, 132302 (2007).

[37] A.Adare *et al.*, *Phys. Rev. Lett.* **98**, 232002 (2007).

[38] A.Adare *et al.*, *Phys. Rev. Lett.* **98**, 232301 (2007).

[39] A.Adare *et al.*, *Phys. Rev. Lett.* **101**, 122301 (2008).

[40] A.Adare *et al.*, *Phys. Rev. Lett.* **96**, 012304 (2006).

[41] J.D.Bjorken, FERMILAB-PUB-82-59-THY and erratum(unpublished).

[42] R.Baier, D.Schiff and B.G.Zhakharov, *Ann. Rev. Nucl. Part.Sci* **50**, 37 (2000).

[43] C.Adler *et al.*, *Phys. Rev. Lett.* **90**, 082302 (2003).

[44] M.Bleicher *et al.*, *Phys. Lett.* **B 530**, 81 (2002).

[45] W. Broniowski and W. Florkowski, *Phys. Rev. Lett.* **87**, 272302 (2001).

[46] J.Adams *et al.*, *Phys. Rev* **C 71**, 064902 (2005).

[47] C.Adler *et al.*, *Phys. Rev.* **C 66**, 061901(R) (2002).

[48] J.Adams *et al.*, *Phys. Rev.* **C 78** 44906 (2008).

[49] R.Rapp and E.V.Shuryak , *Phys. Rev. Lett.* **86**, 2980 (2001).

[50] J.Adams *et al.*, *Phys. Rev. Lett.* **92**, 092301 (2004).

[51] S. D. Protopopescu *et al.*, *Phys. Rev.* **D 7**, 1279 (1973).

[52] M. J. Matison *et al.*, *Phys. Rev.* **D 9** 1872 (1974).

[53] J.Adams *et al. Phys. Rev. Lett.* **92**, 052302 (2004).

[54] V.Greco, M. Ko and P. Levai, *Phys. Rev. Lett.* **90**, 202302 (2003).

[55] C. Nonaka *et al. Phys. Rev.* **C 69**, 0319023 (2004).

[56] M.Harrison, T. Ludlam and S. Ozaki, *Nucl.Instrum. Meth.* **A 499**, 235-244 (2003).

[57] H. Pernegger, *Nucl.Instrum. Meth.* **A 478**, 68-79 (2001).

[58] K.H.Ackermann *et.al.*, *Nucl.Instrum. Meth.* **A 499**, 624-632 (2003).

[59] F.Bergsma *et.al.*, *Nucl.Instrum. Meth.* **A 499**, 633-639 (2003).

[60] M.Anderson *et.al.*, *Nucl.Instrum. Meth.* **A 499**, 659-678 (2003).

[61] R. Bellewid *et.al.*, *Nucl.Instrum. Meth.* **A 499**, 640-651 (2003).

[62] K.H.Ackermann *et.al.*, *Nucl.Instrum. Meth.* **A 499**, 713-719 (2003).

[63] 'A Ring Imaging Cherenkov Detector for STAR', STAR note 349, STAR/ALICE RICH Collaboration.

[64] W.J.Llope *et.al.*, *Nucl.Instrum.Meth.* **A 522**, 252 (2004).

[65] M.Beddo *et.al.*, *Nucl.Instrum. Meth.* **A 499**, 725-739 (2003).

[66] C.E.Allgower *et.al*, *Nucl.Instrum. Meth.* **A 499**, 740-750 (2003).

[67] M.M.Aggarwal *et.al*, *Nucl.Instrum. Meth.* **A 499**, 751-761 (2003).

[68] J.M.Landgraf *et.al*, *Nucl.Instrum. Meth.* **A 499**, 762-765 (2003).

[69] C.Adler *et.al.*, *Nucl.Instrum. Meth.* **A 499**, 778-791 (2003).

[70] L.Arnold *et.al.*, *Nucl.Instrum. Meth.* **A 499**, 652-658 (2003).

[71] F.S.Beiser *et.al.*, *Nucl.Instrum. Meth.* **A 499**, 766-777 (2003).

[72] C.Adler *et.al.*, *Nucl.Instrum. Meth.* **A 470**, 488-499 (2001).

[73] J.Abele *et.al.*, *Nucl.Instrum. Meth.* **A 499**, 692-702 (2003).

[74] M.Anderson *et.al.*, *Nucl.Instrum. Meth.* **A 499**, 679-691 (2003).

[75] D.Liko, "Track Fitting in STAR detector using the Kalman filter Method" *STAR NOTE*, **00087** , 1-15 (1992).

[76] Particle Data Group, *J. Phys. G* **33** , 1 (2006).

[77] H.Bichsel, *Nucl. Instrum. Meth.* **A 562**, 154 (2006); H. Bichsel, D. E. Groom, S. R. Klein, *Phys. Lett.* **B 592**, 242 (2004).

[78] Sevil Salur, Ph.D. Thesis, Yale University, 2006.

[79] C. Adler *et al.*,*Phys. Rev. Lett.* **89** (2002) 092301.

[80] C. Adler *et al.* ,*Phys. Lett.* **B 545** (2004) 143.

[81] D. Drijard *et al.*, *Nucl. Instrum. Meth.* **A 225**, 367 (1984).

[82] D. L'Hôte *et al.*, *Nucl. Instrum. Meth.* **A 337**, 544 (1994).

[83] H.Zhang, Ph.D. Thesis, Yale University, 2003.

[84] D. Mishra, Ph.D. Thesis, Utkal University, 2006.

[85] K.Hagiwara *et al.*, *Phys. Rev.* **D 66**, 010001 (2002).

[86] H.Long, Ph.D. Thesis, UCLA, 2002.

[87] R. Brun *et al.*, GEANT3 User's Guide, CERN/DD/EE/84-1 (1984).

[88] M.Bleicher and J.Aichelin, hep-ph/0201123; M.Bleicher *et al.*, *J. Phys. G.* **25**, 1859 (1999).

[89] Z.W. Lin and C.M. Ko, *Phys. Rev. Lett.* **89**, 202302 (2002).

[90] R.J. Fries *et.al.*, *Phys. Rev. Lett.* **90**, 202303 (2003).

[91] X.Dong *et.al*, *Int. J. Mod. Phys. E.* **16**, 2103 (2007).

[92] G. Wilk and Z. Wlodarczyk, *Phys. Rev. Lett.* **84**, 2270 (2000).

[93] Sarah Blyth, Ph.D. Thesis, University of Cape Town, 2007.

[94] S.Dash *et.al.*, *J. Phys. G.* **35**, 104057 (2008).

[95] S.Dash *et.al.*, *J. Phys. G.* **35** , 044061 (2008).

[96] B.I.Abelev *et al.*, *Phys. Rev.* **C 79**, 034909 (2009).

[97] B.I.Abelev *et al.*, *Phys. Letts.* **B 673**, 183 (2009).

[98] B.I.Abelev *et al.*, eprint: 0809.4737.

[99] T. Akesson *et al.*, *Nucl.Phys.* **B 203**, 27 (1982).